

Aus dem Institut für Biomedizinische Optik  
der Universität zu Lübeck  
Direktor: Prof. Dr. Alfred Vogel

# **Two-photon microscopy and UV laser nanosurgery of murine small intestine in vivo**

Dissertation  
zur  
Erlangung der Doktorwürde  
der Universität zu Lübeck

Aus der Sektion Naturwissenschaften

vorgelegt von  
Regina Bernadette Orzekowsky-Schroeder  
aus Bonn  
Lübeck 2013

1. Berichterstatter: Prof. Dr. Alfred Vogel

2. Berichterstatter: Prof. Dr. Christian Hübner

Tag der mündlichen Prüfung: 10. September 2013

Zum Druck genehmigt. Lübeck, den: 16. September 2013

# Zusammenfassung

Die menschliche Dünndarmschleimhaut besitzt eine Oberfläche von 200-400 m<sup>2</sup> und beheimatet einen großen Teil des Immunsystems. In dieser Arbeit wurden Zellbewegungen und andere Lebensvorgänge an der Dünndarmschleimhaut von lebenden Mäusen anhand von zweiphotonen-angeregter Autofluoreszenzmikroskopie (2PAM) spektral aufgelöst über Stunden untersucht. Um den intrinsischen Kontrast bei der 2PAM zu maximieren, wurden charakteristische Merkmale der Autofluoreszenzspektren (AF-Spektren) verschiedener Zelltypen und -organellen bestimmt. In einem weiteren Schritt wurden die Immun- und Heilungsprozesse nach laser-induzierten Mikroläsionen im Darmepithel untersucht.

Zur Bildgebung wurde ein Zweiphotonenmikroskop benutzt, das um einen spektralen Detektor mit vier Kanälen zwischen 380 und 680 nm erweitert wurde. Ein Femtosekundenpulslaser mit einer Pulswiederholrate von 80 MHz und einer zwischen 710 und 920 nm durchstimmbaren Wellenlänge wurde zur Fluoreszenzanregung benutzt.

In gesunder Schleimhaut wurden die AF-Spektren von Enterozyten, Lysosomen und antigen-präsentierenden Zellen (APCs) in Darmzotten und Peyerschen Plaques anregungs- und emissionsseitig bestimmt. Es wurde gezeigt, dass die Autofluoreszenz im Zytoplasma von Enterozyten hauptsächlich auf der reduzierten Form von Nicotinamid-Adenin-Dinukleotid-(Phosphat) beruht, während die AF-Spektren von APCs vorwiegend Anteile von lysosomalen Flavinen und Lipopigmenten aufweisen. Außerdem wurden AF-Spektren von Stellen mit stark gesteigerter Fluoreszenz bestimmt, welche durch zu hohe Belastung bei scannender Bestrahlung hervorgerufen wird. Ein Vergleich mit den AF-Spektren der anderen Gewebsbestandteile zeigte, dass hierbei durch photochemische und/oder photobiologische Prozesse neue Fluorophore entstanden sind, deren genaue Zusammensetzung jedoch noch nicht abschließend geklärt werden konnte.

---

Im zweiten Teil dieser Arbeit wurden gezielt einzelne Pulse eines UV-Lasers mit 355 nm Wellenlänge und 0.5 ns Pulsdauer ins Zottenepithel fokussiert, um Mikroläsionen zu setzen und die anschließende Gewebsantwort zu beobachten. Dabei wurden im Laserfokus über optischen Durchbruch Kavitationsblasen erzeugt. Die Größe der Blasen bestimmt die Größe des induzierten Schadens im Gewebe.

Größe und Dynamik der Kavitationsblasen wurden über ein Streulichtverfahren in einem interferometrischen Aufbau mit einem Dauerstrich-Laser gemessen. In dieser Arbeit konnten zum ersten Mal vollständige Radius-Zeit-Kurven von einzelnen Kavitationsblasen in Gewebe ermittelt werden. Dabei wurde eine sehr hohe räumliche Auflösung von 80 nm und eine zeitliche Auflösung von 5 ns erreicht.

In Abhängigkeit von der UV-Pulsenergie wurden im Schleimhautepithel Blasen in zwei Größenbereichen erzeugt: I) Maximalradius  $R_{max} = 0.6-2.4 \mu\text{m}$  und II)  $R_{max} = 7.3-25.6 \mu\text{m}$ . Die klare Abgrenzung der Größenbereiche spiegelt die Zweistufigkeit des optischen Durchbruchs mit Nanosekunden-Pulsen wieder, bei dem entweder Plasmen geringer Dichte oder stark leuchtende Plasmen erzeugt werden.

Die Gewebsantwort auf Blasen aus den zwei Größenbereichen unterscheidet sich stark. Typ I-Blasen sind kleiner als die Dimensionen einer typischen Epithelzelle. Bei solchen Blasen verliert die betroffene Zelle ihre Autofluoreszenz, ihre Plasmamembran bleibt intakt, und die Zelle verbleibt vorerst im Epithel.

Typ II-Blasen sind viel größer als eine Epithelzelle. In diesem Fall weitet der Schaden sich aus, und es verlieren 5-6 oder mehr benachbarte Zellen nach und nach ihre Autofluoreszenz. Die Plasmamembran dieser Zellen ist zerstört, und innerhalb von 30 Minuten werden die Zellen aus dem Epithelverband ausgestoßen und ins Darmlumen abgegeben. Gleichzeitig rücken benachbarte, gesunde Epithelzellen zusammen, flachen sich ab und schieben sich langsam unter den abgestoßenen Epithelzellen über die Wunde. Ferner wandern bereits in der ersten Minute nach dem UV-Puls polymorphonukleare Leukozyten (PMNs) in die Schadensregion ein. PMNs sind Teil des angeborenen Immunsystems und ihr Auftauchen definiert den Beginn einer sterilen Entzündung. Innerhalb von zwei Stunden heilen alle Schäden dieser Größe vollständig und folgenlos ab, und es wurde kein Verbleib von PMNs im Gewebe beobachtet.

Die Kenntnis der Entzündungs- und Heilungsreaktionen nach kleinen Schäden an der gesunden Schleimhaut kann in Zukunft helfen zu verstehen, welche Prozesse im Falle

---

von entzündlich veränderter Schleimhaut gestört sind, wenn man die Methodik dieser Arbeit auf ein geeignetes Modell chronisch-entzündlicher Darmschleimhaut überträgt.

---

# Summary

Human small-intestinal mucosa has an enormous surface of 200-400 m<sup>2</sup> and houses a large part of the immune system. In this work, processes in the living small intestinal mucosa of mice were studied over several hours using spectrally resolved two-photon excited autofluorescence microscopy (2PAM). To maximize intrinsic contrast of 2PAM, characteristic features of the autofluorescence (AF) spectra were determined for various cell types and cell organelles. In a further step, immune and healing response to laser-induced micro-lesions in the intestinal epithelium were studied.

For spectral imaging a two-photon microscope was equipped with a detector with four emission channels between 380 and 680 nm. Fluorescence was excited using a femtosecond laser with tunable wavelength between 710 and 920 nm.

In healthy intestinal mucosa, the AF spectra of enterocytes, lysosomes, and antigen-presenting cells (APCs) were acquired in villus regions and in Peyer's patches. It could be shown that AF in the cytoplasm of enterocytes arises mainly from the reduced form of nicotinamide adenine dinucleotide (phosphate), while APCs' AF is dominated by contributions of lysosomal flavins and lipopigments. Further, AF spectra were acquired of sites with massively increased fluorescence that indicates photodamage by scanning irradiation. Comparison with the AF spectra of the other tissue components showed that in the fluorescent lesions new fluorophores have formed by either photochemical or photobiological processes. However, their exact composition could not yet be determined.

In the second part of this work, microlesions were induced by focussing single pulses of a UV laser with 355 nm wavelength and 0.5 ns pulse duration into the villus epithelium, and the tissue response was observed by 2PAM. In the laser focus, a cavitation bubble is formed by optical breakdown. The bubble's size determines the size of the

---

induced tissue lesion.

Size and dynamics of the cavitation bubbles were measured using an interferometric backscattering technique with an additional probe laser in continuous wave mode. In this work, for the first time complete radius-time curves of single cavitation bubbles in tissue could be determined, with very high spatial and temporal resolution of 80 nm and 5 ns respectively.

Depending on the UV-laser pulse energy, bubbles in two size regimes were generated: I) maximum radii  $R_{max} = 0.6-2.4 \mu\text{m}$  and II)  $R_{max} = 7.3-25.6 \mu\text{m}$ . The clear delineation of the size regimes is characteristic for optical breakdown with UV nanosecond pulses, in which either low-density plasmas or brightly luminescent plasmas are produced.

Tissue response to bubbles of these two size regimes differs strongly. Type-I bubbles are smaller than a typical epithelial cell. For such bubbles, the affected cell loses its autofluorescence, its plasma membrane remains intact, and the cell remains in the epithelium during the observation time.

Type-II bubbles reach a size much larger than an epithelial cell. In this case, the damage spreads until it encompasses 5-6 or more adjoining cells that all lose their autofluorescence. The plasma membrane of these cells is destroyed and within 30 minutes the cells are expelled into the intestinal lumen. At the same time, healthy neighboring cells migrate towards the wound, flatten and stretch out below the expelled cells to cover the denuded area. Further, already within the first minute after application of the UV pulse, polymorphonuclear lymphocytes (PMNLs) immigrate into the damaged region. PMNLs are cells of the innate immune system, and their appearance defines the onset of a sterile inflammation. Within two hours, lesions of this size have completely healed and no remaining PMNLs were observed in the tissue.

Knowledge of inflammatory and healing reactions after small damage of healthy intestinal mucosa forms a basis for future research that aims at identifying the processes, which are disturbed in the case of chronic intestinal bowel disease. For this purpose, the methodology developed in this work can in future be applied to study models of chronic intestinal bowel disease.

# Contents

<b>Zusammenfassung</b>	<b>ii</b>
<b>Summary</b>	<b>vi</b>
<b>1 Introduction</b>	<b>1</b>
<b>2 Physiology of small intestinal mucosa</b>	<b>5</b>
2.1 Immune system . . . . .	5
2.2 Basic intestinal anatomy . . . . .	8
2.3 Selected functional compartments . . . . .	9
2.3.1 Villi and crypts . . . . .	9
2.3.2 Peyer’s patches . . . . .	11
<b>3 Methodical principles</b>	<b>13</b>
3.1 Two-photon-excited fluorescence microscopy . . . . .	13
3.1.1 Fundamental working principle and specifications . . . . .	13
3.1.2 Autofluorescence vs. molecular markers . . . . .	14
3.1.3 Spectral imaging . . . . .	15
3.2 Plasma-mediated laser nanosurgery . . . . .	16
3.2.1 Optical breakdown and plasma formation . . . . .	16
3.2.2 Plasma-induced events . . . . .	19
3.2.3 Transition from imaging to surgery . . . . .	20
3.3 Online-dosimetry by bubble interferometry . . . . .	22
3.3.1 Bubble monitoring by probe beam scattering . . . . .	22

## CONTENTS

---

3.3.2	Determination of bubble size and dynamics . . . . .	24
<b>4</b>	<b>Experimental setup and methods</b>	<b>27</b>
4.1	Mouse model . . . . .	27
4.2	Spectrally resolved two-photon microscopy . . . . .	28
4.3	Image analysis . . . . .	31
4.4	Laser manipulation . . . . .	34
4.5	Staining protocols . . . . .	36
<b>5</b>	<b>Spectrally resolved 2PM of murine small intestine</b>	<b>39</b>
5.1	Physiological appearance . . . . .	40
5.2	Autofluorescence spectra of cells and cell organelles . . . . .	46
5.3	Correlation of spectral cell signatures to endogenous fluorochromes . . . . .	54
5.4	Rapid fluorescence increase and photodamage . . . . .	56
5.5	Conclusions . . . . .	59
<b>6</b>	<b>UV-laser microsurgery and tissue response</b>	<b>61</b>
6.1	Bubble dynamics and size . . . . .	62
6.2	Tissue response to laser-induced lesions . . . . .	69
6.2.1	Tissue response to small cavitation bubbles . . . . .	69
6.2.2	Tissue response to large cavitation bubbles . . . . .	71
6.3	Conclusions . . . . .	76
<b>7</b>	<b>Outlook</b>	<b>79</b>
	<b>List of Movies</b>	<b>83</b>
	<b>References</b>	<b>85</b>
	<b>Publications</b>	<b>95</b>

# 1

## Introduction

With a surface of 200-400 m<sup>2</sup> the intestine is the largest and one of the most important interfaces at which the body comes into contact with the environment [Lüllmann-Rauch 2006, Mowat and Viney 1997, von Brandis and Schönberger 1995]. Everyday, several kilograms of partially digested food mass pass by that contain not only nutrients but also pathogens such as bacteria or parasites, which must be prevented from entering the body. Consequently, a major part of the immune system is located in the gut. It is estimated, that more than 60 % of the total body's T-lymphocytes, an important group of small immune cells, is associated with the small intestine [Guy-Grand and Vassalli 1993]. Lymphocytes and numerous other immune cells reside in the intestinal epithelium and in the underlying tissue layer, the so-called lamina propria [Didierlaurent et al. 2002]. Further, organized gut-associated lymphoid tissue is found in the form of mesenterial lymph nodes and the so-called Peyer's patches in the ileum. Peyer's patches are secondary lymphatic organs where specialized epithelial cells, named M-cells, take up antigens from the lumen [Gebert 1997, Wolf and Bye 1984] to present them to immune cells such as lymphocytes and antigen-presenting cells that reside in the follicular regions below the M-cells [Brandtzaeg et al. 1999]. A network of highly complex mechanisms ensures that an immune response is elicited, when pathogenic substances are detected, while tolerance to apathogenic factors is maintained [Mowat and Viney 1997].

This intricate selective barrier function ultimately depends on its key element, an intact epithelial cell layer. Although it is constantly mechanically worn, the single-layered epithelium is only protected by a thin layer of mucus that is produced by

## 1. INTRODUCTION

---

scattered goblet cells within the epithelium. Therefore, small lesions occur frequently on a daily basis, for example due to passage of hard food compounds.

In the presence of a local epithelial defect, pathogens might have the chance to enter the lamina propria through that lesion and trigger an immune reaction. In the case of various intestinal disorders, repeated damage and impairment of the mucosal surface barrier is observed. This may lead to inflammation, uncontrolled immune response, and disequilibrium of the homeostasis of the organism. A leaky gut may be even responsible for the development of not only bowel cancer but also for cancer that arises at other organs and is a consequence of a defect intestinal mucosa that is permeable for pathogens and carcinogens [Fasano 2011, Fink 1990, Lin et al. 2012, Marchiando et al. 2010, Turner 2009]. Therefore, rapid resealing of the epithelial surface barrier and extrusion of damaged cells into the lumen following injuries are essential to preserve normal tissue homeostasis.

Although this important immunologic scene essentially is an interface to the body's outside, it is located within the body and is hardly accessible for investigation. Therefore, the barrier function of the epithelium has been mainly studied using *in vitro* models. The focus was laid either on assessing repair mechanisms on a cellular level, termed epithelial restitution [McCormack et al. 1992, Moore et al. 1989b, Nusrat et al. 1992], or on the molecular factors involved [Dignass 2001, Fasano 2011]. However, none of these *in vitro* models can give a full picture, because they lack the connection to resources of the immune system that are located outside of the epithelium. Therefore, in order to gain insight into the dynamics of this highly complex mucosal barrier system, an *in vivo* model is needed that is combined with time-lapse and three-dimensional imaging with subcellular resolution, which allows for reliable and non-damaging discrimination of the various cell types. The study of tissue dynamics in response to injury requires the capability of creating lesions at a predetermined location and time with control of the initial lesion size. These prerequisites make laser nanosurgery in combination with two-photon excited autofluorescence microscopy the instrument of choice for this work.

In this thesis, processes in the living small intestinal mucosa of mice were studied over several hours. For that purpose, an intravital mouse model established by Klinger et al. [2012], and spectrally resolved two-photon excited autofluorescence microscopy (2PAM) were used. To maximize intrinsic contrast during 2PAM, characteristic features

---

in the autofluorescence spectra of various cell types and cell organelles were determined. In a further step, immune and healing response after controlled laser-induced lesions in the epithelial barrier were investigated.

This thesis is structured as follows. First, a short overview over the immune system is given in chapter 2. The two lines of defense, innate and adaptive immunity, are briefly described and their most important cellular representatives introduced. Then the anatomical structure and normal physiologic function of healthy intestinal mucosa is summarized in sections 2.2 and 2.3.

Chapter 3 introduces the methodical principles applied in the experiments, which rely on light-tissue interactions in different irradiance regimes. Spectrally resolved two-photon excited fluorescence microscopy uses nonlinear absorption of scanning irradiation at comparatively low irradiance to induce fluorescence. By local application of light with higher irradiance, plasma-mediated precise nanosurgery can be performed. Lesions created to probe the intestinal barrier function are due to the disruptive action of cavitation bubbles produced during plasma-expansion. The size of these cavitation bubbles determines the size of the tissue lesion [Hellman et al. 2007, Hutson and Ma 2007, Vogel et al. 1996]. An interferometric probe-beam scattering technique allows determination of the cavitation bubble's size and dynamics with nm spatial and ns temporal resolution [Vogel et al. 2008] and thus enables an online-monitoring of the lesion size. Chapter 4 then describes the experimental implementation of the above methods as well as the in vivo mouse model for spectrally resolved autofluorescence microscopy and UV-laser nanosurgery of intestinal mucosa.

The results of this thesis are presented and discussed in two chapters. In chapter 5, it is demonstrated that autofluorescence based two-photon microscopy can reveal the complex morphology and functional dynamics of vital murine intestinal mucosa. Subcellular resolution allows to easily distinguish individual cells and their cytosolic organelles based on their morphology. For the first time, physiological processes such as peristalsis or shedding of aged epithelial cells were imaged with microscopic resolution in vivo. Autofluorescence excitation-emission spectra were recorded for different cell types and cell organelles that are relevant for digestion and immune response, the two major functions of small intestine. The excitation and emission measurements of two-photon excited cellular autofluorescence spectra are linked to spectra of endogenous chromophores. The possibility of generating multi-parameter spectral fingerprints

## 1. INTRODUCTION

---

of different cell types is demonstrated. It is shown, that selective fluorescence excitation with two separate wavelengths is beneficial for contrasting epithelial enterocytes and antigen presenting cells. This information lays the basis for future automated identification of cells in images of this highly dynamic tissue or as a tool for targeted manipulation of single cells based on their spectral autofluorescence characteristics. Photodamage reveals itself in a drastic increase of the emission intensity and a change of spectral characteristics, which may be used for online dosimetry of safe imaging.

Chapter 6 describes the tissue reactions provoked by focussing ns laser pulses into the epithelium. As a function of laser pulse energy, cavitation bubbles are produced in two distinct size regimes. For small bubbles, with maximum radii  $R_{max} = 0.6-2.4 \mu\text{m}$ , damage is restricted to one cell that loses its autofluorescence and remains in the epithelium during the observation time of 30 minutes. For large bubbles,  $R_{max} = 7.3-25.6 \mu\text{m}$ , the damage region spreads and encompasses 5-6 and more adjoining cells that lose their autofluorescence and exhibit damaged plasma membranes. The damaged cells are expelled within 30 minutes from the epithelium and shed into the intestinal lumen. Simultaneously, neighboring healthy epithelial cells move toward the lesion and cover the denuded area. Further, already within 1 minute after application of the laser pulse, the advent of polymorphnuclear leucocytes (PMNs), inflammatory cells of the innate immune system, was observed. After two hours at the latest, all lesions were completely healed, no inflammatory cells remained in the tissue, and the integrity of the mucosal barrier was reestablished.

The results presented in chapter 6 lay the basis for understanding inflammatory and healing reactions after small damage of the immunologically important environment of small intestinal mucosa. It could be shown that in a healthy individual, small lesions are rapidly closed without further consequences for tissue homeostasis.

Finally, in chapter 7 open questions are discussed and it is outlined how the methods for controlled and precise creation and simultaneous observation of small tissue lesions may in future be applied to study tissue reactions of inflamed tissue, for example in the case of chronic intestinal bowel disease.

## 2

# Physiology and function of small intestinal mucosa

The small intestine has a selective barrier function between body and environment and plays a crucial role in the immune system. Therefore, this chapter will give a short overview of the immune system, before the intestinal anatomy is briefly introduced with a focus on the functional compartments that are investigated in this work [Lüllmann-Rauch 2006, von Brandis and Schönberger 1995].

## 2.1 Immune system

The immune system protects the body from various noxious substances: e.g. pathogenic microorganisms, degenerated or infected body's own cells, and alien cells. This highly complex system can be roughly categorized into the **innate (unspecific)** and **adaptive (specific) immune system**; however, both branches are functionally intertwined [Lemaitre et al. 1996, Poltorak et al. 1998, Schuler and Steinman 1985, Steinman and Cohn 1973, Steinman and Witmer 1978]. Figure 2.1 shows schematically the two branches of the immune system and their cellular representatives.

All cellular representatives of the immune system, **lymphocytes, granulocytes, and antigen-presenting cells (APCs)**, are also referred to as white blood cells. A leading part in both branches of the immune system is played by **lymphocytes**, which either are involved directly in defense or support defensive measures of other

## 2. PHYSIOLOGY OF SMALL INTESTINAL MUCOSA

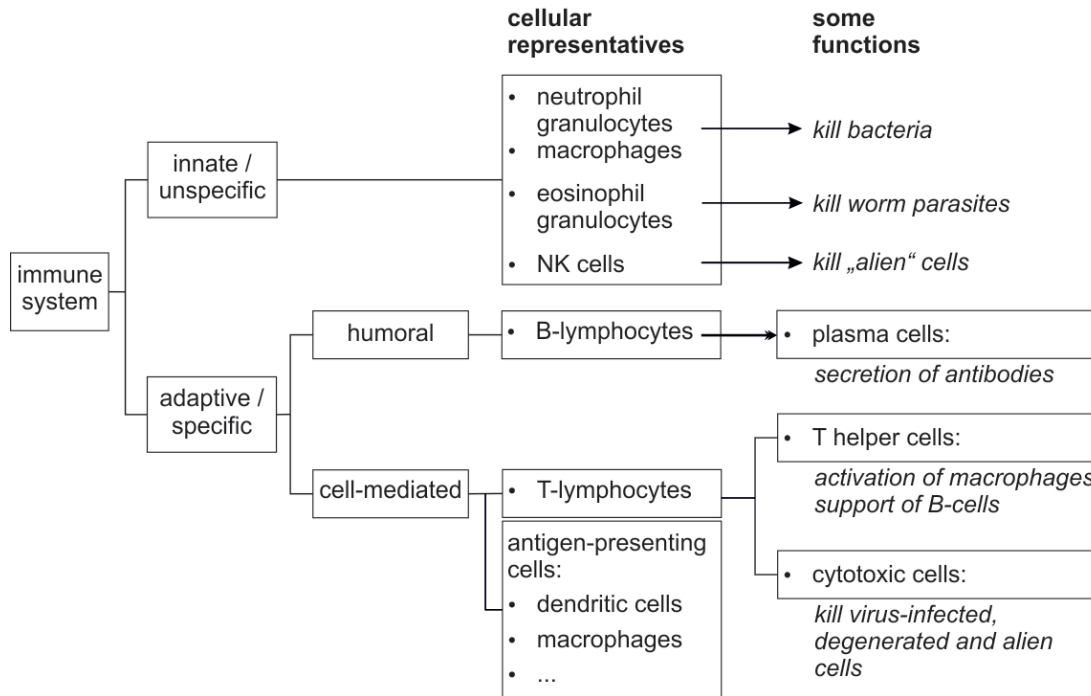


**Figure 2.1:** Schematic classification of the immune system with the two branches innate and adaptive immunity and their cellular representatives and functions.

cells. There are three fractions of lymphocytes: **B- and T-lymphocytes**, and **natural killer cells (NK cells)**. NK cells are large lymphocytes, B- and T-cells are small. NK cells belong to the innate immune system, while B- and T-lymphocytes are part of the adaptive immune system. All three lymphocyte populations emerge from the same population of progenitor cells in the bone marrow. B- and T-lymphocytes pass through a maturation process in different primary lymphatic organs (B: bone marrow; T: thymus), before they take up their function and populate the secondary lymphatic organs (lymph nodes, spleen, and mucosa-associated lymphatic tissue such as the Peyer's patches in the small intestine). Here, B- and T-lymphocytes preferentially populate different zones that accordingly are called B-zones or T-zones. An immune response involving T-lymphocytes is cell-mediated, while B-lymphocytes trigger secretion of 'humoral factors'. These antibodies (immune globulins, Ig) specifically bind harmful molecules (antigens) and thus render them harmless. Although they differ in their defensive strategies and function, B- and T-lymphocytes cannot be distinguished morphologically by standard histology. The work of lymphocytes in the specific im-

immune system is complemented by certain **antigen-presenting cells (APCs)**, such as **dendritic cells (DCs)** and **macrophages**.

Immune response with B- and T-cells to a new protein-like antigen typically takes 1-2 weeks time and follows - very much simplified - following steps:

- Recognition and binding of an antigen to a lymphocyte's receptor. T-cells therefore need the interaction with an antigen-presenting cell. This binding of an antigen leads to activation of the lymphocyte.
- Proliferation of activated lymphocytes.
- Differentiation of descendants from activated lymphocytes into effector cells, that carry out the defensive measure.
- Production of memory cells after successful defense.
- Termination of the immune response by apoptosis (controlled cell death) of many effector cells.

In contrast to B- and T-cell mediated specific immune response, the innate immune system reacts in a very short time (minutes) and thus is the 'first line of defense'. Cellular representatives are mainly **granulocytes**, macrophages and NK cells. Granulocytes are also referred to as **polymorphonuclear leucocytes (PMNs or PMNLs)** because of the variable shape of their cell nuclei. Further, **humoral factors**, such as cytokines that activate macrophages, play a crucial role. Depending on the staining-response of their protoplasm to standard histologic dyes, granulocytes are categorized into eosinophil, basophil and neutrophil granulocytes. **Neutrophil granulocytes** are the first immune cells to arrive at a lesion site, followed by macrophages that are attracted by cytokines. Cell organelles in the cytoplasm of neutrophil granulocytes contain a range of enzymes which enable them to dissolve injured or denatured cell and tissue substances and to phagocytose bacteria. Neutrophil granulocytes die by apoptosis, when their work is done, or when their short life-time (2-4 days) is over. Therefore, they must be continuously replaced by new cells.

In the case of laser-induced microlesions to epithelial surfaces, an immediate response of the innate immune system is expected. The in vivo mouse model in combination with two-photon excited autofluorescence microscopy used in this work provides

## 2. PHYSIOLOGY OF SMALL INTESTINAL MUCOSA

---

the unique possibility to study the immunologic processes of a complex organism with intact immune system on a microscopic scale. It should be possible to observe immigration of neutrophil granulocytes and possibly macrophages at locally induced lesions, because this first inflammatory reaction will likely occur within minutes after the laser damage. It is unlikely that the adaptive immune system will respond to this kind of damage, because small lesions of epithelia are a daily situation in the body, especially in the intestine. However, if pathogens invade through such a lesion, a more complex immune reaction including both lines of defense is needed. The branch of adaptive immunity is not observable in this work, owing to the long time spans of days to weeks needed.

### 2.2 Basic intestinal anatomy

The small intestine is with 5-6 m length the longest part of the digestive tract in humans. It consists of three segments: duodenum ( $\approx 30$  cm), jejunum ( $\approx 2$  m) and ileum ( $\approx 3$  m). The short duodenum can be clearly delineated from the following jejunum due to macroscopic as well as microscopic characteristics. In contrast, jejunum and ileum exhibit only slight differences in their mucosal composition, and there is a gradual transition between these segments without exact delineation.

The small intestinal mucosa is the surface layer of the intestinal wall and consists itself of three layers: the epithelium, the lamina propria (LP), and the muscularis mucosae. The epithelium is a single-layered, columnar cell layer and contains different, specialized cell types. Besides its regionally specialized functions, the epithelium always has the function of a diffusion barrier. Therefore neighboring epithelial cells are sealed together by 'adhesion complexes'. The epithelium rests on a basement membrane that separates the epithelium from the underlying lamina propria. The LP is a loose connective tissue that contains many cells and reticular collagen fibres. It houses the terminal branchings of nerves as well as blood and lymph capillaries. Many free immune cells constantly reside and move in the LP. The muscularis mucosae consists of smooth muscle cells and gives a certain mobility to the mucosa.

During passage through the small intestine, the food mass (chyme) is eventually dissociated into small molecules that are resorbed by the enterocytes of the intestinal epithelium, the topmost cellular layer, and then are further processed by the organism.

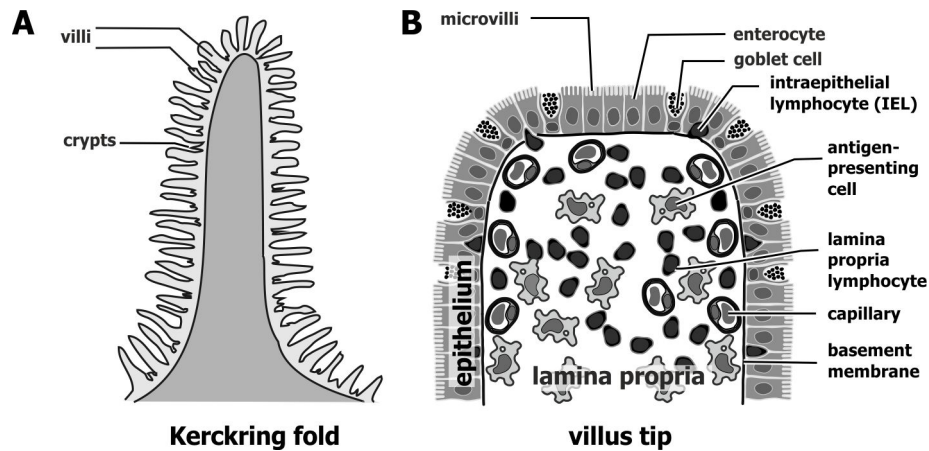


**Figure 2.2:** Schematic of three-fold surface enlargement in the small intestine. A Kerckring fold with villi and crypts is shown in **A**, while **B** is an enlarged view of a villus tip showing the microvilli-bearing enterocytes in the epithelium as well as the most important other cell types and structures.

Therefore the active surface of the small intestine is enlarged by two orders of magnitude through a special, three-step structural hierarchy of the intestinal mucosa (Fig. 2.2). First, the intestinal tube exhibits numerous circular folds, so-called Kerckring folds. These enlarge the surface from nominally  $0.3\text{ m}^2$  to  $\approx 1\text{ m}^2$ . The Kerckring folds are covered with tightly-packed finger-like projections of about 1 mm length, called villi, that again enlarge the surface by a factor of ten to  $\approx 10\text{ m}^2$ . However, the ultimate surface enlargement is due to a special form of the plasma membrane of enterocytes, which are the most abundant cell type in the intestinal epithelium. Enterocytes possess numerous hairlike extensions of their protoplasm, called microvilli. These microvilli again enlarge the functional surface by a factor of 20 to 40.

## 2.3 Selected functional compartments

### 2.3.1 Villi and crypts

Characteristic for small intestinal mucosa is the combination of villi and crypts. The prominent villi extend into the intestinal lumen and are areas of resorption, while the crypts are tubular invaginations of the epithelium and are locations of constant cell renewal.

## 2. PHYSIOLOGY OF SMALL INTESTINAL MUCOSA

---

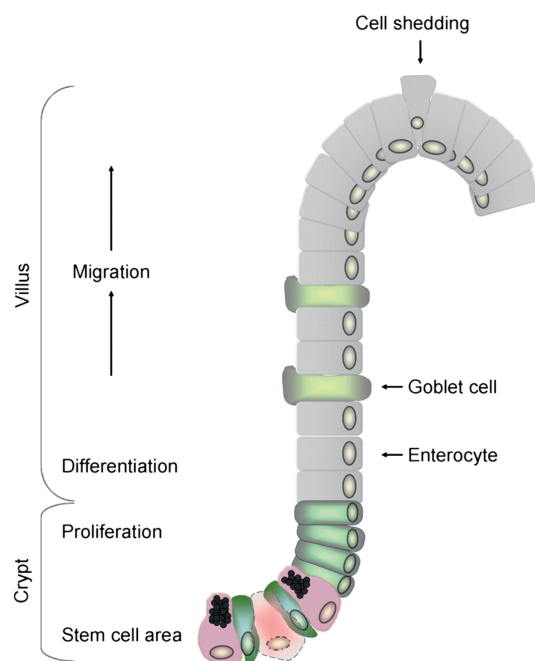


**Figure 2.3:** The intestinal epithelial layer from the crypt to the villus tip. New epithelial cells are constantly produced in the crypt region. They differentiate into different epithelial cells and take up their function while they gradually move to the villus tip. At the tip they die and are shed into the lumen. Figure reproduced from [Günther et al. 2012]

Figure 2.2 B shows the structure of an intestinal villus. Due to the resorptive function of villi, the most abundant cell type in the villus epithelium are enterocytes. These microvilli-bearing cells are specialized for resorption and directed transport of nutrients and liquids. Further in the villus epithelium one finds scattered goblet-cells, enteroendocrine cells and brush cells as well as intraepithelial lymphocytes (IELs). IELs are mainly regulatory T-cells of the adaptive immune system and constantly patrol in the basal part of the epithelium right above the basement membrane. They ensure the homeostasis of the intestinal epithelium [Chen et al. 2002] and protect against intestinal inflammation [Inagaki-Ohara et al. 2004, Tsuchiya et al. 2003]. In the villus lamina propria below the epithelium, numerous, freely motile immune cells are found that constantly manage the decision between inflammatory response and tolerance to substances in the gut lumen. These free immune cells are to a high fraction T-lymphocytes [Resendiz-Albor et al. 2004] but also antigen-presenting cells such as macrophages and

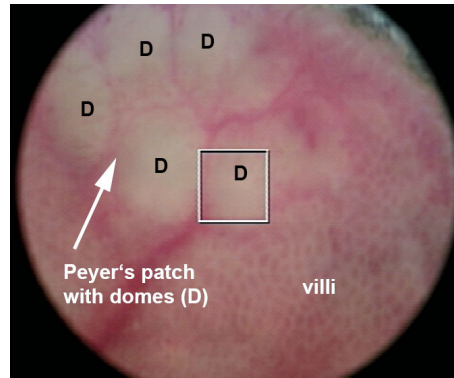


**Figure 2.4:** Murine small intestine as seen through the surgical microscope. A Peyer's patch with several dome areas is surrounded by numerous villi.

dendritic cells [Uematsu et al. 2008, Varol et al. 2009]. With the setup used in this work, it was possible for the first time, to directly observe and image individual lymphocyte-APC interaction in the lamina propria [Klinger et al. 2012]. Although immune cells of the specific immune system are always present, inflammatory cells such as neutrophil granulocytes, are not found in a healthy villus.

In the crypts, multipotent stem cells constantly generate new epithelial cells that differentiate into enterocytes, goblet cells and enteroendocrine cells while they move upward the crypt wall. The new epithelial cells then gradually migrate to the villus tip while they take up their function (Fig. 2.3) [Günther et al. 2012]. At the villus tip they finally die from anoikis, a special form of programmed cell-death, and are expelled into the intestinal lumen [Grossmann et al. 1998, Yuan and Kroemer 2010]. That way, every 4-5 days the whole epithelium is completely renewed. Because about 1400 cells are shed from a villus per day [Potten and Loeffler 1990], it is likely that this frequent event will be observable with in vivo two-photon excited fluorescence microscopy.

### 2.3.2 Peyer's patches

Near all mucosae one finds not only scattered lymphocytes but also organised lymphoid tissue. In the case of the small intestine one finds conglomerates of lymph follicles in the ileum, the so-called 'Peyer's patches', that constitute a secondary lymph organ. Figure 2.4 shows a Peyer's patch in murine small intestine. These Peyer's patches are part of the adaptive immune system and contain B-zones (follicles) as well as T-zones

## 2. PHYSIOLOGY OF SMALL INTESTINAL MUCOSA

---

(interfollicular regions). The epithelium on top of single lymph follicles ('domes') exhibits several characteristic features: The mucin layer is very thin, and enterocytes have only weak resorptive abilities. Between the enterocytes, the dome epithelium contains specialized cells, named M-cells, that take up antigens from the lumen [Gebert 1997, Wolf and Bye 1984]. Below the M-cells, contact of immune cells such as lymphocytes and antigen presenting cells with relevant antigens can then trigger a specific immune response [Brandtzaeg et al. 1999, Büning et al. 2006].

In this study, villus enterocytes and specific cell organelles in their cytoplasm as well as antigen-presenting cells in the lamina propria of villi and dome areas are first investigated to characterize their autofluorescence excitation-emission spectra. Due to their different functions, these cells/cell organelles contain different substances and exhibit different 'spectral fingerprints'. The second part of this work, focuses on the healing and immune response of the villus regions after laser-induced epithelial lesions.

# 3

## Methodical principles

In this chapter the theoretical foundations of two-photon microscopy and plasma-mediated laser nanosurgery are presented, both of which rely on nonlinear light-tissue interaction in slightly different irradiance regimes. The different parameter regimes for non-invasive imaging and invasive nanosurgery are briefly reviewed. Finally, an interferometric method for online-dosimetry of the laser-nanosurgical effects is described, that makes use of light reflection at the bubbles generated by a phase explosion at the laser focus.

### 3.1 Two-photon-excited fluorescence microscopy

#### 3.1.1 Fundamental working principle and specifications

Two-photon excited fluorescence microscopy has been established as a valuable tool in biology and life sciences soon after its first demonstration by Denk et al. [1990]. In this technique, fluorescent molecules are excited via simultaneous absorption of two near infrared photons that can deeply penetrate into the tissue. The process of two-photon absorption has theoretically been described already by Göppert-Mayer [1931]. But owing to the low cross sections involved, experimental demonstration was not realized until powerful lasers emitting ultrashort pulses were at hand that provided the high spatial and temporal photon density needed for this nonlinear process. In two-photon microscopy, the tightly focused excitation laser beam is scanned over the sample and the fluorescent light is collected at each scanning position with a photomultiplier tube.

### 3. METHODOICAL PRINCIPLES

---

For spectral imaging, the fluorescent light is split by a grating, a prism or dichroic mirrors into different wavelength channels that are each detected by a line detector or separate photomultiplier tubes. The total detected time-averaged fluorescence intensity  $\langle F(t) \rangle$  for each pixel depends on time-averaged laser power  $\langle P(t) \rangle$  and laser pulse duration  $\tau$  at the sample and is directly proportional to the two-photon absorption cross sections  $\sigma_{2P}$ , the concentrations  $C$  and the fluorescence quantum yield  $\eta$  of the fluorophores as well as to the detection quantum efficiency  $\phi$  of the system.  $\lambda$  is the excitation wavelength. For a single chromophore this is [Xu and Webb 1996]:

$$\langle F(t) \rangle \propto \phi \eta \sigma_{2P} C \frac{\langle P(r, t) \rangle^2}{\lambda \tau} \quad (3.1)$$

The product of the chromophore's fluorescence quantum yield  $\eta$  and its two-photon absorption cross section  $\sigma_{2P}$  is called two-photon action cross section  $\sigma'_{2P}$  and is experimentally more accessible than the pure two-photon absorption cross section.

From repeated scans of a stack of images of adjacent focal planes time-lapse volume images can be generated. Compared to confocal laser scanning microscopy that can also generate time-lapse and three-dimensional data with high resolution, two-photon microscopy has two main advantages. First, since infrared photons are used to excite the fluorophores, penetration depths of 100 – 400  $\mu\text{m}$  can be reached even in strongly scattering tissues [Durr et al. 2011, Helmchen and Denk 2005]. In conventional fluorescence microscopy, the chromophores are mostly excited using UV/blue wavelengths that are strongly scattered in biological tissue, which limits the optical penetration depth to a few tens of micrometers. Second, the nonlinear absorption process leads to an intrinsic depth selection, because only in the focal region the photon flux density is high enough to excite fluorescence. Hence, no additional pinhole is needed in the detection path of the microscope and, most notably, photodamage and photobleaching are confined to the focal region as well. Minimization of photodamage is essential especially for long-time in vivo studies of dynamic processes, in which the biological system should be perturbed as little as possible.

#### 3.1.2 Autofluorescence vs. molecular markers

In recent years, cell dynamics in a variety of complex living tissues have been studied using two-photon microscopy with exogenous markers and/or fluorescent proteins.

### 3.1 Two-photon-excited fluorescence microscopy

---

These include skin [Zinselmeyer et al. 2008], kidney [Dunn et al. 2002], and lymphatic tissue [Mempel et al. 2004]. Konjufca and Miller have reviewed the potential of two-photon microscopy as a tool to study the dynamics of host-pathogen interactions in vivo [Konjufca and Miller 2009]. In the intestine, two-photon microscopy with molecular markers has been used to study the epithelial barrier function in vivo [Watson et al. 2005], to shed light on the role of dendritic cell extension into the lumen for pathogen sampling and uptake [Chieppa et al. 2006], and to demonstrate goblet cell imaging as a marker for intestinal metaplasia of the stomach [Bao et al. 2010].

However, it has been shown that not only molecular markers but also autofluorescence from many endogenous chromophores can be two-photon excited within the tuning range of a Ti:Sapphire laser [Zipfel et al. 2003]. Additionally, the collagen framework of the extracellular matrix yields a second-harmonic signal of the focused femtosecond laser pulse at half the wavelength [Campagnola et al. 2002, Zoumi et al. 2002]. It has been demonstrated that, based on autofluorescence contrast, microscopic imaging of highly dynamic tissues is possible in vivo [Steven et al. 2008]. This opens the possibility to use autofluorescence for imaging general tissue morphology and to use additional molecular markers for specific questions beyond morphology, e.g. for functional imaging of metabolic states. Even more importantly, experimental complexity is reduced and the use of intrinsic fluorescence is expected to be less invasive to the organism than the use of molecular markers, which are usually phototoxic [Crawford and Braunwald 1991]. Further, as there are only a few FDA-approved fluorescence contrast agents, the use of autofluorescence is most promising for any future clinical application.

#### 3.1.3 Spectral imaging

Spectral information about cellular autofluorescence complements the morphological aspect of two-photon microscopy and can be used to delineate different structures in images of thick tissues with a submicron resolution without additional staining [Palero et al. 2007] or give a metabolic picture of the sample [Rocheleau et al. 2004]. Ti:Sapphire femtosecond lasers allow the excitation wavelength to be tuned in the range of 700-1000 nm and thus enable to use differences in the excitation spectra for discrimination

### 3. METHODOICAL PRINCIPLES

---

of fluorescent components. Further, the fluorescence emission can be spectrally analysed. By combining excitation and emission spectroscopy, two-dimensional spectral fingerprints of tissues and cells can be acquired [Chen et al. 2009, Radosevich et al. 2008].

In vivo autofluorescence excitation-emission fingerprinting with a limited number of spectral channels has been demonstrated for the relatively static and easily accessible tissue of skin [Radosevich et al. 2008], while cellular dynamics have been studied autofluorescence-based only without the additional benefit of spectral information [Steven et al. 2008]. It is still a challenge to apply spectrally resolved two-photon autofluorescence imaging to dynamic structures such as moving immune cells in the intestine under normal physiological conditions, because endogenous chromophores have a low two-photon absorption cross section [Huang et al. 2002, Zipfel et al. 2003] resulting in low signal. Furthermore, the maximum applicable excitation power that would improve imaging speed and image quality is limited by photodamage (Sect. 3.2.3).

## 3.2 Plasma-mediated laser nanosurgery

### 3.2.1 Optical breakdown and plasma formation

When ultra-short laser pulses are focussed with high numerical apertures into dielectric media, such as biological tissue, very high irradiances are reached, and energy deposition is governed no longer by linear absorption and scattering. Instead, light energy is deposited in the material by a complex interplay of different nonlinear, irradiance-dependent processes. In the case of two-photon microscopy, the nonlinear effect of simultaneous absorption of two photons is used to excite fluorescent molecules for tissue imaging. However, at higher irradiance values, the material in the focal volume is ionized and a plasma is formed. This process called optical breakdown is the basis for plasma-mediated laser nanosurgery whereas photoionization is an unwanted side-effect during nonlinear imaging.

Since cells consist of more than 80 % water, water is the most relevant model substance for a transparent dielectric in tissue surgery. Thus, optical breakdown in aqueous media has been extensively studied experimentally as well as theoretically

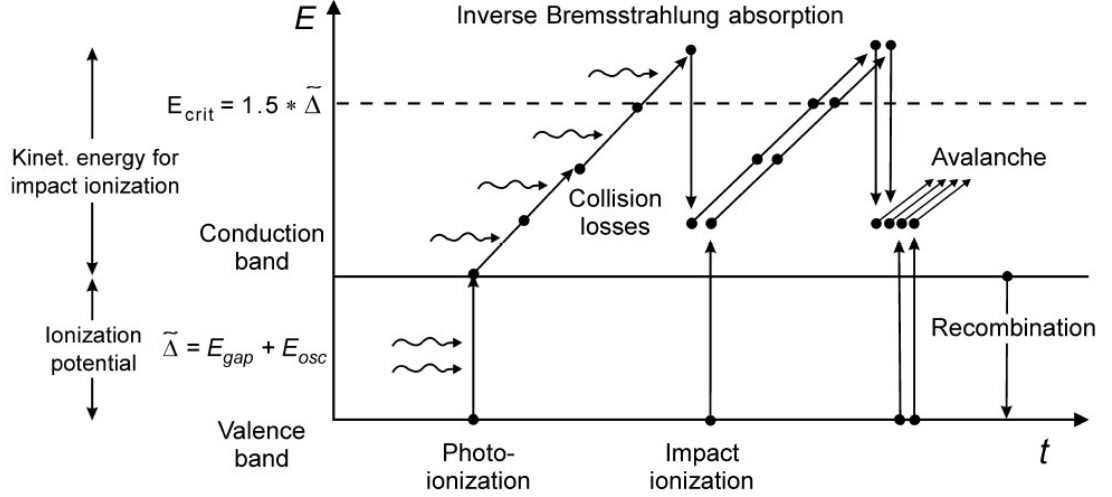


**Figure 3.1:** Interplay of photoionization, inverse Bremsstrahlung absorption, and impact ionization in the process of plasma formation during optical breakdown with fs laser pulses. The additional pathway of thermal ionization is not included, because this becomes relevant only for longer pulse durations. (Illustration from [Vogel et al. 2005]).

[Lauterborn 1974, Linz 2010, Sacchi 1991, Venugopalan et al. 2002, Vogel et al. 1996; 2005; 2008].

In order to describe plasma-formation during optical breakdown, water is usually regarded as an amorphous semiconductor with an energy bandgap of  $E_{\text{gap}} = 6.5$  eV between valence band and conduction band [Grand et al. 1979, Nikogosyan et al. 1983, Sacchi 1991, Williams et al. 1976]. Figure 3.1 illustrates the interplay of photoionization, tunnel ionization, impact ionization and inverse Bremsstrahlung absorption and recombination that are involved in plasma-formation in the focal volume. An electron in the valence band can be lifted into the conduction band (‘ionized’) either by photoionization (multiphoton absorption or tunneling) or by impact ionization. In order to generate quasi-free electrons in the conduction band, the bandgap energy plus the electron’s oscillation energy in the electric field, the effective ionization potential  $\tilde{\Delta}$ , must be overcome.

Once there is an electron in the conduction band, it can gain additional energy from the radiation field in a process called ‘inverse Bremsstrahlung absorption’. This is a non-resonant collision of an electron with a heavy particle (atom or ion) during which a photon is absorbed. Through recurring events of inverse Bremsstrahlung absorp-

### 3. METHODOICAL PRINCIPLES

---

tion the electron can gain enough kinetic energy to ionize another electron by impact ionization. Sufficient energy is accumulated, when the kinetic energy of the impacting electron is larger than the effective ionization potential  $\tilde{\Delta}$  in order to satisfy energy and momentum conservation laws. Now there are two quasi-free electrons that can in turn undergo inverse Bremsstrahlung absorption and transfer their energy to more electrons by collisions and so on. This amplification auf quasi-free electrons is called ‘avalanche ionization’ or ‘cascade ionization’.

The generation of quasi-free electrons by avalanche and photo-ionization is counteracted by recombination and by diffusion out of the focal volume during the laser pulse. Electron diffusion is a relatively slow process ( $\approx$  ps), which is most important for long pulse durations (several ns) and small focal volumes corresponding to large numerical apertures. Recombination of electron-hole pairs occurs on a picosecond time scale and reduces the density of quasi-free electrons  $\rho$  in the conduction band. Since recombination requires two particles - an electron and a hole - the recombination rate is proportional to  $\rho^2$ . Especially for high electron densities, the recombination process can thus stop avalanche ionization that is only proportional to  $\rho$ , before full ionization is reached.

Electron recombination and collisions with heavy particles lead to thermalization of the energy deposited in the medium, thus causing a temperature increase in the focal volume. At sufficiently high temperatures thermal ionization of electrons sets in. The thermalization time is on the order of several picoseconds. Thus, for femtosecond laser pulses thermal ionization does not contribute to the generation of quasi-free electrons. However, for picosecond and nanosecond pulses there is sufficient time for causing a considerable temperature increase in the focal volume, and thermal ionization will support avalanche ionization in driving the breakdown process. When the irradiance is high enough, thermal ionization will generate more quasi-free electrons than are lost by recombination and diffusion, and full ionization in the laser focus can be reached.

Consequently, temporal dynamics and irradiation thresholds of plasma-formation are different for fs and ns optical breakdown.

With fs pulses, very high irradiances  $I$  are needed to complete optical breakdown during the short pulse duration. The probability for multiphoton absorption of  $n$  photons depends on the irradiance as  $I^n$ . Therefore, multiphoton ionization will always

provide enough start electrons for cascade ionization. Thus, by adjusting the laser pulse energy, plasma-size and the resulting plasma-induced effects such as bubble formation can be precisely tuned in a continuous fashion.

Recently Linz [2010] and Vogel et al. [2010] discovered that minute cavitation bubbles as small as those created by fs pulses can be produced also by ns laser pulses at ultraviolet (UV) or visible (VIS) wavelengths, if these pulses exhibit a smooth (Gaussian) pulse shape. They showed that the optical breakdown with ns pulses is a two-step process. In the first step, at low pulse energies, a low-density plasma is produced, because recombination counteracts avalanche ionization and prevents full ionization to be reached. This low-density plasma regime results in very small cavitation bubbles with maximum radii between 150 nm and 30  $\mu\text{m}$ . The second step occurs abruptly at pulse energies 1.5 to 30 times larger than the bubble formation threshold (depending on pulse duration and wavelength). At these energies, the irradiance is so high that the temperature in the laser focus reaches a value at which thermal ionization sets in that intensifies avalanche ionization. At the transition to ‘thermal runaway’ of the breakdown process, the plasma suddenly assumes a much larger size, bright plasma luminescence is observed, and much larger bubbles are produced. Linz et al. [2010] showed that the energy range in which small bubbles can be produced is much larger for ns than for fs pulses. This is advantageous for nanosurgery, because it enables a higher tunability of the desired size of the surgical effect.

### 3.2.2 Plasma-induced events

The plasma that is generated in the focal volume during optical breakdown causes a series of effects in the material or tissue.

Already in the low-density plasma regime, quasi-free electrons will cause chemical alterations of tissue molecules either directly or due to generation of reactive oxygen species that affect organic molecules [Boudaiffa et al. 2000, Vogel et al. 2005].

Thermal tissue effects do not play a critical role for optical breakdown with ultrashort laser pulses. Pulse series from a fs oscillator at 80 MHz repetition rate will produce a temperature increase sufficient for thermal denaturation only at irradiances at which about  $10^6$  quasi-free electrons are generated during a single pulse. Thus, before thermal denaturation of tissue molecules can occur, the free electrons will have

### 3. METHODOICAL PRINCIPLES

---

already caused strong chemical effects. Thus, chemical effects by quasi-free electrons will probably dominate [Vogel et al. 2005].

For fs laser pulses, the thermalization time is much shorter than the acoustic transit time from the laser focus to its periphery. Thus, no acoustic relaxation is possible during fs laser pulses, and the thermoelastic stress stays confined to the focal region leading to a massive pressure rise. In turn, a stress wave is emitted that consists of both of a compressive and tensile part in order to comply with energy and momentum conservation laws. This stress wave can lead to a fracture of the material, even if the temperature in the focal volume is not sufficiently high to cause thermal denaturation. In water, the tensile stress wave will cause the formation of a cavitation bubble when the tensile strength of the liquid is exceeded [Vogel et al. 2005].

For ns laser pulses, there is no pressure confinement, and bubble formation starts when the temperature for the superheat limit of water at ambient pressure is reached (300°C). At this temperature there will be necessarily a phase transition in form of explosive vaporization [Vogel and Venugopalan 2003, Vogel et al. 2008].

Well above bubble formation threshold, the plasma assumes energy densities as high as 10-40 kJ/cm<sup>3</sup> within a very short time resulting in very high temperature and pressure values in the focal volume. This rapid temperature and pressure increase results in explosive expansion of the plasma with emission of a shock wave that, in turn, leads to formation of cavitation bubbles that are much larger than the bubbles at threshold. In this regime, the mechanical forces exerted by the cavitation bubble will determine the size of the disrupted region in tissue [Vogel et al. 1996].

#### 3.2.3 Transition from imaging to surgery

It was shown in the last sections that nonlinear light-tissue interaction can result in different effects ranging from non-invasive imaging to destructive cell surgery depending on the irradiance regime. In figure 3.2 these different working regimes are indicated in terms of irradiance and focal electron density calculated for pulses with 170 fs pulse duration and 800 nm wavelength [Vogel et al. 2005]. The irradiance is normalized to the value  $I_{rate}$  at which an electron density of  $10^{21}$  cm<sup>-3</sup> is reached with a single pulse. This electron density serves as the threshold criterion for optical breakdown in numerical models. The bubble formation threshold with single pulses typically lies at irradiance

### 3.2 Plasma-mediated laser nanosurgery

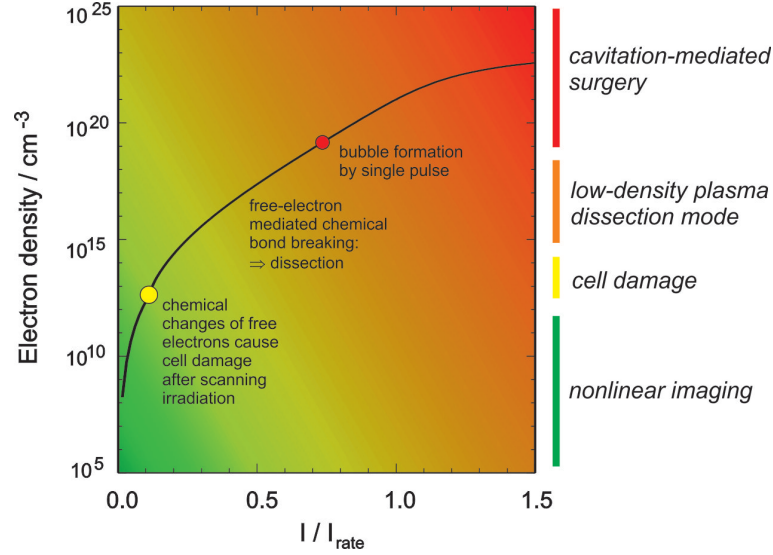


**Figure 3.2:** Effects of fs-breakdown with increasing irradiance. Free electron density in the focal volume as function of irradiance for 170 fs, 800 nm [Vogel et al. 2005].

values  $0.8 \times I_{rate}$ , corresponding to pulse energies between 10 and 30 nJ, depending on the numerical aperture used. Examples for this regime are the work of Yanik et al. [2004] who employed amplified fs-pulses at 1 kHz repetition rate to study functional regenerations of axons after axotomy, and the work of Nishimura et al. [2006] who used photodisruption of small blood vessels by ultrashort laser pulses to establish models of stroke in rats.

Nanosurgery based on cavitation bubbles produced with ultraviolet nanosecond laser pulses has been used to cut subcellular structures such as the cytoskeleton and to study relaxation processes in cells and developing organisms [Colombelli et al. 2004; 2007, Hutson and Ma 2007].

Irradiances below bubble formation threshold ranging down to about 15 % of the threshold value enable to perform tissue dissection by cumulative chemical effects mediated by free electrons or multiphoton-absorption. In this regime, the effects are essentially confined to the focal volume and thus enable submicrometer precision cuts at arbitrary locations. Examples are the studies of neural network in the brain [Sacconi et al. 2007], intranuclear chromosome dissection [König et al. 1999b], or the modulation of morphogenetic movements in *Drosophila* embryos [Supatto et al. 2005].

Even lower irradiances are used for nonlinear imaging of tissues. As has already

### 3. METHODOICAL PRINCIPLES

---

been described in Sect. 3.1, multiphoton-excited fluorescence microscopy is becoming ever more widely used, because it provides a method of non-invasive imaging of live tissues. However, the irradiance range for safe imaging is narrow ( $< 0.1 I_{rate}$ ), and the transition from nondestructive imaging to irradiance regimes that induce photodamage during imaging is fluent [Hopt and Neher 2001, Hovhannisyanyan et al. 2008, Koester et al. 1999, König et al. 1995; 1999a]. Photodamage during time-lapse 2PAM of murine intestine is presented and discussed in section 5.4 of this thesis.

## 3.3 Online-dosimetry by bubble interferometry

### 3.3.1 Bubble monitoring by probe beam scattering

The threshold for cavitation bubble formation defines the onset of disruptive mechanisms contributing to manipulation and dissection of cells. The spatial extent of plasma-mediated surgical effects is determined by the size of the cavitation bubble produced during plasma expansion [Hellman et al. 2007, Hutson and Ma 2007, Vogel et al. 1996]. For that purpose, precise control and knowledge of the cavitation bubble size are essential in order to achieve the desired size of effects in cell surgery.

Online dosimetry of the laser-induced effects requires, therefore, the ability of monitoring the dynamics and size of laser-induced cavitation bubbles in real time. Close to bubble formation threshold, bubble radii are smaller than the diffraction-limited focal spot of the focussed laser beam that is used to produce them [Vogel et al. 2005]. Further, the time from bubble expansion to collapse, the bubble oscillation time  $T_{osc}$ , is on the order of only several ten nanoseconds for the smallest bubbles. In order to detect such small bubbles and determine their maximum radius  $R_{max}$ , a probe-beam scattering technique has been developed by Vogel et al. [2008]. A continuous-wave laser beam with visible wavelength (probe) is focussed collinearly and confocally with the laser that induces optical breakdown (pump) in a water-filled cuvette as depicted in Fig. 3.3 A. Generation of a cavitation bubble in the laser focus results in a scattering signal that is linked to the bubble's size and readily allows to identify both the onset of bubble expansion and the time of collapse. The time interval between these events defines the bubble oscillation time  $T_{osc}$ . The first bubble oscillation cycle is often followed by several subsequent oscillations until the bubble energy is dissipated by shock

### 3.3 Online-dosimetry by bubble interferometry

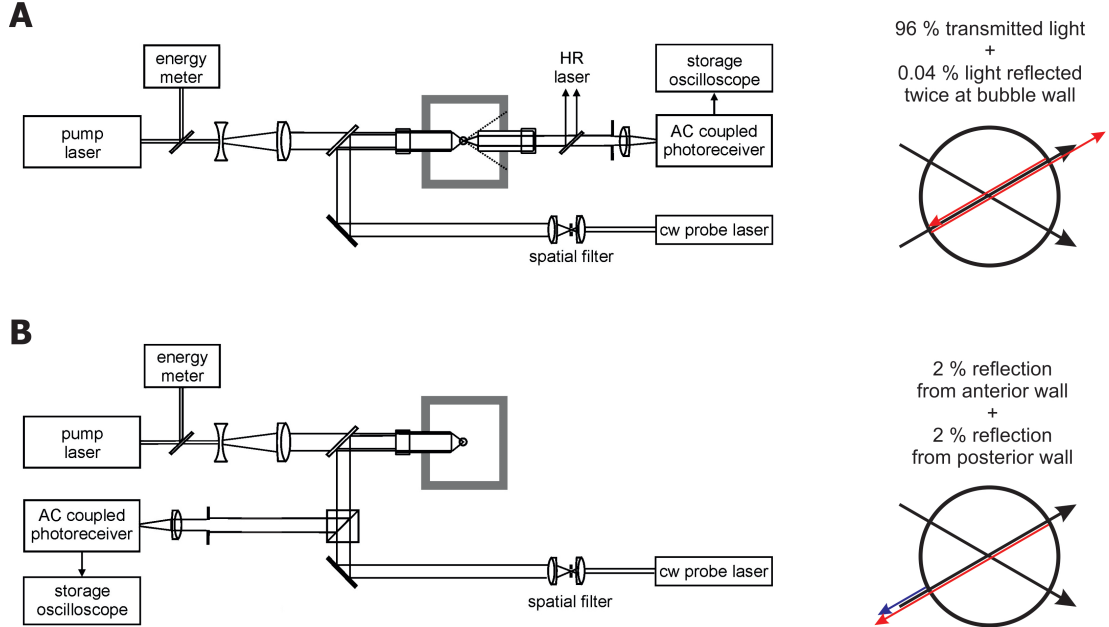


**Figure 3.3:** Light scattering techniques for online monitoring of cavitation bubble dynamics and size in transmission (A) and reflection (B).

wave emission and viscous damping. All oscillations are visible in the scattering signal. The maximum bubble radius  $R_{max}$  can be calculated from the oscillation time  $T_{osc}$  as described in section 3.3.2.

Use of the forward scattering signal for bubble detection provides a good signal to noise ratio because of the heterodyne gain arising from coherent mixing of the scattered light with the directly transmitted light. For bubbles much smaller than the focal diameter, the scattering signal is considerably weaker than the total amount of transmitted light. AC-coupling can remove the bias and makes it possible to detect small bubbles well below the optical resolution limit. The light scattering technique provides reliable results for bubbles with only 15 ns oscillation time and 150 nm maximum radius.  $T_{osc}$  can be measured with about  $\pm 1$  ns accuracy, corresponding to an accuracy for  $R_{max}$  of  $\pm 10$  nm [Vogel et al. 2008].

For online dosimetry of nanosurgery in a living animal, forward-detection is not possible, and the probe beam scattering has to be used in backreflection as shown in Fig. 3.3 B. In this geometry, scattering signals are weaker than in transmission, because only about 2 % of the incident light is reflected at the liquid-gas interface of the bubble

### 3. METHODOICAL PRINCIPLES

---

wall. Nevertheless, the scattering signal again allows to determine the bubble size  $R_{max}$  by determination of  $T_{osc}$  [Linz et al. 2013].

Although the backscattering signal is weaker, it contains more useful information than the transmission signal. Equal amounts of the probe laser light are reflected at the front and back surface of the bubble, and both components interfere at the detector. During the bubble oscillation the interference signal changes, because the pathlength difference between both components varies as the bubble expands and collapses. The modulation of the backscattering signal thus contains information about the radius-time curve  $R(T)$  while its duration provides information about  $T_{osc}$  and  $R_{max}$ .

#### 3.3.2 Determination of bubble size and dynamics from the scattering signals

Figure 3.4 shows scattering signals that were recorded in transmission (A) and reflection mode (B) as described above. The experimentally accessible oscillation time  $T_{osc}$  is indicated for both signals. The maximum bubble radius  $R_{max}$  cannot be determined directly from the scattering signals. It is calculated from the oscillation time  $T_{osc}$  by the Rayleigh-formula:

$$R_{max} = \frac{T_{osc}}{1.83} \sqrt{\frac{p_{stat} - p_v}{\rho_{liq}}} \quad (3.2)$$

where  $p_{stat}$  is the hydrostatic pressure,  $\rho_{liq}$  is the liquid density, and  $p_v$  is the vapor pressure inside the bubble (2330 Pa at 20 °C).

Once the maximum bubble radius is determined, the interference fringes on scattering signals recorded in reflection mode allow to determine radius-time curves for the bubble oscillation. Each complete fringe corresponds to a pathlength difference of  $\Delta l = \lambda = 2\Delta d$  and thus a diameter change of  $\Delta d = \lambda/2$  or a radius-change of  $\lambda/4$ . During expansion, the bubble wall velocity decreases until the maximum radius is reached and then is accelerated again. This is reflected in a frequency decrease and increase of the interference fringes. The time at which the bubble has reached its maximum expansion,  $T_{exp}$  is characterized by the lowest fringe frequency and can be easily determined from the scattering signal (Fig. 3.4 (B)) Thus, starting from  $R_{max}$  at  $T_{exp}$ , radius-time curves of the bubble oscillation dynamics can be obtained with a spatial resolution as high as  $\lambda/8$ , if fringe minima and maxima both are evaluated. The time

### 3.3 Online-dosimetry by bubble interferometry

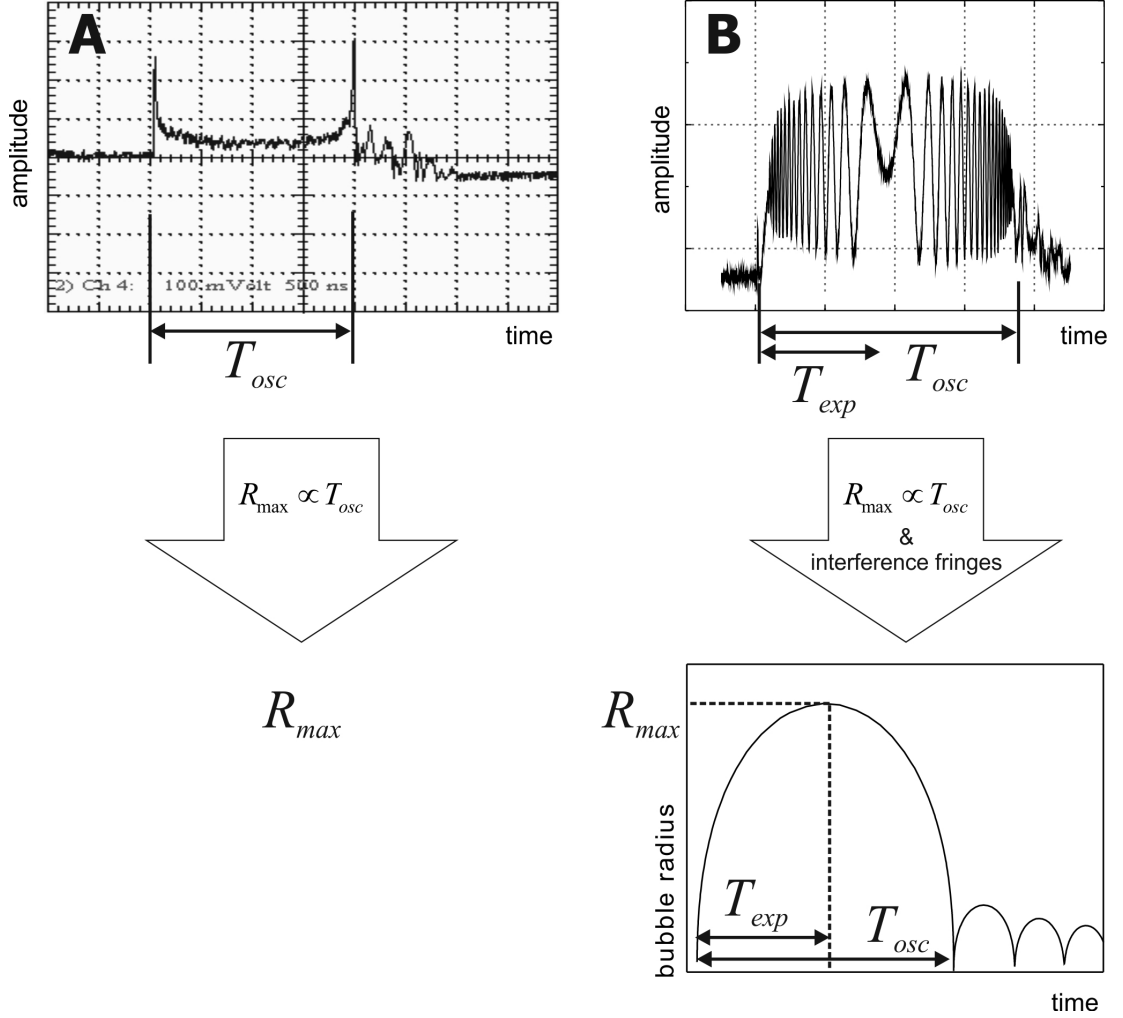


**Figure 3.4:** Qualitative illustration of the determination of the oscillation time  $T_{osc}$  from scattering signals recorded in transmission (A) and reflection mode (B). The maximum bubble radius  $R_{max}$  is then calculated from  $T_{osc}$  using Eq.3.2. In reflection mode, additionally radius-time curves can be determined starting from  $R_{max}(T_{exp})$  using the information contained in the interference fringes.

resolution is determined by the bandwidth of the photodetector and oscilloscope used. In the setup used in this thesis, the photodetector's bandwidth was 200 MHz allowing a time resolution of 5 ns.

However, Eq. 3.2 is not correct for bubble sizes below a few micrometers, because it neglects the surface tension that produces a pressure scaling inversely proportional to the bubble radius, which adds to the hydrostatic pressure. Surface tension counteracts

### 3. METHODOICAL PRINCIPLES

---

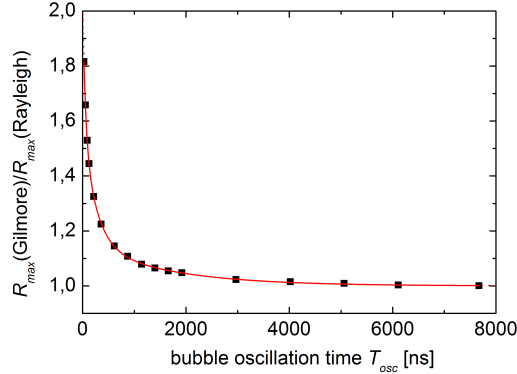


**Figure 3.5:** Ratio  $R_{Gilmore}/R_{Rayleigh}(T_{osc})$  of the maximum bubble radius calculated with the Gilmore model to the maximum bubble radius calculated with the Rayleigh model from the oscillation time  $T_{osc}$  [Vogel et al. 2008]. The Gilmore model was modified to include the temperature dependence of surface tension. An analytic function  $f(T_{osc})$  as described by Eq. 3.3 was fitted to the  $R_{Gilmore}/R_{Rayleigh}$  values.

bubble expansion and accelerates collapse, and for a given oscillation time,  $R_{max}$  is larger under the influence of surface tension. A correction factor  $f(T_{osc})$  has been presented and experimentally validated by Vogel et al. [2008]. It was derived by comparing the results of Eq. 3.2 with the outcome of a modified Gilmore model [Gilmore 1952] of laser-induced bubble dynamics that considers both surface tension at the bubble wall and its temperature-dependence.

The correction factor by which the radius value determined through Eq. 3.2 must be multiplied to obtain the exact  $R_{max}$  value is plotted in Fig. 3.5. It can be approximated by the analytical equation:

$$f(T_{osc}) = 0.43238 \cdot e^{\frac{-T_{osc}}{248.2074}} + 0.47292 \cdot e^{\frac{-T_{osc}}{49.01347}} + 0.15773 \cdot e^{\frac{-T_{osc}}{1589.40295}} + 1 \quad (3.3)$$

Figure 3.5 shows that for very small bubbles the actual radius corresponding to a given oscillation time is almost twice as large as predicted by the Rayleigh model that does not consider surface tension.

In biological tissue, visco-elastic-plastic material properties will further modify cavitation bubble dynamics and reduce the maximum bubble radius as will be discussed in detail in Sect. 6.1. Further, the bubble collapse is prolonged due to viscous damping, leading to increased bubble oscillation times [Brujan and Vogel 2006]. Using the

### 3.3 Online-dosimetry by bubble interferometry

---

prolonged oscillation times in calculation of the maximum bubble radii would lead to erroneous results. However, a reasonable value for  $R_{max}$  can still be obtained by defining a virtual oscillation time  $T'_{osc} = 2T_{exp}$  based on the the bubble expansion time  $T_{exp}$  (Sect. 6.1).

### **3. METHODICAL PRINCIPLES**

---

# 4

## Experimental setup and methods

In this chapter first the in vivo mouse model is introduced that is the fundamental experimental environment for this thesis. Then the experimental setup for spectrally-resolved two-photon microscopy is presented, and the methods for quantitative image analysis are described. Thereafter, the experimental setup for UV-laser nanosurgery with online-dosimetry of the induced cavitation bubbles using a backscattering technique is described. Finally, the applied staining protocols for molecular markers are briefly summarized.

### 4.1 Mouse model

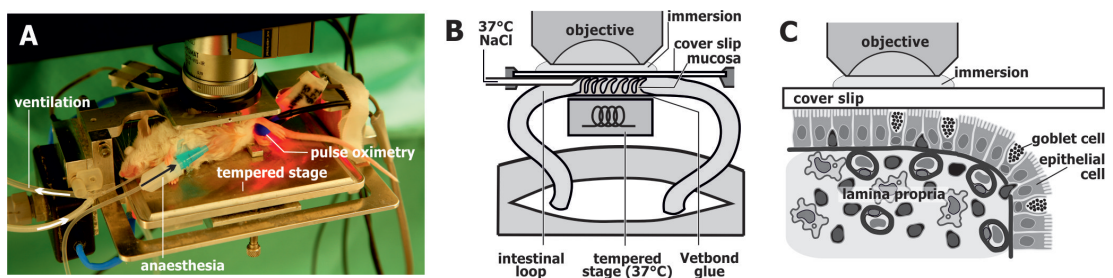


**Figure 4.1:** Setup for the investigation of murine intestinal mucosa in vivo. (A) Anaesthetised balb/c mouse with ventilation and pulse oximetry on a homeothermic table. (B) Schematic drawing of the topology for accessing the intestinal mucosa with the water immersion microscope objective. (C) Schematic diagram of the intestinal mucosa with exemplarily marked imaging and surgical focus plane (not true to scale).

Female Balb/c mice (n=9 for autofluorescence spectra, n=12 for UV nanosurgery),

## 4. EXPERIMENTAL SETUP AND METHODS

---

8 to 10 weeks of age, were purchased from Charles River Laboratories and kept under standard conditions with free access to food and water. Animals were anaesthetised by intraperitoneal injection of a combination of Fentanyl (Bayer), Midazolam (Curamed) and Medetomidin (Pfizer). After assuring adequate anaesthesia, the mouse was placed on a homeothermic table for surgery and later experimental handling. Then a tracheostomy was performed and the mouse was connected to a ventilator (Hugo Sachs Elektronik & Harvard Apparatus GmbH). The abdominal cavity was opened and an intestinal loop was gently protruded. The loop was fixed onto a heated block with temperature-control using Vetbond glue (3M) and opened lengthwise so as to press the luminal side of the tissue slightly against a fixed microscope coverslip. This procedure minimized movement artifacts due to peristalsis. The mouse on the tempered stage was then placed under the microscope objective as shown in Fig. 4.1. Fig. 4.1 C shows a schematic of a segment of an intestinal villus subject to the experimental investigations. During all procedures, the small intestine was constantly moisturized with 37 °C-warm NaCl solution, and core body temperature was maintained at 37 °C. To prevent heat drain through the microscope objective, it was equipped with an objective heating. The tissue was constantly perfused, as seen by erythrocyte movement phenomena, and cells remained fully motile with no evidence of decreased viability for experiments lasting up to eight hours. During the experiment, the subject's vital parameters were monitored with a pulse oximeter at the tail vein (MouseOx, Starr Life Sciences). The animal experiments were approved by the local government (V742-72241.122).

### 4.2 Spectrally resolved two-photon microscopy

Autofluorescence imaging was done with a modified commercial two-photon microscope (DermaInspect, JenLab GmbH). Fig. 4.2 shows a schematic of the setup. The fluorescence excitation source was a femtosecond Ti:sapphire laser tunable between 710-920 nm, with a pulse repetition rate of 80 MHz (MaiTai, Newport Spectra-Physics). A Zeiss 40 × /1.2 w C-Apochromat objective was used to focus the excitation light into the sample and collect the fluorescence light. The field of view was 150 × 150  $\mu\text{m}^2$  and scanned in subsequent horizontal lines resulting in an image of 512 × 512 pixels.

For imaging with spectral separation of the emission light, a four-channel spectral detector was inserted into the fluorescence path consisting of four photomultiplier tubes

## 4.2 Spectrally resolved two-photon microscopy

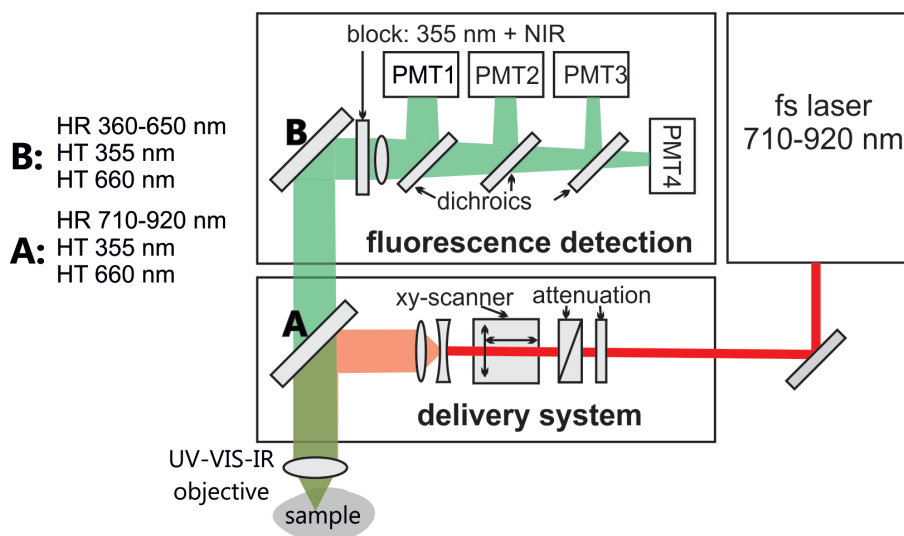


**Figure 4.2:** Setup for spectrally resolved imaging by two-photon excited fluorescence microscopy. PMT = photomultiplier tube, exp. = beam expander, cw = continuous wave mode, HR = highly reflecting, HT = highly transmitting.

(PMTs 1 and 2: R1294A, PMTs 3 and 4: R1295A, Hamamatsu Photonics) and a set of dichroic filters (ST440DCXR, HC-BS495, ST580DCXR, AHF Analysentechnik AG). The dichroic filters were chosen such as to provide a good separation between known fluorescence emission spectra of endogenous fluorophores.

Of particular interest is a separation of the reduced forms of nicotinamide adenine dinucleotides (NAD(P)H) from other chromophores. NAD(P)H is crucial for the cell metabolism and is found in high concentrations at the mitochondria [Piston and Knobel 1999]. Enterocytes are metabolically very active and thus contain in the cytosol many mitochondria for synthesis of adenosine tri-phosphate. In order to spectrally characterize the four detection channels, transmission measurements of all optical elements except for the objective were performed. Transmission data of the manufacturer were used for the microscope objective. Figure 4.3 shows the spectral characteristics of our fluorescence detection system including detector quantum efficiency in comparison to emission spectra of endogenous fluorophores as reported in [Mochizuki et al. 1995, Wagnières et al. 1998].

From the intensity images recorded in the four spectral channels, false-color images were produced. It was found by Palero [2007] that maximum contrast of autofluorescent

## 4. EXPERIMENTAL SETUP AND METHODS

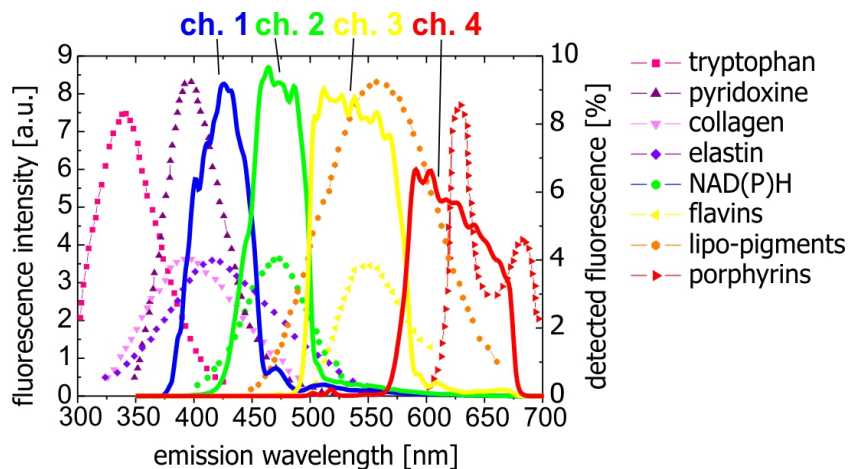


**Figure 4.3:** Spectral detection probability of the four detection channels including the transmission of all optical elements and the quantum efficiency of the photomultipliers (solid lines, right axis). For comparison, emission spectra of important endogenous chromophores as reported in [Mochizuki et al. 1995, Wagnières et al. 1998] are also shown (symbols, left axis). NAD(P)H: nicotinamide adenine dinucleotide and nicotinamide adenine dinucleotide phosphate.

structures with different emission spectra is obtained, when the false colors are chosen as close as possible to the natural colors of the fluorescence light. However, when no additional fluorescence stains were used, this color-mapping did not yield sufficient contrast between the different autofluorescent tissue components studied in this work (enterocytes and antigen-presenting cells). Therefore, in order to bring out the fine differences in spectral autofluorescence, the colors were chosen to be: blue for channel 1,  $\lambda \approx 380\text{-}450$  nm; green for channel 2,  $\lambda \approx 450\text{-}500$  nm; red for channel 3,  $\lambda \approx 500\text{-}580$  nm; pink for channel 4,  $\lambda \approx 580\text{-}680$  nm. Figure 4.4 shows exemplarily the intensity images of an intestinal villus as they appear in the four spectral channels and the false-color image composed from these four images with this color-map-1.

However, when red fluorescent dyes were used, maximum contrast was desired between tissue autofluorescence (blue-green) and stains (red-orange). Therefore colors were chosen to make autofluorescence appear blue-green and stains red-orange in the images: blue for channel 1, green for channel 2, yellow for channel 3, red for channel 4. Throughout the figures, this color-map will be indexed with color-map-2.

To obtain excitation spectra, subsequent images of the same structure were recorded while the two-photon excitation wavelength was varied between 730-910 nm. For each

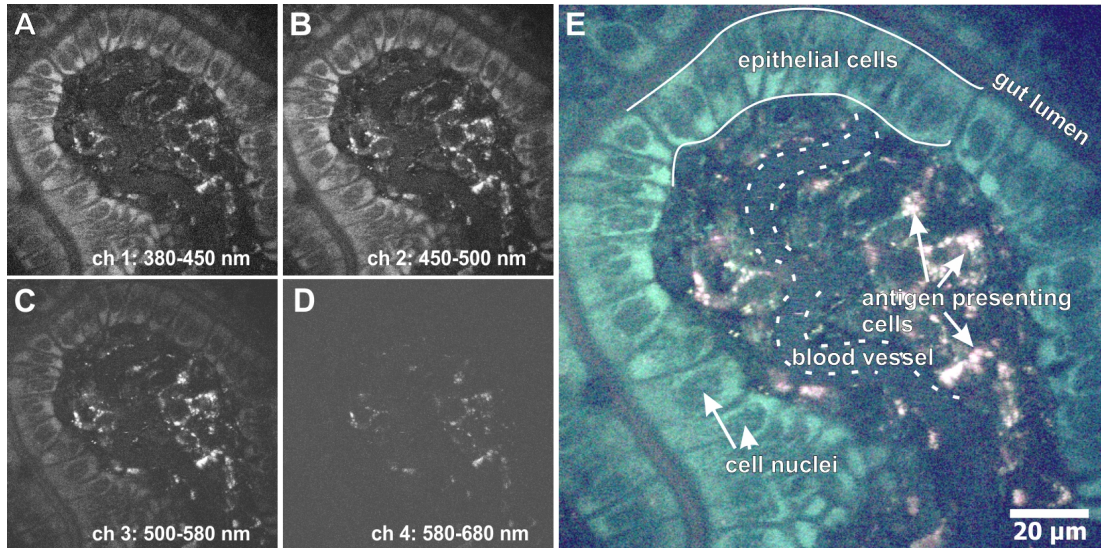


**Figure 4.4:** Optical section through a villus recorded in four spectral channels (A-E) and composed false-color image (F). (color-map-1).

excitation wavelength, the average laser power at the sample was adjusted such that the autofluorescence signal of all relevant biological structures was above the noise level, while staying below the threshold for photodamage. Acquisition times of 7.4 or 13.4 seconds were required to record single images.

### 4.3 Image analysis

In order to spectrally distinguish different cells and cell organelles, one is interested in the material-specific fluorescence intensity characteristics as a function of excitation and emission wavelength. As is evident from equation 3.1, for an excitation wavelength  $\lambda_{ex}$ , the total recorded fluorescence intensity of a single chromophore is directly proportional to the product of two-photon action cross section  $\sigma'_{2P}(\lambda_{ex})$  and the concentration  $C$  of the chromophore in the sample. This product is specific for each sample. All other factors in the equation are inherent to the imaging system and apply equally to all samples.

In cells, a mixture of different chromophores is expected to contribute to the fluorescence intensity in each pixel. Following eq. 3.1, the sum of these contributions can

#### 4. EXPERIMENTAL SETUP AND METHODS

---

be described as:

$$\langle F(t) \rangle \propto \frac{\langle P(r, t) \rangle^2}{\lambda_{ex} \tau} \sum_i \sigma'_{2P_i}(\lambda_{ex}) C_i \quad (4.1)$$

Laser excitation power and pulse duration vary with excitation wavelength. In order to calculate the cell- or cell organelle-specific fluorescence intensity as a function of excitation wavelength, we thus need to correct the measured fluorescence intensity for the mean power  $\langle P \rangle$  at the sample and the laser pulse duration  $\tau$  and excitation wavelength  $\lambda_{ex}$ :

$$\langle F(t)_{corr} \rangle = \langle F(t) \rangle \frac{\lambda_{ex} \tau}{\langle P(r, t) \rangle^2} \propto \sum_i \sigma'_{2P_i}(\lambda_{ex}) C_i \quad (4.2)$$

The laser pulse duration  $\tau$  was measured by means of an autocorrelator (PulseCheck, APE GmbH, Berlin, Germany) at a location where the pulses were transmitted through the microscope but had not yet entered the objective (Fig. 4.5). The pulse duration was obtained by fitting the autocorrelation function to a  $\text{sech}^2$ -function. Measurement of the emission spectra of the laser confirmed that the pulses were Fourier transform limited. To account for pulse broadening in the two-photon microscope, the group delay dispersion (GDD) of the DermaInspect and the objective were determined experimentally (Fig. 4.6). Then the pulse length  $\tau'$  after transmission through the entire microscope was calculated using the GDD-values:

$$\tau' = \tau \sqrt{1 + \left( \frac{4 \ln(2) GDD}{\tau^2} \right)^2} \quad (4.3)$$

However, for wavelengths longer than 890 nm, the laser intensity was too small to determine the GDD after transmission through the DermaInspect. Therefore, only data up to this wavelength were used for evaluation of the fluorescence emission spectra.

The mean excitation laser power at the sample was measured after each experiment using an integrating sphere (model no. 69, Delta Developments). As direct measurements with the water immersion objective were not possible, we measured the power entering the back entrance pupil of the objective. This was achieved by using an aperture stop of the same size as the back aperture of the objective and measuring the power behind this aperture. Data were then corrected for the objective's transmittance as provided by the manufacturer.

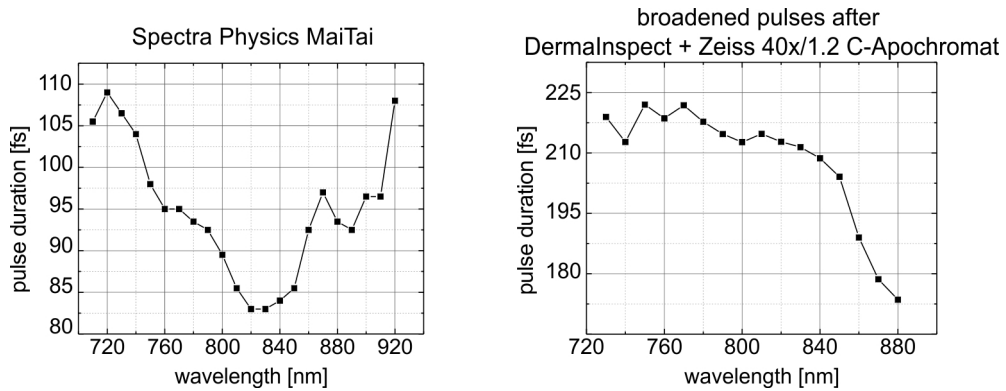


**Figure 4.5:** Left: Measured pulse duration of the infrared fs laser (MaiTai, Spectra Physics) used for two-photon imaging. Right: Calculated pulse duration after transmission through the two-photon microscope and the objective.

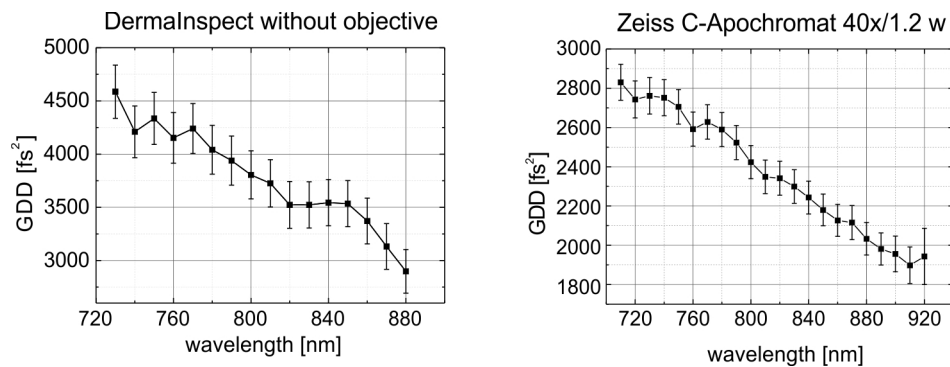


**Figure 4.6:** Measured group delay dispersion of the two-photon microscope (Dermalnspect, JenLab) and the microscope objective (Zeiss C-Apochromat 40x/1.2 w).

For generating excitation- and emission spectra of specific cells and cellular structures, regions of interest (ROIs) were defined in the images. The ROIs were selected manually according to tissue morphology and delineated using the image analysis software ImageJ (<http://rsbweb.nih.gov/ij>). ROIs were the apical cytoplasm of enterocytes (ECs), bright punctuate regions, presumably lysosomes, within the apical cytoplasm of enterocytes, and antigen presenting cells (APCs) that contained many bright granules in the lamina propria of villi and Peyer's patches. For each excitation wavelength, 4-20 ROIs of the same type were evaluated in an image and the average intensity value and standard error of the mean of these ROIs were calculated for each emission channel. A channel-specific mean background value as recorded in a dark measurement without laser irradiation was subtracted from this value. Subsequently, data were corrected for

## 4. EXPERIMENTAL SETUP AND METHODS

---

the experimental parameters according to equation 4.2.

The corrected average fluorescence intensity  $\langle F_{corr} \rangle$  as a function of excitation wavelength was analyzed in order to characterize enterocytes, and antigen presenting cells within the lamina propria of Peyer's patches and villi by their spectral excitation-emission fingerprints.

Emission spectra with four bins corresponding to the four emission channels were calculated at a fixed excitation wavelength for a desired cell type as follows:

$$\langle F(t)_{corr} \rangle_{ch_i}(\lambda_{ex}) = \langle F(t) \rangle_{ch_i}(\lambda_{ex}) \frac{\lambda_{ex}\tau}{\langle P(r,t) \rangle^2} \quad (4.4)$$

Analogous, the specific excitation spectrum of the respective cell type or tissue structure was calculated by integrating the mean fluorescence intensity over all four emission channels  $ch_i$  for each excitation wavelength  $\lambda_{ex}$ :

$$\langle F(t)_{corr} \rangle_{sum}(\lambda_{ex}) = \frac{\lambda_{ex}\tau}{\langle P(r,t) \rangle^2} \sum_{i=1}^4 \langle F(t) \rangle_{ch_i}(\lambda_{ex}) \quad (4.5)$$

Two-dimensional excitation-emission spectra were produced by plotting  $\langle F(t)_{corr} \rangle$  for each emission channel  $ch_i$  as a function of excitation wavelength.

In some cases, information is contained in the set of images that can be visualized by combining single spectral excitation or emission images to a ratiometric image. Therefore, a mathematical operation that links these images is performed pixel-wise on the images, e.g. building a ratio. A prerequisite for useful ratiometric imaging is that the same structures are imaged to the same pixels in the images. That is, structures must not move from one to the other image, or they must be registered before a ratiometric image can be generated.

### 4.4 Laser manipulation

Figure 4.7 shows the experimental setup for combined laser manipulation with online dosimetry and two-photon microscopy of the tissue. Laser manipulation, dosimetry and imaging were done through the same water immersion microscope objective. Lesions were produced by focussing single-longitudinal mode (slm) UV laser pulses with 355 nm wavelength, 500 ps pulse duration and Gaussian beam profile, (PNV 001525, teem

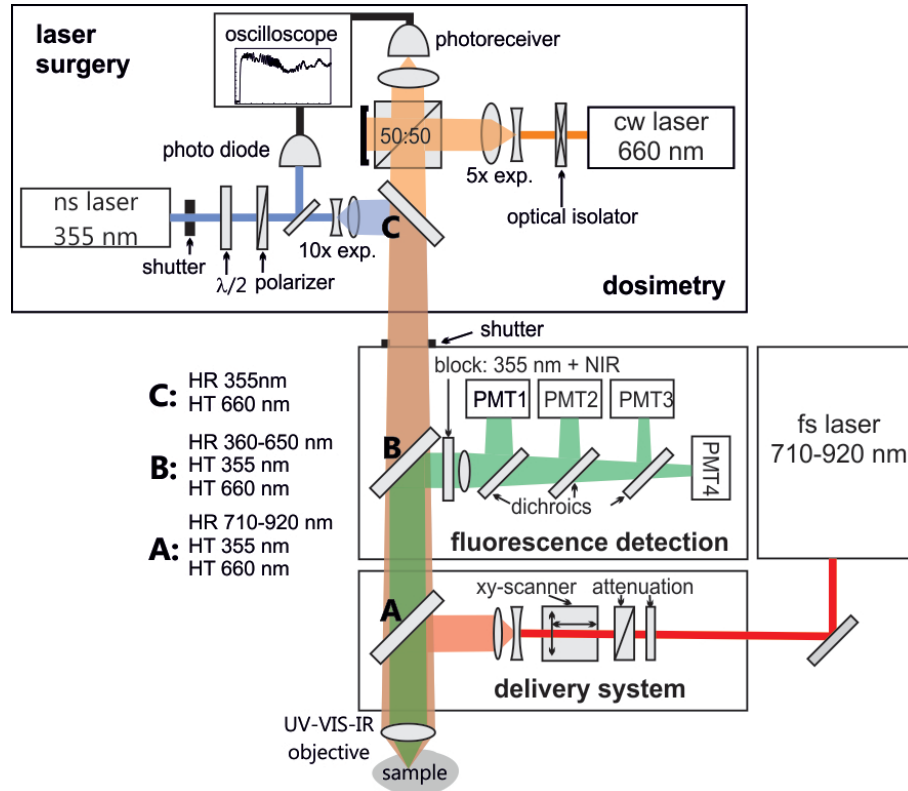


**Figure 4.7:** Setup for UV laser manipulation with online dosimetry and spectrally resolved imaging by two-photon excited fluorescence microscopy. PMT = photomultiplier tube, exp. = beam expander, cw = continuous wave mode, HR = highly reflecting, HT = highly transmitting.

photonics) into the intestinal epithelium. The UV laser beam was coupled into the fluorescence pathway of the two-photon microscope used for imaging, and expanded to fill the back aperture of the microscope objective. The divergence of the UV laser was adjusted such that the focus falls within the imaging plane of the two-photon microscope. Single pulses for laser nanosurgery were selected from the 10-Hz pulse train using a mechanical shutter. The maximum pulse energy of the UV laser system is  $30 \mu\text{J}$  and could be attenuated by means of a half-wave plate and polarizer. A fraction of the attenuated beam was deflected by a beam splitter and directed onto a photodiode. The diode's signal was used as energy reference and to trigger the oscilloscope. Before each experiment, the UV pulse energy entering the back entrance pupil of the objective was measured using a photodiode-based energy meter (PD 10, Ophir Optonics Ltd). Data

## 4. EXPERIMENTAL SETUP AND METHODS

---

were then corrected for the objective’s transmittance as provided by the manufacturer (0.43 at 355 nm). For laser surgery it was aimed at a plane 4  $\mu\text{m}$  below the surface. Aiming in axial direction relied on two-photon imaging of the apical cytoplasm of the epithelial cells. In the lateral direction a cross-hair was used that indicated the fixed focus position of the UV laser beam. The sample was moved until the cross-hair pointed to the desired location in the simultaneously recorded two-photon microscopic images.

Online-dosimetry of the size of the laser-induced microbubbles was done by a probe-beam scattering technique similar to that used in previous work [Vogel et al. 2008]. A 40 mW slm diode-pumped solid state laser (RCL-040-660-S, CrystaLaser) at 660 nm wavelength in continuous wave mode (cw) was coupled into the fluorescence pathway of the two-photon microscope and adjusted collinearly and confocally with the UV laser beam. The presence of a cavitation bubble in the laser focus leads to scattering and partial reflection of the cw probe light at the bubble front and back wall. The reflected probe light is detected in a backscattering geometry. Therefore, an interferometric setup was built with a 50:50 beamsplitter and a fast photoreceiver with 200 MHz bandwidth corresponding to  $< 5$  ns temporal resolution (HCA-S-200M-SI, FEMTO Messtechnik GmbH). Bubble initiation and collapse are marked by the onset and final minimum of the scattering signal. The time difference between initiation and collapse defines the bubble oscillation time  $T_{osc}$ , which scales with bubble size  $R_{max}$  as is described in Sect. 3.3.2. Further, during the bubble’s oscillation, light reflected from the bubble’s front and back wall interferes and gives rise to amplitude modulations of the scattering signal. Each complete fringe (minimum and maximum) corresponds to a diameter change of  $\lambda/2$  and a radius change of  $\lambda/4$ . Thus, starting from  $R_{max}$  that is determined from  $T_{osc}$ , the interference fringes allow to track the movement of the bubble wall with nanometer accuracy [Linz et al. 2013]. Details are described in section 3.3.

### 4.5 Staining protocols

#### LysoTrackerR Red DND-99

LysoTrackerR Red DND-99 (Invitrogen) was used in order to identify intracellular lysosomes. 50  $\mu\text{l}$  of 1 mM LysoTrackerR were diluted with 500  $\mu\text{l}$  standard NaCl solution

and were applied in situ onto the intact intestinal mucosa. The dye is membrane permeant and coupled to a weak alkali. Therefore it accumulates in acidic cell compartments such as lysosomes. LysoTrackerR Red DND-99 has an emission maximum of 600 nm and is detected by PMT 4 (Fig. 4.3).

### **Propidium iodide**

Propidium iodide (PI) was used in order to identify damaged cells. A drop of PI solution (1 mg/ml in NaCl) was applied in situ and flushed with Ringer solution after 1-10 min. Because PI is membrane impermeant to healthy cells, it enters exclusively defect cells and intercalates with double-stranded DNA or RNA. When bound to nucleic acids, the fluorescence emission maximum is 617 nm which is detected by PMT 4 (Fig. 4.3).

### **Blood smears**

Blood smears were stained according to the Pappenheim staining method with modified May-Gruenwald's solution (Merck) and Giemsa stain solution (Merck). Polymorphonuclear leucocytes, mainly neutrophil granulocytes, could be identified by standard microscopic morphology.

#### 4. EXPERIMENTAL SETUP AND METHODS

---

## 5

# Spectrally resolved two-photon microscopy of murine small intestine in vivo

In this chapter, it is shown that spectrally resolved two-photon excited autofluorescence imaging can be used to distinguish different cell types and functional areas during dynamic processes in the living gut. First, images of the physiological situation and function of small intestinal mucosa are presented. These data indicate that normal tissue function is sustained during the experimental situation and serve as a reference compared to the situation after experimental manipulation with the UV ns laserpulses (Chap. 6). Then, excitation and emission spectra of mucosal tissue and tissue components are presented and correlated to spectra of endogenous chromophores. It is shown that selective excitation with only two different wavelengths within the tuning range of a Ti:sapphire femtosecond laser system yields excellent discrimination between enterocytes, antigen presenting cells and lysosomes based on the excitation and emission properties of their autofluorescence. Changes of the spectral signature with the onset of photodamage are demonstrated and their origin is discussed.

Major parts of this chapter have been published in the peer-reviewed Journal of Biomedical Optics [Orzekowsky-Schroeder et al. 2011]. This text closely follows the argumentation in that paper.

## 5. SPECTRALLY RESOLVED 2PM OF MURINE SMALL INTESTINE

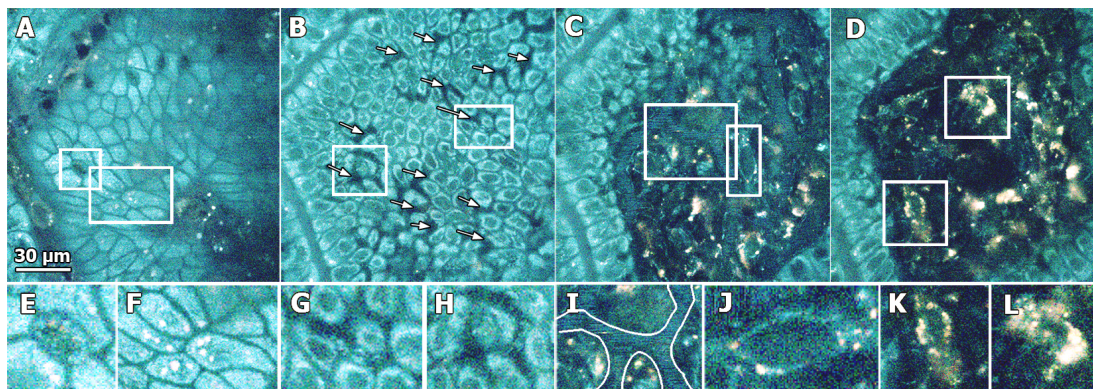


**Figure 5.1: Movie 5.1.** Image stack through  $33 \mu\text{m}$  of an intestinal villus. Excitation wavelength  $\lambda_{ex}=730 \text{ nm}$ , image size  $150 \times 150 \mu\text{m}^2$ . (A)  $1.6 \mu\text{m}$  depth. Goblet cells appear dark in the bright mosaic pattern of enterocytes. (B)  $13.6 \mu\text{m}$  depth. Black intraepithelial lymphocytes reside between the basal part of the prismatic epithelial cells. Cell nuclei appear dark. (C,D)  $22.4$  and  $25 \mu\text{m}$  depth. Antigen presenting cells filled with bright granules, fibroblasts and blood vessels are visible in the lamina propria. Details of the image stack: goblet cell (E), epithelial lysosomes (F), intraepithelial lymphocytes (G,H), capillary vessel (I), fibroblast (J), antigen presenting cells (K,L). (Color-map-1).

### 5.1 Physiological appearance of small intestine based on intrinsic contrast

With the setup described in Chap. 4, image stacks of optical sections were recorded at different depths, and thus the three-dimensional morphology of small intestinal mucosa in vivo was imaged [Klinger et al. 2012]. Figure 5.1 and Movie 5.1 show an image stack of a volume  $150 \times 150 \mu\text{m}^2$  covering  $33 \mu\text{m}$  depth starting in the lumen just above the tip of an intestinal villus. At  $1.6 \mu\text{m}$  depth, the **epithelium** appears as a mosaic of bright areas with dark borders (Fig. 5.1 A). In contrast to the bright cytosol of **enterocytes** the outline of the cells appears dark. Dark pieces in the mosaic were identified as mucus-containing **goblet cells**. The mucus itself does not fluoresce, but cytosol and mitochondria below the mucus granules do show fluorescence (Fig. 5.1 E). In some enterocytes bright granules appear in the apical cytoplasm (Fig. 5.1 F). These granules are most likely **lysosomes** that are known to be located predominantly in the apical cytoplasm of enterocytes. **Cell nuclei** of enterocytes start to appear at approximately  $4 \mu\text{m}$  depth and extend up to  $16 \mu\text{m}$  depth (Fig. 5.1 B). The nuclei appear dark in the autofluorescence image, because the densely packed chromatin is not fluorescent,

and they contain only low concentrations of fluorescent NADH [Zhang et al. 2002]. At about 14  $\mu\text{m}$  depth, dark cells are found between the enterocytes (Figs. 5.1 B, G, H). These are **intraepithelial lymphocytes (IELs)** in which the non-fluorescent cell nucleus makes up most of the cell volume. The Movies 5.3 and 5.4 belonging to Figs. 5.3 and 5.4 will show that IELs are vigorously moving between the enterocytes. It is known that IELs consist of  $\approx 50 - 60\%$   $\gamma\delta$  T cells. These are specialized lymphocytes that ensure the homeostasis of the intestinal epithelium [Chen et al. 2002] and protect against intestinal inflammation [Inagaki-Ohara et al. 2004, Tsuchiya et al. 2003]. These lymphocytes reside only in the basal part of the epithelium right above the basement membrane.

The **basement membrane** is an important structure that is found in all epithelia. The basal surface of the epithelial cells rests on this collagenous membrane forming cell-matrix connections. As long as cells are attached to the basement membrane, extracellular matrix molecules provide a constant survival signal to epithelial cells [Hofmann et al. 2007]. Because the basement membrane consist mainly of type IV collagen [Le Bleu et al. 2007], which is not autofluorescent and does not yield a second-harmonic generation signal [Strupler et al. 2007], it is not visible in two-photon microscopic images. The basement membrane is located at approximately 17.5  $\mu\text{m}$  in this image stack.

Below, **capillaries, fibroblasts, lymphocytes** and **antigen presenting cells** can be seen in the **lamina propria (LP)** of the villus (Figs. 5.1 I-L respectively): Erythrocytes in the **capillaries** emit a weak autofluorescence signal and, since they are moving fast during image acquisition, appear as faint lines parallel to the scanning direction of the laser beam in the fluorescence image (Movie 5.1). Observation of these movement traces during the experiments served as additional and instantaneous indication that physiological conditions were maintained, because movement traces are not visible when blood circulation of the tissue is compromised. **Fibroblasts** are stationary cells of the connective tissue that play an important role in synthesis of extracellular matrix' constituents (mainly collagen). **Lamina propria lymphocytes (LPLs)** are moving cells and can morphologically not be distinguished from IELs. However, it is known that they comprise a different lymphocyte subset, namely mostly CD4+, TCR- $\alpha\beta$ + cells [Resendiz-Albor et al. 2004]. Using the experimental setup of this work, an average speed of 12  $\mu\text{m}/\text{min}$ . of single LPLs was determined by Klinger et al. [2012].

## 5. SPECTRALLY RESOLVED 2PM OF MURINE SMALL INTESTINE

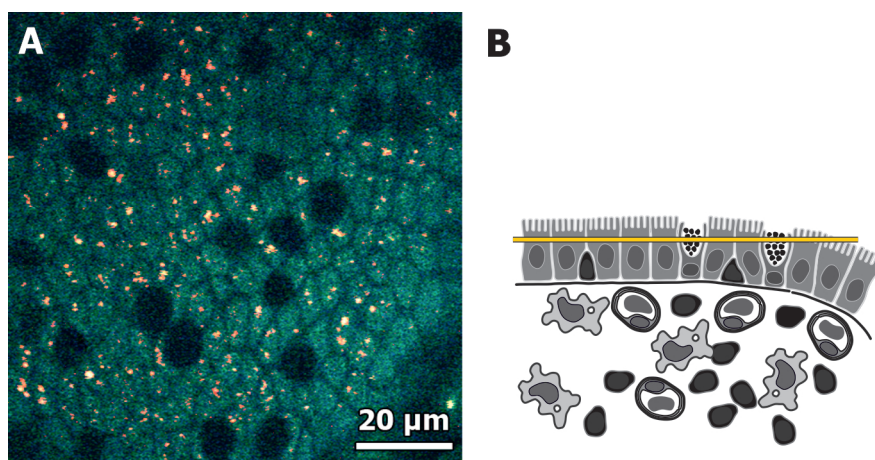


**Figure 5.2:** Sectional view through villus epithelium onto which LysoTracker Red (Invitrogen) was applied one hour before imaging. The image plane lies in the apical cytoplasm of enterocytes. LysoTracker Red stained the bright punctate regions in the apical cytoplasm of enterocytes and confirmed their identification as lysosomes. Excitation wavelength was 780 nm. (Color-map-2)

**Antigen presenting cells (APCs)**, such as **dendritic cells** or **macrophages**, contain many lysosomes that appear as bright reddish or white granules in the false-color images (Figs. 5.1 C, D, K, L). From 26  $\mu\text{m}$  depth on, a dark area devoid of cells appears in the middle of the lamina propria (Movie 5.1). This is most likely a lymph vessel.

Several facts suggest, that the bright punctuate organelles that are located within the apical cytoplasm of enterocytes and within antigen presenting cells are most likely lysosomes. First, due to their function, APCs contain many lysosomes. Second, lysosomes are abundant in all cells which have a mainly resorptive function as have enterocytes. Third, from electron micrographic slides it is known that lysosomes in enterocytes are located preferably in the apical cytoplasm. This interpretation has been confirmed in an experiment using LysoTracker Red (Invitrogen) (see Sect. 4.5). The red fluorescent dye is membrane-permeant and coupled to a weak alkali. Therefore it will accumulate in acidic cell compartments such as lysosomes that typically possess a pH of 4.8. The dye stained the bright cell organelles in the apical cytoplasm of enterocytes when applied directly onto the intestinal mucosa as is shown in Fig. 5.2.

It was already mentioned that the intestinal mucosa is a highly dynamic environment. Therefore, without adding the dimension of time, any description of the phys-

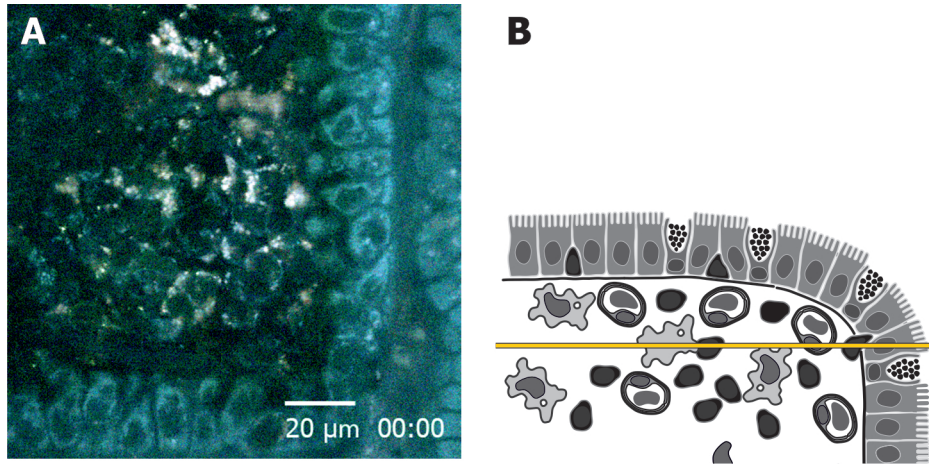


**Figure 5.3: Movie 5.3.** Time-lapse of a cross sectional view of an intestinal villus covering 13 minutes. A frame was recorded every 40 seconds. Excitation wavelength  $\lambda_{ex} = 730$  nm, image size  $150 \times 150 \mu\text{m}^2$ . Cells in the lamina propria as well as intraepithelial lymphocytes move and interact during the observation period. (Color-map-1).

iological state of this tissue would be incomplete. Thus, by imaging the same field of view repeatedly over time, time-lapse videos can be generated that add information about movements, ongoing changes and physiological processes. Figure 5.3 shows a cross section through an intestinal villus that intersects the lamina propria as well as the epithelial layer. In Movie 5.3 this field of view was recorded repeatedly every 40 seconds over a time period of 13 minutes. The time-lapse reveals that cells in the lamina propria of a villus move, interact and change shape. Intraepithelial lymphocytes in the basal part of the epithelium are also constantly in motion. Movie 5.4 (Fig. 5.4) covers the same time span in a different villus and shows exclusively IEL movements. It can be noted that IELs eventually slow down after 13 minutes of observation. The reasons for this finding must be related to the accumulated light dose from scanning laser irradiation in this almost continuous mode of observation. It has been proposed that during scanning irradiation with fs laser-pulses reactive oxygen species are produced [Baumgart et al. 2009, Tirlapur et al. 2001]. These molecules may influence the citrat cycle of metabolism in the cell and eventually lead to apoptosis-like cell death.

In chapter 2 it was already described that the epithelium undergoes physiological turnover every 4-5 days. This process involves the movement of newly generated cells from the proliferative compartment in the lower crypts to the tip of small intestinal

## 5. SPECTRALLY RESOLVED 2PM OF MURINE SMALL INTESTINE

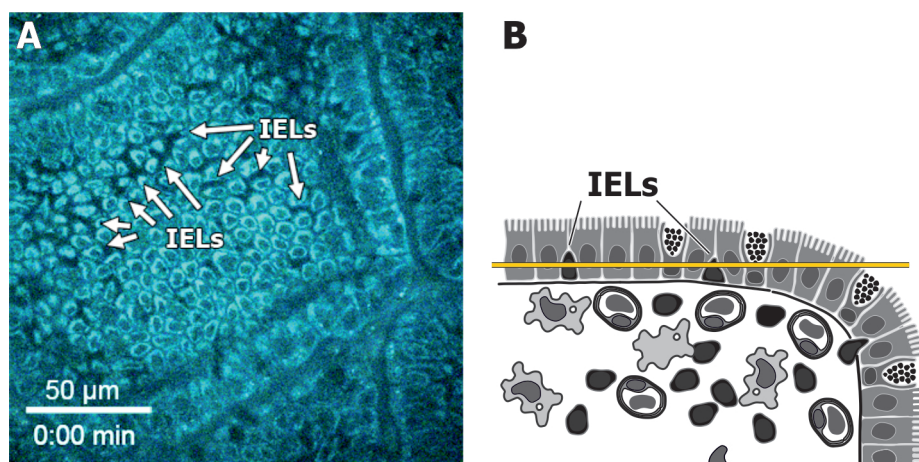


**Figure 5.4:** Still image (A) and time-lapse video (Movie 5.4) of moving intraepithelial lymphocytes (IELs) in the basal epithelium. The movie covers 13 minutes of observation time and the sequence is repeated 3 times. Layout of the tissue and imaging plane (yellow line) are shown in the schematic drawing (B). (Color-map-1).

villi [Karam 1999]. It has been estimated that 1400 cells are shed from each villus tip per day, which is  $\approx 10^{11}$  cells per day from the human small intestine [Potten and Loeffler 1990]. This shedding occurs within minutes and without disruption of epithelial continuity because the surrounding cells constrict the dying cell and meet to form a new multicellular junction below the extruding cell [Madara 1990, Pentecost et al. 2010, Rosenblatt et al. 2001]. Aged epithelial cells, after travelling from the crypt base to the villus tip in the small intestine are thought to die from anoikis, a special form of programmed cell death. In cells that are dependant on anchorage to extracellular matrix structures, such as a basement-membrane, anoikis is induced after detachment from the extracellular matrix [Grossmann et al. 1998, Yuan and Kroemer 2010]. This physiological cell shedding process was repeatedly observed during the experiments and is shown in Fig. 5.5 and Movie 5.5.

Cell shedding and mucus production by goblet cells leads to a continuous production of material which is present in the intestinal lumen, although at the beginning of the experiment the mucosa is rinsed with Ringer solution to remove all luminal contents. Material transport between intestinal villi was also observed in vivo and is shown in Movie 5.6 (Fig. 5.6). The fact that all these processes continue to take place indicates that normal tissue function is maintained under experimental conditions.

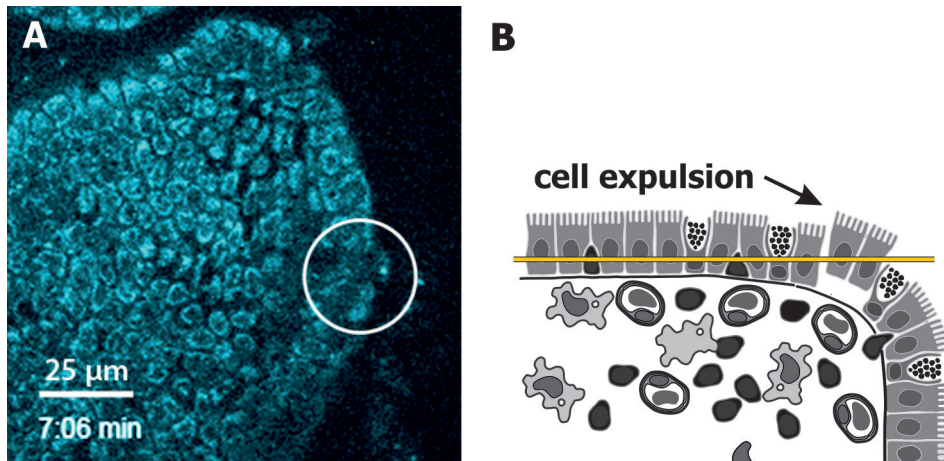


**Figure 5.5:** Still image (A) and time-lapse video (Movie 5.5) of a physiological cell shedding process in murine small intestinal epithelium. The movie covers 11:50 minutes of observation time and the sequence is repeated 4 times. Layout of the tissue and imaging plane (yellow line) are shown in the schematic drawing (B). (Color-map-1).

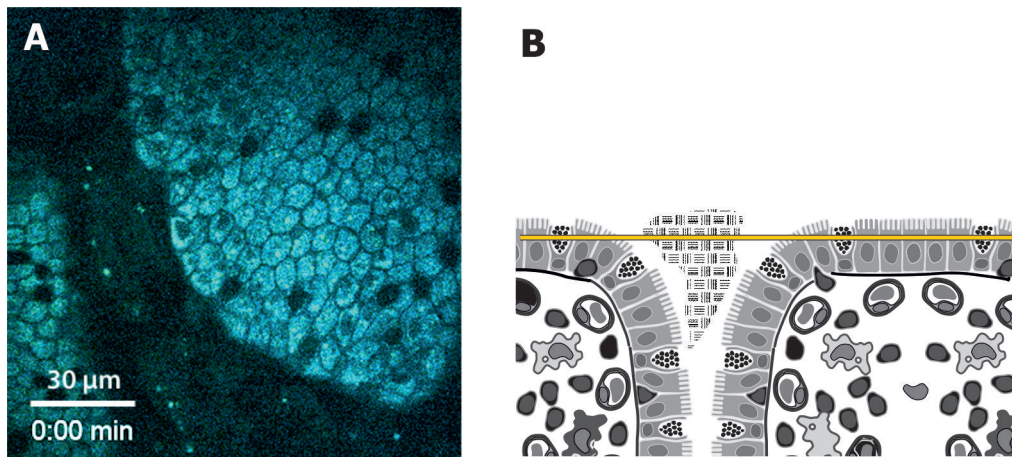


**Figure 5.6:** Still image (A) and time-lapse video (Movie 5.6) of material transport between two intestinal villi. The time-lapse covers 2 minutes of observation time and the sequence is repeated 5 times in the movie. Layout of the tissue and imaging plane (yellow line) are shown in the schematic drawing (B). (Color-map-1).

### 5.2 Autofluorescence spectra of cells and cell organelles in different functional areas within the small intestine

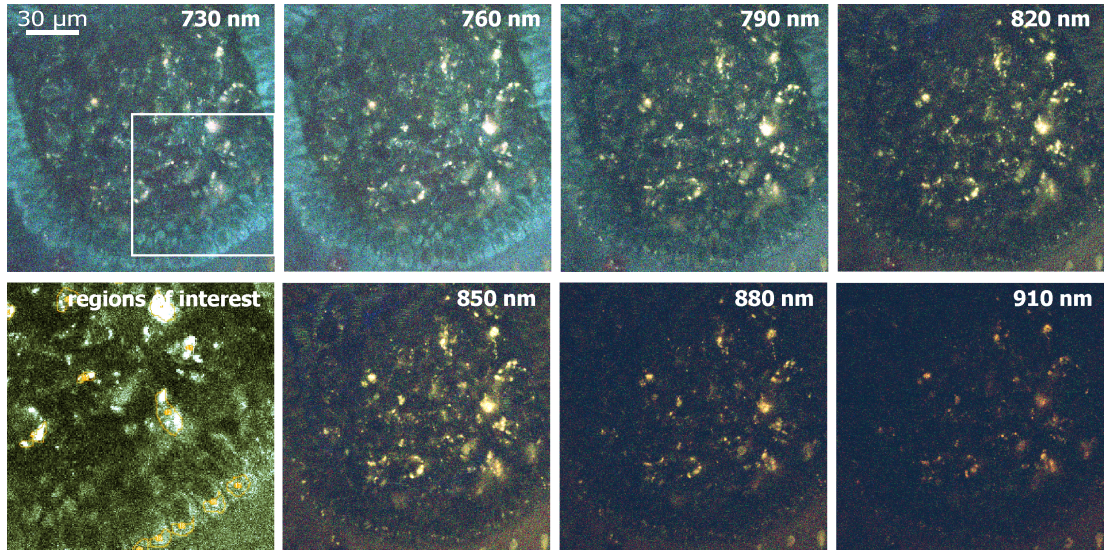
Distinct cellular structures and cell populations can be associated with the two main functions of the small intestinal mucosa, i.e. resorption and immune system. To identify the relevant cells we were interested in the autofluorescence spectra of following tissue components: enterocytes and lysosomes within enterocytes as representatives for resorption, and antigen presenting cells in two different functional areas, the villi and Peyer's patches, as representatives for pathogen sampling and uptake. Antigen presenting cells in the lamina propria of villi and the gut associated organized lymphoid tissue, the Peyer's patches, have different functions and consist of different cell populations (see Chap. 2). Gastrointestinal macrophages are present mostly in the subepithelial lamina propria of villus in the small intestine [Hume et al. 1984] and are believed to be crucial for tissue homeostasis. It has been proposed that antigens resulting from digestion in the lumen and transepithelially transported or degraded intracellularly in enterocyte lysosomes could associate with MHC II complexes<sup>1</sup> and be presented to lymphocytes to suppress the systemic immune response to luminal antigens such as digested food products [Denning et al. 2007, Mayer et al. 1992, Smythies et al. 2005]. In the subepithelial dome area of organized mucosal lymphoid tissue, the Peyer's patches, the dominant antigen presenting cells are dendritic cells [Kelsall and Strober 1996], which are designed to process antigens and initiate specific immune response. In the follicle-associated epithelium, specialized epithelial M cells deliver samples of foreign material through active transepithelial vesicular transport from the lumen directly to intraepithelial lymphoid cells [Neutra and Murtaugh 1998]. Thus, it is conceivable, that these different cell populations from diverse functional areas might contain different mixtures or concentrations of fluorescent molecules and thus show different spectra.

Figure 5.7 shows a series of false-color two-photon excited autofluorescence images of an intestinal villus taken at different excitation wavelengths ('Lambda Stack'). The cytoplasm of enterocytes fluoresces merely at shorter excitation wavelengths. Above 800 nm, within enterocytes only the fluorescence of the bright granular cell organelles in the apical part of the cells is excited. The spectral emission of antigen presenting

---

<sup>1</sup>Main Histocompatibility Complex II: a group of proteins that are important for immune recognition. MHC II molecules are only found on lymphocytes and antigen-presenting cells.

## 5.2 Autofluorescence spectra of cells and cell organelles



**Figure 5.7:** Autofluorescence images of an intestinal villus taken at different two-photon excitation wavelengths. Enterocyte fluorescence is excited only up to 790 nm, while antigen presenting cells in the lamina propria and epithelial lysosomes yield a strong fluorescence signal over the whole excitation spectrum. In the lower left image of the figure, selected regions of interest are exemplarily marked in a region corresponding to the box in the image at 730 nm. (Color-map-1).

cells and enterocytes shows significant differences for excitation at shorter wavelengths: enterocytes appear blue-greenish with a dark nucleus while antigen presenting cells are filled with reddish bright granules. In contrast, antigen presenting cells in the lamina propria yield a strong signal up to the longest available excitation wavelengths. As the excitation wavelength becomes longer the entire images appear more reddish. This is due to the fact that only fluorophores with lower excitation energies and thus a redder emission spectrum can be excited.

Figure 5.8 shows an equivalent excitation wavelength series for the lamina propria of a Peyer's patch at the same magnification. There are more and finer bright granules within the cells compared to the villus lamina propria. Furthermore for  $\lambda_{ex} \geq 790$  nm blue second harmonic signal is emitted from the collagen cross links of the extracellular matrix. The epithelium lies approximately  $12 \mu\text{m}$  above the focal plane and is not visible in this image series.

From Lambda-stacks as shown above, autofluorescence excitation and emission spectra of selected structures were acquired (see. Sect. 4.3). Figure 5.9 A shows auto-

## 5. SPECTRALLY RESOLVED 2PM OF MURINE SMALL INTESTINE

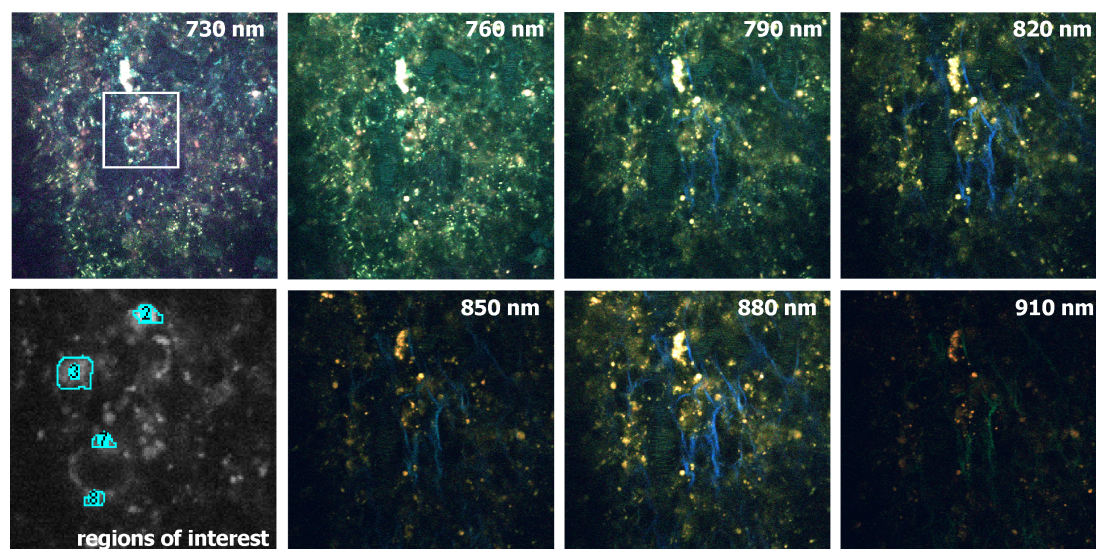


**Figure 5.8:** Autofluorescence images of the lamina propria in a Peyer's patch taken at different two-photon excitation wavelengths. The morphology and inner structure of cells differs markedly from the villus lamina propria (fig. 5.7). At excitation wavelengths  $\geq 790$  nm, second-harmonic light is generated at the collagen framework of the extracellular matrix that is detected in the  $\geq 450$  nm emission channel and thus appears blue in the false-color images. In the lower left image, selected regions of interest are exemplarily marked in a region corresponding to the box in the image at 730 nm. (Color-map-1).

fluorescence excitation spectra for the cytoplasm of enterocytes, antigen presenting cells and lysosomes within enterocytes. Variations in absolute fluorescence intensity were observed for the same cell type between different lambda-stacks recorded in different experiments. These variations were caused by variations in tissue thickness, amount of mucus, remnants of luminal content etc. Therefore, the excitation spectra in Fig. 5.9 were normalized to the intensity value at 730 nm to be able to compare data from different lambda stacks. The fluorescence intensity in all enterocyte excitation spectra decreases by two orders of magnitude with the same slope with increasing wavelength up to about 820 nm. For longer wavelengths, the mean count rate of the autofluorescence signal from enterocytes lies within the standard deviation of the dark count rate.

In contrast, antigen presenting cells in villi and Peyer's patches show a very weak decrease in fluorescence intensity with increasing wavelength. The signal drops at most about one order of magnitude and is well above noise level even for the longest available excitation wavelengths. This corresponds to the good visibility of antigen presenting

## 5.2 Autofluorescence spectra of cells and cell organelles

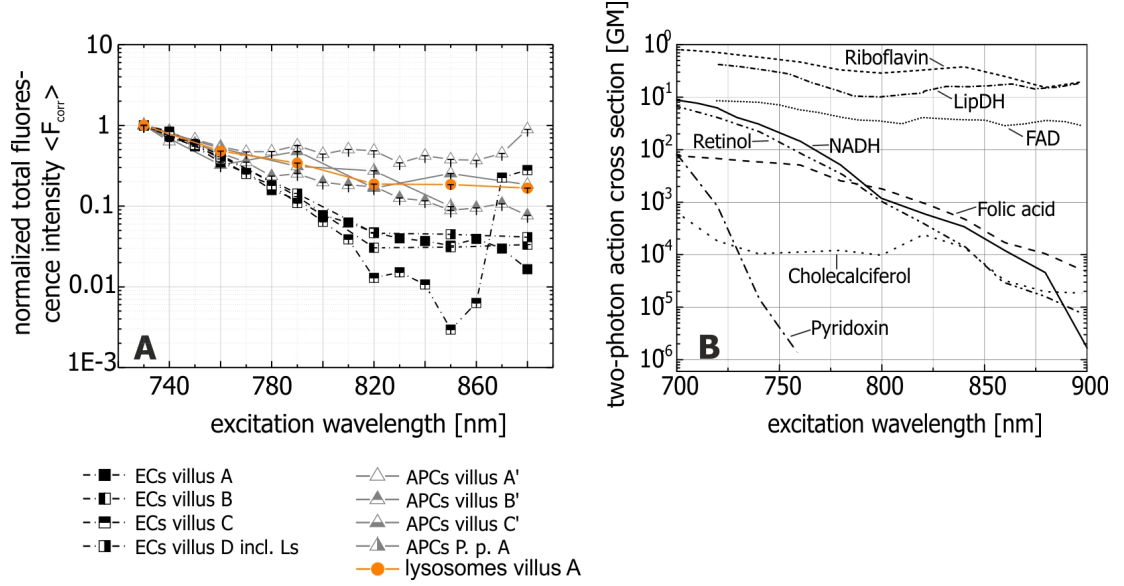


**Figure 5.9:** (A) Measured excitation spectra of intestinal cells and cell organelles. ECs: cytoplasm of enterocytes, APCs: antigen presenting cells, Ls: lysosomes. Capital letters in the legend denote different experiments. For better comparison between different experiments, spectra are normalized to the intensity value at 730 nm and to  $P^2/(\lambda\tau_{\text{pulse}})$ . Here,  $P$  is the average laser power at the sample,  $\lambda$  the excitation wavelength, and  $\tau_{\text{pulse}}$  the pulse length at the sample. After normalization, the recorded intensity values are directly proportional to the two-photon absorption cross sections  $\sigma_{2P}$  of the excited chromophores. (B) Two-photon absorption cross sections for endogenous fluorophores as reported in [Huang et al. 2002, Zipfel et al. 2003].

cells over the whole wavelength range as seen in Fig. 5.7. The variation amongst the signals of antigen presenting cells is stronger than for enterocytes which may be explained by the broad variety of cell shapes and inner structure (granulation). As cells move and change shape, the cell content within the ROIs may slightly vary from frame to frame during wavelength tuning, which may effect the extracted mean intensity values. However, cell parts entering and leaving the image plane should balance on average because a coordinated directed movement of antigen presenting cells is not expected.

Lysosomes in the apical cytoplasm of enterocytes show a similar excitation spectrum to that of antigen presenting cells (orange circles in Fig. 5.9 A), which too contain a large and dense amount of brightly fluorescent cell organelles, presumably lysosomes.

Figure 5.10 shows excitation spectra obtained as above but now broken down into

## 5. SPECTRALLY RESOLVED 2PM OF MURINE SMALL INTESTINE

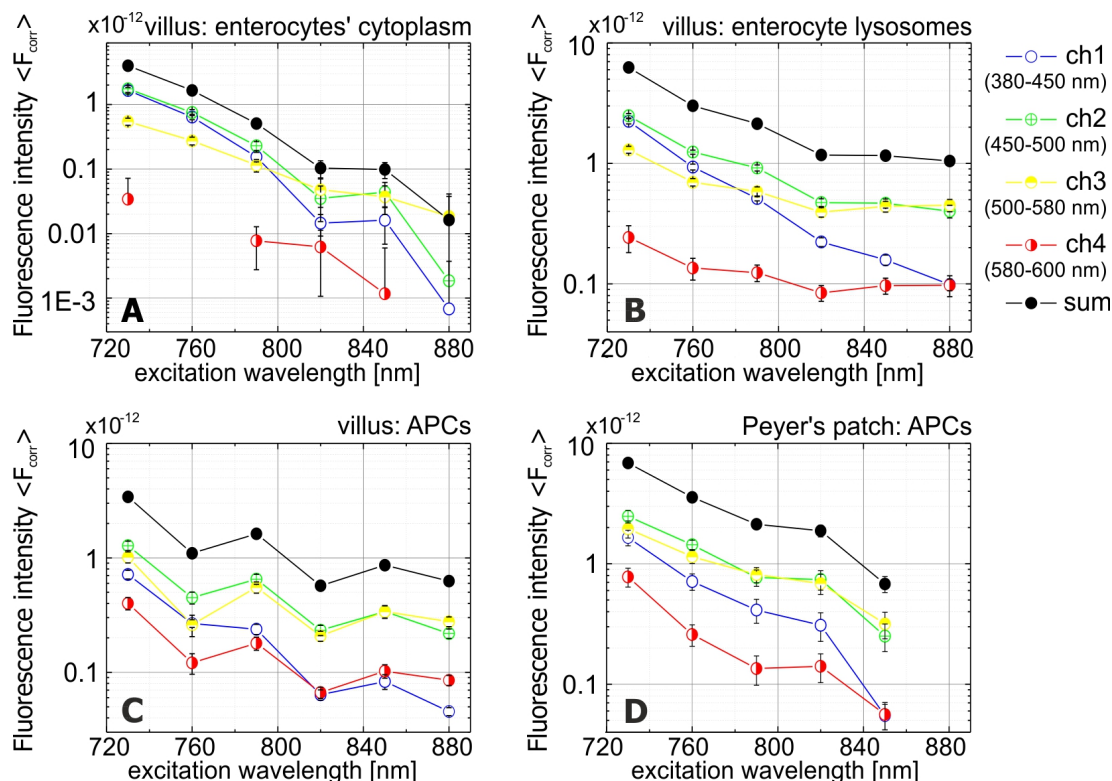


**Figure 5.10:** Spectral excitation-emission characteristics of selected tissue components in the small intestine. **(A)** Apical cytoplasm of villus enterocytes ( $n=7$ ). **(B)** Villus epithelial lysosomes ( $n=15$ ). **(C)** Antigen presenting cells (APCs) in the villus lamina propria ( $n=15$ ). **(D)** Antigen presenting cells in the lamina propria of Peyer's patch ( $n=11$ ). The average intensity from selected regions of interest is plotted on a semilogarithmic scale for each emission channel as function of excitation wavelength (open symbols). In addition, the sum intensity of all channels is shown (black dots). As in figure 8, intensity values are normalized to  $P^2/(\lambda\tau_{pulse})$  in order to correct for measured differences in experimental parameters. All spectra are taken from the same animal in order to compare absolute differences in fluorescence intensity (no normalization to the 730 nm value). Error bars represent the standard error of the mean.

the spectral contributions from each emission channel. All spectra are taken from the same animal and were not normalized to be able to compare absolute intensity differences between different fluorescent structures. The emission spectra exhibit marked differences between the different tissue constituents.

The cytoplasm of enterocytes in an intestinal villus (Fig. 5.10 A) yields a significant signal only in the first three channels, i.e. the fluorescence emission spectrum lies below

## 5.2 Autofluorescence spectra of cells and cell organelles

---

580 nm. The emission  $> 580$  nm in the fourth channel is almost at background level. Therefore, the value is almost zero for 760 and 880 nm excitation and thus out of scale in Fig. 5.10 A. The signals in the first two channels ( $< 500$  nm) are about equal for an excitation wavelength up to 780 nm and brighter than the signal in the third channel (500-580 nm). The decrease of fluorescence intensity with increasing excitation wavelength is more pronounced for channel 1 and 2 than for channel 3. In all channels, excitation with wavelengths longer than 800 nm does not yield significant fluorescence emission from cytosol in enterocytes (see also Fig. 5.7).

The spectral autofluorescence emission of lysosomes in enterocytes of an intestinal villus is shown in figure 5.10 B. Fluorescence intensity is generally brighter, but the main difference as compared to the cytoplasm is a significant signal in the red emission channel that was negligible for the cytoplasm. Further, the signal in the second channel (450-500 nm) is stronger than the short-wavelength contribution ( $< 450$  nm) detected in the first channel, and the fluorescence intensity decrease with increasing excitation wavelength is more pronounced for the first than for the second channel.

Antigen presenting cells of the lamina propria of both villi (5.10 C) and Peyer's patches (5.10 D) show a strong emission of about equal intensity for all excitation wavelengths in the green and yellow channel. In contrast to enterocytes' cytoplasm and lysosomes, this signal is stronger than the fluorescence signal in the first channel for all excitation wavelengths. In the first channel, the signal decreases with increasing wavelength as for cytoplasm of enterocytes. Most likely, the cytoplasm of antigen presenting cells has a composition similar to enterocytes' cytoplasm, which results in a component of similar autofluorescence spectrum. In addition, fluorescence emission in the red channel ( $> 580$  nm) is about a factor 10 stronger for antigen presenting cells than for enterocytes at all excitation wavelengths. Compared to lysosomes, the signal in the red channel is stronger for antigen presenting cells at short excitation wavelengths and decreases more rapidly with increasing excitation wavelength. Overall, the absolute intensities are distributed more equally between all four emission channels, i.e. the emission spectrum of antigen presenting cells is broader and shifted to the red as compared to cytoplasm and lysosomes of enterocytes.

The acquisition and comparison of complete excitation-emission spectra is very time consuming and not suited for a real-time discrimination of cells and cell organelles based

## 5. SPECTRALLY RESOLVED 2PM OF MURINE SMALL INTESTINE

### A) Ratio of fluorescence emission intensities at 730 nm excitation wavelength

	ch2/ch1	ch2/ch3	ch2/ch4
villus ECs	$1.06 \pm 0.18$	$3.20 \pm 0.56$	$51.1 \pm 57$
villus lysosomes	$1.11 \pm 0.07$	$1.91 \pm 0.15$	$10.2 \pm 2.6$
villus APCs	$1.79 \pm 0.23$	$1.26 \pm 0.18$	$3.19 \pm 0.49$
Peyer's patch APCs	$1.50 \pm 0.29$	$1.27 \pm 0.26$	$3.18 \pm 0.69$

### B) Ratio of fluorescence emission intensities at 820 nm excitation wavelength

	ch1/ch2	ch1/ch3	ch1/ch4
villus ECs	$2.42 \pm 1.6$	$0.73 \pm 0.54$	$5.65 \pm 5.7$
villus lysosomes	$2.12 \pm 0.24$	$1.20 \pm 0.14$	$5.61 \pm 0.94$
villus APCs	$3.67 \pm 0.53$	$1.12 \pm 0.16$	$3.5 \pm 0.53$
Peyer's patch APCs	$2.39 \pm 0.78$	$1.08 \pm 0.29$	$5.25 \pm 1.71$

### C) Ratio of fluorescence emission intensities at 730 nm and 820 nm excitation wavelength

	$\frac{ch1(730nm)}{ch1(820nm)}$	$\frac{ch2(730nm)}{ch2(820nm)}$	$\frac{ch3(730nm)}{ch3(820nm)}$	$\frac{ch4(730nm)}{ch4(820nm)}$
villus ECs	$114 \pm 44$	$50 \pm 29$	$11 \pm 6$	$5.5 \pm 7.6$
villus lysos.	$10 \pm 1.0$	$5.3 \pm 0.5$	$3.3 \pm 0.4$	$2.9 \pm 0.8$
villus APCs	$11 \pm 1.5$	$5.5 \pm 0.8$	$4.9 \pm 0.7$	$6.0 \pm 1.0$
Peyer's p. APCs	$5.4 \pm 1.6$	$3.4 \pm 0.7$	$2.8 \pm 0.7$	$5.5 \pm 1.8$

**Table 5.1:** Ratiometric comparison of autofluorescence emission for cytoplasm of enterocytes (ECs), lysosomes and antigen presenting cells (APCs) in an intestinal villus and antigen presenting cells in a Peyer's patch. Ratios of the normalized intensity values in the four spectral emission channels (ch 1 - ch 4) were calculated for the data of fig. 5.10.

on their autofluorescence spectra. However, ratiometric comparison of autofluorescence emission in the four emission channels or at two fixed excitation wavelengths could be used instead. Therefore, in figure 5.11 and table 5.1 the spectral fluorescence emission of the different cells and cell organelles of fig.5.10 is compared at 730 and 820 nm excitation.

In table 5.1 channel 2 was chosen as ratiometric reference channel following an approach taken by Huang et al. [2002]. These authors showed that, using 750 nm and 800 nm two-photon excitation and fluorescence emission channels of 410-490 nm and 510-650 nm, ratiometric imaging of NAD(P)H and flavoprotein in cardiomyocytes reflected the redox-state of the cell. They found that fluorescence excitation at 800 nm compensated for the large differences in concentration and two-photon absorption cross section of NAD(P)H and flavin adenine dinucleotide (FAD) at the mitochondria and

## 5.2 Autofluorescence spectra of cells and cell organelles

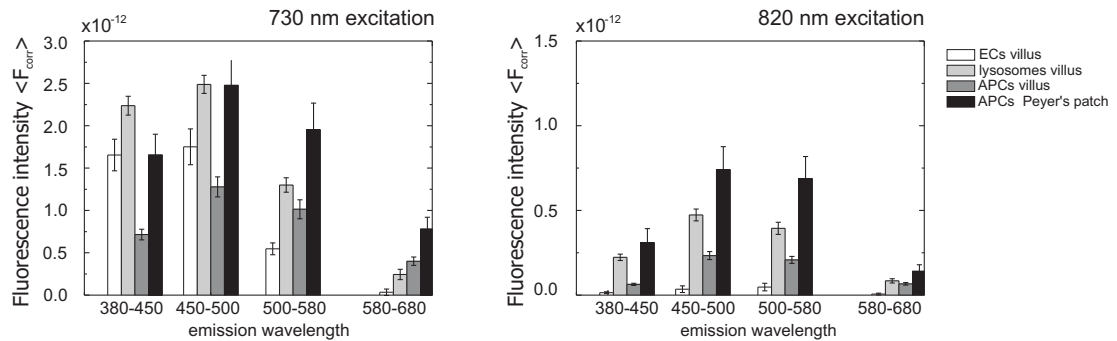


**Figure 5.11:** Emission spectra of epithelial cells (ECs), lysosomes and antigen presenting cells (APCs) at 730 nm excitation and 820 nm excitation.

gave an almost balanced picture of the redox-ratio. In our setup, NAD(P)H fluorescence is detected mainly in channel 2 (450-500 nm), while flavins fluoresce predominantly in channel 3 (500-580 nm). Consequently, the ratio of fluorescence intensities ch2/ch3 excited at 820 nm should best reflect the NAD(P)H/FAD ratio. At 730 nm excitation, all four selected tissue components are visible and all of them peak at 450-500 nm emission. However, for the cytoplasm and lysosomes within enterocytes, the short-wavelength contribution from 380-450 nm is about as strong as the emission between 450-500 nm. This is reflected in a ratio close to one for ch2/ch1 in table 5.1 A). The red-shifted spectral emission of lysosomes as compared to the cytosol is represented by a lower ch2/ch3 ratio of lysosomes. The high ch2/ch4 ratio for cytoplasm of enterocytes has a large error and has to be disregarded due to the marginal fluorescence intensity in channel 4. The ch2/ch3 ratios at 730 nm and 820 nm excitation show differences between enterocytes, lysosomes and antigen presenting cells. At 820 nm this ratio is approximately the same for lysosomes and antigen presenting cells but lower for enterocytes. This difference must not necessarily be related to differences in the redox-state of the cell populations but may originate from our ROI selection. While in enterocytes we selected regions in the apical cytoplasm containing a high amount of mitochondria, the ROIs in antigen presenting cells comprise only a minor fraction of mitochondria and cytosol but a large amount of the bright granules which we identified as lysosomes. Thus, although the ratio of emission intensities in ch2/ch3 discriminates between enterocytes and antigen presenting cells, it does not necessarily tell about differences in the respective metabolic states. The ROIs selected for antigen presenting cells in villi and Peyer's patches contain similar structures. Nevertheless, even though

## 5. SPECTRALLY RESOLVED 2PM OF MURINE SMALL INTESTINE

---

the cell populations and their tasks differ, the ch2/ch3 ratio does not show differences between these cell types within the error margins. If differences in the NAD(P)H/FAD ratio are present, they may not be observable because of the high lysosomal portion in the cells compared to the mitochondrial portion. The ch2/ch1 ratio is slightly larger for antigen presenting cells in the lamina propria of villi than for antigen presenting cells in the Peyer's patches. This indicates that antigen presenting cells in villi contain fluorophores that emit in the short-wavelength range of ch1 in lower concentration or with lower two-photon absorption cross section than those in Peyer's patches. Table 5.1 C indicates that antigen presenting cells in Peyer's patches and villi can be even better distinguished when looking not only at a single excitation wavelength at 730 nm or 820 nm. The short-wavelength emission intensity at 730 nm compared to 820 nm excitation is twice as bright for macrophages in the lamina propria of the villi than for dendritic cells in the subepithelial dome area of Peyer's patches (ch1(730 nm)/ch1(820 nm)). Likewise, the higher ratios of ch3(730nm)/ch3(820nm) and ch4(730nm)/ch4(820nm) for antigen presenting cells in a villus points to a red-shifted emission spectrum at 730 nm excitation as compared to lysosomes. This points to an additional autofluorescence component with larger Stokes shift in antigen presenting cells.

### 5.3 Correlation of spectral cell signatures to endogenous fluorochromes

In order to identify the fluorochromes contributing to the autofluorescence signal, the spatial distribution of the fluorescence and the recorded excitation-emission spectra are compared with the known morphology of the cells and literature data of endogenous fluorescent chromophores contained in the studied tissue components (Figs. 4.3 and 5.9 B). The comparison indicates that autofluorescence in enterocytes arises mainly from NAD(P)H, which is abundant in high concentrations at the mitochondria and in lower concentrations in the cytosol. The regions of interest in the apical part of enterocytes comprise the cytosol and everything that is located within this selected part of the cell, for example mitochondria. In the normalized excitation spectra of the tissue components, the wavelength dependence of the two-photon action cross sections of the fluorescent chromophores is reflected in the slope of the spectra. The steep decrease of spectral amplitude with increasing wavelength observed for cytosol of enterocytes

### 5.3 Correlation of spectral cell signatures to endogenous fluorochromes

---

corresponds well with the literature data for NADH (solid line in fig. 5.9 B). The value for the action cross section of NADH drops by one and a half orders of magnitude between 730 and 800 nm, and so does the normalized fluorescence intensity value that was measured for the apical cytoplasm of enterocytes. Figure 4.3 shows that the spectral emission of NAD(P)H is maximal around 470 nm and thus predominantly is detected in channels 2 and 1 with a small contribution in channel 3. This corresponds well to the spectral emission pattern measured for the cytoplasm of enterocytes. Though riboflavin or retinol have similar spectral characteristics their low concentration in these cells and the distribution pattern of the fluorescence, which matches the distribution of the mitochondria, lead to the conclusion that NADH contributes mostly the the fluorescence of the enterocytes.

In lysosomes of enterocytes and in antigen presenting cells that contain lysosomes, the fluorescence signal seems to have a high contribution from flavins and lipopigments. Lysosomal membranes contain FAD [Shin and Mego 1988] that emits around 550 nm (flavins, Fig. 4.3) and that can be efficiently excited over the whole tuning range of the laser (Fig. 5.9 B). The good visibility of the lysosomal signal over all excitation wavelengths (Figs. 5.7 and 5.9 A) and the generally much higher fluorescence intensity of lysosomes and antigen presenting cells compared to other tissue structures corresponds well with the high two-photon action cross section of FAD (Fig. 5.9 B). Another possible fluorescence source within lysosomes are lipo-pigments that accumulate within lysosomes as a result of degradation of lipids. The emission spectrum of lipo-pigments is very broad, with a maximum around 550 nm (fig.4.3). The lipo-pigment lipofuscin is found in granules of 1-5  $\mu\text{m}$  size within the cytoplasm of metabolically active cells such as the retinal pigment epithelium [Richards-Kortum and Sevick-Muraca 1996] and has been described also in villus macrophages [Bronson 1981]. Lipofuscin has a high two-photon action cross section [Zipfel et al. 2003] and its excitation maximum covers the broad range from 700-850 nm, which corresponds well to the excitation spectra of lysosomes measured in the present study (Figs. 5.10 and 5.11). The strong contribution of fluorescence emission from lysosomes in channel 3, where the FAD and lipo-pigment signal are measured, further corroborates the link of lysosomal autofluorescence to these chromophores. In addition, the bright punctuate regions in the apical cytoplasm of enterocytes in fixed sections of rat intestinal villi have been associated

## 5. SPECTRALLY RESOLVED 2PM OF MURINE SMALL INTESTINE

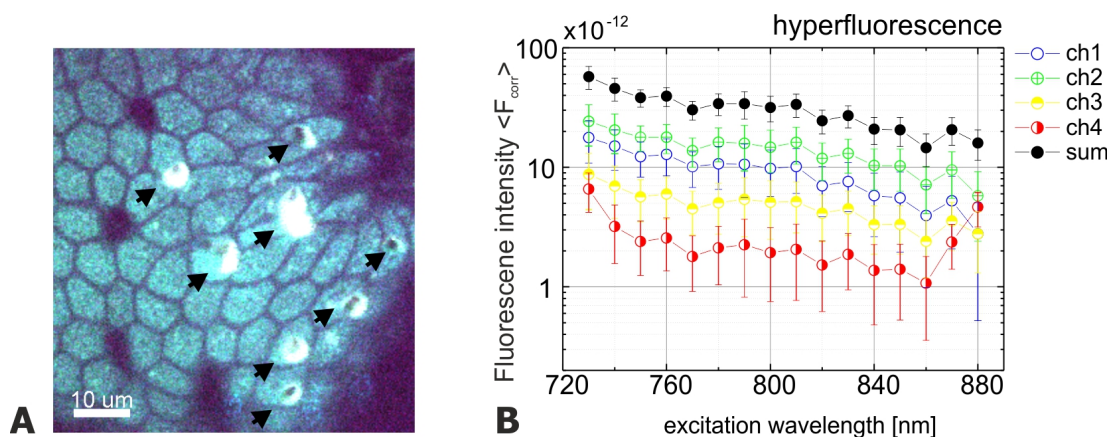


**Figure 5.12:** Hyperfluorescence induced by repeated scanning irradiation. **Movie 5.12.** Intestinal villus tip scanned 7 times with an average excitation power of 37.9 mW and excitation wavelength 730 nm. This is about 1.5 times more average power than what was usually used for autofluorescence imaging. Scan time per frame and field of view were 7.4 s and  $150 \times 150 \mu\text{m}^2$ . After five scans, hyperfluorescent lesions start to occur at several sites. Additionally, an active retraction of the villus is observed. **(A)** Enlarged section of the field of view from Movie 5.12, after 7 scans. Hyperfluorescent regions are marked by arrowheads. **(B)** Excitation-emission spectrum of hyperfluorescent regions. The intensity increase in channel 4 at 730 and 870-880 nm is due to excitation stray light. (Color-map-1).

with storage of indoleamines, a group of neurotransmitters, based on three-photon excited UV-emission below 400 nm [Zipfel et al. 2003]. This interpretation cannot be confirmed, because the used setup cannot detect fluorescence below 400 nm. However, it seems likely that lysosomes contain a mixture of the above mentioned chromophores, including indoleamines.

### 5.4 Rapid fluorescence increase and photodamage

Besides identifying tissue constituents, the spectral information allows also to monitor changes of cell state induced by the laser irradiation. When the exposure due to scanning irradiation is too high, after a certain irradiance time suddenly a bright fluorescence, which we named hyperfluorescence, associated with cell damage appears (Fig. 5.12 and ). Movie 5.12 shows that these hyperfluorescent lesions occur subsequently at several points in the scanned image plane and grow when they are further irradiated. When they have grown, the hyperfluorescent regions in many cases surround a small

## 5.4 Rapid fluorescence increase and photodamage

---

dark area. This may indicate that the hyperfluorescence develops a three-dimensional structure like a sphere or bubble. The total fluorescence intensity in the hyperfluorescent regions increases to a level 10 times and 40 times higher than the lysosome or cytosol fluorescence, respectively. Typically, the increase in fluorescence intensity is first noticed in channel 4, i.e. in the red part of the emission spectrum, where the normal autofluorescence signal is very weak. Additionally in Movie 5.12 it is observed that the whole villus actively retracts from the focus plane. It is likely that photochemically induced concentration changes of molecules such as reactive oxygen species associated with oxidative stress trigger a contraction of smooth muscle cells in the villus lamina propria that leads to the observed villus retraction.

Fig. 5.12 B shows the measured characteristic spectral excitation-emission properties of the hyperfluorescence. The fluorescence excitation spectrum exhibits a weak, monotonous decay with increasing wavelength. The emission spectrum shows, for all excitation wavelengths, a maximum in the green channel (450-500 nm) and is quite strong also in the blue channel (400-450 nm). The signal in the red emission channel (600-680 nm) has the smallest contribution to the hyperfluorescence emission spectrum, but it is much stronger for hyperfluorescent regions than for cells that are not yet photodamaged (see Fig. 5.10). The excitation wavelength dependence of the total hyperfluorescence intensity (sum of all channels) resembles that of antigen presenting cells. However, the spectral emission of hyperfluorescence peaks at shorter wavelengths (ch. 1, 2) while it is maximal in channels 2 and 3 for antigen presenting cells. This difference indicates that the chemical composition of the relevant fluorophores in the hyperfluorescent lesions is different from the autofluorescence components.

Chemical changes of cellular substances may be induced directly by two-photon or three-photon processes [Nikogosyan 1990] but also indirectly via free-electron generation that results in chemical bond breaking [Vogel et al. 2005]. Further, cellular metabolism may be altered in response to the induced ‘photo-stress’ and may actively contribute to the formation of new chemical substances.

In our experiments, hyperfluorescence commenced at roughly 2 times the average excitation power that was normally used for imaging at 730 nm. The fact that hyperfluorescence starts only after a certain irradiance time suggests that the involved photochemical processes are dose-dependent. It is also likely, that cellular repair mech-

## 5. SPECTRALLY RESOLVED 2PM OF MURINE SMALL INTESTINE

---

anisms will counteract the photo-stress and thus influence the threshold for visible damage that appears in the form of hyperfluorescence.

Hyperfluorescence during two-photon excited fluorescence microscopy has been observed previously in cultured cells [Tiede and Nichols 2006] and in collagenous tissue such as tendon and cornea [Hovhannisyan et al. 2008]. Tiede and Nichols [2006] observed formation of point-like or granular hyperfluorescent lesions during two-photon excited fluorescence microscopy in cultured cells very similar to the results presented in this thesis. Because of the granular structure and the emission spectra of the hyperfluorescent lesions that showed a broad peak near 600 nm, they proposed that the bright granules might contain lipofuscin, a group of age-pigments. Lipofuscin is known to accumulate in cells in response to oxidative stress and consists of non-degradable oxidized protein-lipid aggregates [Boulton et al. 2004, Haralampus-Grynaviski et al. 2003, Mata et al. 2000]. Lipofuscin is also found in lysosomes [Brunk and Collins 1981, Essner and Novikoff 1960], and lysosomes are found in many enterocytes as has been described in Sect. 5.1. Because lipofuscin itself is a photoinducible free radical generator [Boulton et al. 1993], it may contribute to the growing size of the hyperfluorescent areas during further irradiation.

However, although the red emission of hyperfluorescence is stronger than for the autofluorescence components, in this work the hyperfluorescence emission peaks in the green and blue part of the spectrum for all excitation wavelengths. Therefore, the production of lipofuscin alone cannot explain the observed results. In their studies of cornea and tendon, Hovhannisyan et al. [2010] explained femtosecond-laser induced hyperfluorescence by photo-induced tyrosine dimerization and developed a rate-equation model for description of the temporal dynamics. Tyrosine is an essential amino acid that is abundant not only in collagen but also in most proteins. Fluorescence measurements of thin collagen films that underwent photomodification by single pulse UV irradiation showed that the photoproduct has an increased fluorescence over the whole spectrum and additional fluorescent components at 409 and 430 nm wavelengths [Wisniewski et al. 2007]. In our setup, such a fluorescence emission would be detected mainly in channel 1 with a smaller contribution in channel 2 due to a certain spectral overlap of the dichroic filters. However, our spectral emission maximum is in channel 2. Therefore it is likely, that in epithelial cells of murine small intestine tyrosine-photoproducts

do contribute to hyperfluorescence but are not the only newly formed molecules responsible for the observed hyperfluorescence. A mixture with lipofuscin pigments is likely. However, further studies with higher spectral resolution of the emission spectra are needed to clarify the exact chemical composition of the hyperfluorescent regions. It further remains unclear whether the hyperfluorescent molecules are formed by pure photochemistry or as a result of cellular metabolism that is altered by photoinduced stress. Future investigations that focus on the time course of spectral fluorescence may answer these questions.

## 5.5 Conclusions

Spectrally resolved time-lapse two-photon imaging of cellular dynamics was demonstrated in murine small intestine in three dimensions and up to eight hours. Imaging based solely on autofluorescence provides good intrinsic contrast between different cell types, cell organelles and other tissue components of the intestine. The autofluorescence intensity spectra of different cell types and cell organelles were investigated, and marked differences between enterocytes, antigen presenting cells and lysosomes were found. As concluded by the excitation spectra autofluorescence of all named tissue components is excited simultaneously at 730 nm excitation wavelength, while an excitation wavelength  $\geq 820$  nm is best-suited to selectively excite antigen presenting cells and lysosomes within enterocytes and to induce second-harmonic generation at the collagen scaffold of the extracellular matrix. The spectral signatures of cell types and cell organelles were related to the spectra of endogenous fluorophores. It was concluded that autofluorescence in the cytoplasm of enterocytes is mainly due to NAD(P)H. The bright punctuate cell organelles in the apical cytoplasm of enterocytes and within antigen presenting cells were identified as lysosomes that contain FAD and lipopigments.

Strong and long-lasting irradiation of the mucosal tissue induced hyperfluorescence associated with cell damage. The hyperfluorescence excitation-emission spectrum indicates that it arises from a chemical substance with either high concentration or high two-photon absorption cross section that was absent before laser irradiation. The sudden onset of hyperfluorescence indicates that the chemical composition of the tissue is modified locally in a nonlinear process when both a certain irradiation dose and a certain irradiance threshold are exceeded. In our experiments, this occurred when the

## **5. SPECTRALLY RESOLVED 2PM OF MURINE SMALL INTESTINE**

---

power exceeded a value roughly 2 times higher than the average excitation power that was normally used for autofluorescence imaging at 730 nm.

In future, automated segmentation based on autofluorescence fingerprints may be implemented to follow individual cells over long time periods. This feature would facilitate investigations of cell-cell interaction occurring during immunologic processes at this important mucosal interface. In order to selectively follow antigen presenting cells, the use of two different laser wavelengths, for example 730 nm and 820 nm, is best suited to discriminate antigen presenting cells and surrounding tissue. However, since the cells are rapidly moving and acquisition of one image takes about 10 seconds, a sequential imaging with two different excitation wavelengths is not fast enough to capture the same tissue state. Thus, a meaningful ratiometric image showing clearly different tissue structures could not be generated. Therefore, interlaced excitation with two different wavelengths is desirable in order to be able to superimpose the images. With such a setup, a ratiometric comparison of fluorescence intensities in the different emission channels could be used for an online discrimination of different cells or cell organelles. Moreover, in order to tackle immunologic questions, further discrimination of cellular subtypes of antigen presenting cells, such as dendritic cells, B- and T-lymphocytes is needed that may require the combination of exogenous markers with the autofluorescence-based spectral fingerprinting explored in this study.

## 6

# Intravital UV-laser microsurgery of murine gut mucosa with online monitoring of cavitation bubble dynamics

This chapter is dedicated to the study of immune response and healing processes of murine small intestinal mucosa that were investigated by studying the response to localized laser-induced damage. Epithelial lesions were created by 355-nm, 500-ps pulses from a microchip laser that produced minute cavitation bubbles. Size and dynamics of these bubbles were monitored using an interferometric backscattering technique with 80 nm resolution.

In this chapter first the dynamics and size of the laser-induced microbubbles as derived from the scattering signals are presented. It is shown that, as a function of laser pulse energy, bubbles can be generated with maximum radii in two distinct size regimes. Afterwards the immediate destructive effects of microbubbles of different size will be presented, and finally, the healing and immune response of the intestinal mucosa in reaction to the different extents of damage in the two bubble size regimes will be presented. The physiological situation in healthy murine small intestine as observed by two-photon microscopy was introduced in section 5.1 and serves as a reference for the tissue response to small laser-induced lesions.

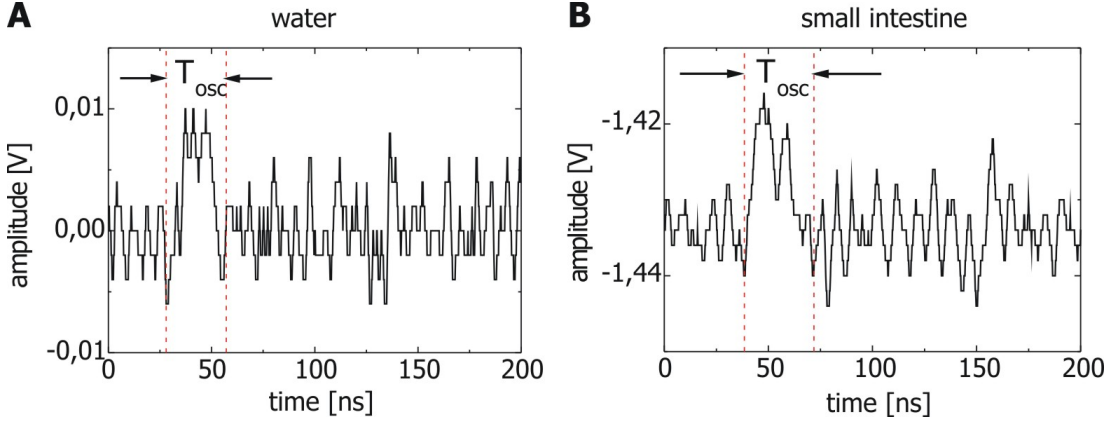


**Figure 6.1:** Scattering signals at the threshold for bubble formation in water (A) and in murine small intestinal epithelium (B). The threshold energies at  $NA = 1.2$  were 103 nJ for water and 33 nJ for intestine, and the bubble oscillation time was  $T_{osc} = 29$  ns in both cases.

## 6.1 Bubble dynamics and size

During optical breakdown material in the laser focus is ionized and a plasma is formed [Linz 2010, Vogel et al. 2005] as has been described in section 3.2.1. The plasma expansion drives the emission of a shock wave and forms a cavitation bubble [Venugopalan et al. 2002, Vogel et al. 1996]. The lowest laser pulse energy at which cavitation bubbles are generated,  $E_{th}$ , depends, on the laser pulse duration, wavelength, the numerical aperture used for focussing, and on the local optical absorption properties of the material. With  $NA = 1.2$ , the threshold energy  $E_{th}$  for bubble formation in water was 103 nJ. In small intestinal mucosa it was a factor of 3 lower (33 nJ). The reduced energy threshold for bubble formation in mucosa is due to the enhanced linear and nonlinear absorption of UV light in biological tissues. Tissues contain many biomolecules which possess energy levels within the band gap of water with a fairly long lifetime ( $\approx 1$  ns). Excited state absorption from these electronic states enables a stepwise ionization that reduces the threshold for optical breakdown [Czochralska and Lindqvist 1983, Hutson and Ma 2007]. Figure 6.1 shows the scattering signals at the bubble formation thresholds in water and small intestine. The oscillation time,  $T_{osc}$ , of the smallest detectable cavitation bubbles was 29 ns in both media.

Figure 6.2 shows typical scattering signals for medium-sized bubbles in water and

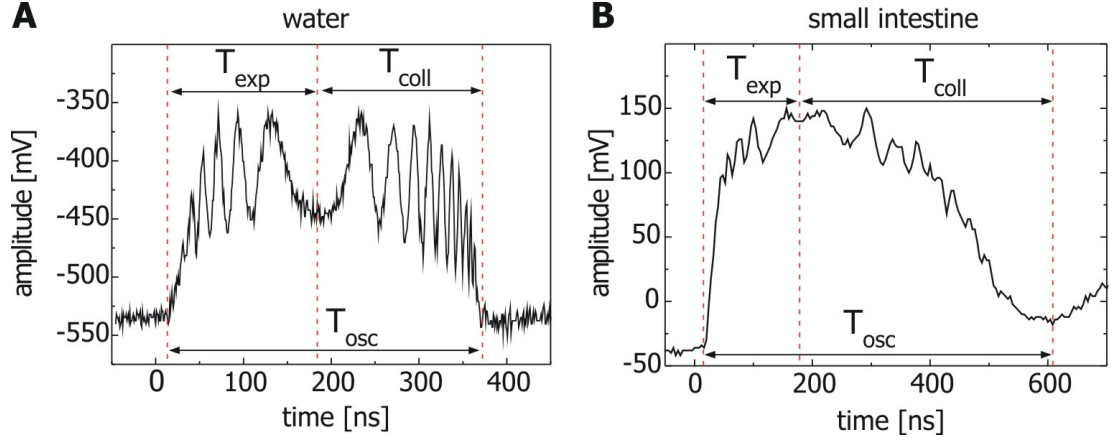


**Figure 6.2:** Interferometric signal from backscattering at a cavitation bubble in water (A) and in small intestine (B). Oscillation times  $T_{osc}$  as well as expansion and collapse times  $T_{exp}$  and  $T_{coll}$  are marked and amount to: (A)  $T_{osc} = 356$  ns,  $T_{coll}/T_{exp} = 1.05$  (B)  $T_{osc} = 596$  ns,  $T_{coll}/T_{exp} = 2.47$

in small intestinal epithelium. In water (Fig. 6.2 A), the bubble is perfectly spherical, and the signal amplitude is strongly modulated due to alternating constructive and destructive interference of probe-beam light reflected at the bubble front and back wall. The frequency of these interference fringes decreases with decreasing bubble wall velocity during bubble expansion and increases again with increasing bubble wall velocity during the collapse phase. The time until the bubble has reached its maximum expansion,  $T_{exp}$ , can be readily determined from beginning of the signal and the point at which the fringe frequency is lowest. In analogous fashion the collapse time,  $T_{coll}$ , was determined. The times for bubble expansion,  $T_{exp}$ , and collapse,  $T_{coll}$ , are almost equal ( $T_{coll}/T_{exp} = 1.05$ ).

Scattering signals in epithelial cells of the small intestine as shown in Fig. 6.2 B differ markedly from the scattering signals in water. The modulation of the interference fringes is much less pronounced, because the bubbles are not perfectly spherical due to local inhomogeneities of the mechanical properties of the cell content that will influence the bubble dynamics. Moreover, the collapse phase takes significantly longer than bubble expansion ( $T_{coll}/T_{exp} = 2.47$ ), i. e. signals are asymmetric in time. Finally, the signal amplitude does not recover its original baseline value after the first bubble oscillation, but keeps a small positive value and then increases again due to a rebound of the oscillating bubble.

## 6. UV-LASER MICROSURGERY AND TISSUE RESPONSE

---

Why does the bubble rebound in intestine but not in water? Water has a low viscosity, and cavitation bubbles in water contain mainly water vapour that condenses at the bubble wall during bubble collapse. This leads to a very intense collapse during which a great part of the bubble oscillation energy is dissipated in form of a shock wave [Lauterborn and Vogel 2013]. For small bubbles, the collapse is further intensified by surface tension  $\sigma$  which adds a pressure term proportional  $\sigma/r$ . For bubbles with radii smaller than  $1 \mu\text{m}$  the additional pressure becomes larger than the atmospheric pressure. Due to the strong shock wave emission, it remains not sufficient energy for a rebound after collapse [Paltauf and Schmidt-Kloiber 1996]. By contrast, in small intestinal epithelium non-condensable gaseous compounds fill the cavitation bubble that are formed during plasma formation due to the dissociation of biomolecules. The collapse is therefore attenuated by the compressibility of this gas. Another attenuating factor is viscous damping of the tissue. Thus, after collapse a small gas-filled residual bubble remains that continues to scatter the probe beam. The bubble rebounds despite the viscosity of the tissue, because only a small fraction of the oscillation energy was converted into an acoustic transient.

In water the maximum bubble radius  $R_{max}$  can be calculated directly from the measured oscillation times [Rayleigh 1917, Vogel et al. 2008]. In tissue, determination of  $R_{max}$  from  $T_{osc}$  would lead to erroneous results because the collapse phase is prolonged by viscous damping. However, we shall see that a reasonable value for  $R_{max}$  can still be obtained based on the bubble expansion time  $T_{exp}$ . The elastic forces act symmetrically on bubble expansion and collapse – in a similar fashion as surface tension, which counteracts bubble expansion and accelerates collapse. For the same laser energy,  $T_{osc}$  is thus shorter and  $R_{max}$  smaller in an elastic medium than in water. However, for the same oscillation time,  $R_{max}$  is larger in an elastic medium than in water. In an elastic medium such as porcine lens, Vogel et al. found  $R_{max}$  to be 13 % larger for a given bubble oscillation time than in water (unpublished data). By contrast, plastic deformation and viscous damping distort the symmetry of the bubble oscillation, mainly by prolonging the collapse phase. In the extreme case of aperiodic damping,  $T_{osc}$  can become infinitely large while  $T_{exp}$  still remains finite [Brujan and Vogel 2006, Lauterborn 1974]. Therefore, we define a virtual oscillation time  $T'_{osc} = 2T_{exp}$  and calculate  $R_{max}$  from  $T'_{osc}$  as for water. The calculated  $R_{max}$  values for murine small intestinal epithelium are slightly underestimated due to the use of water parameters in

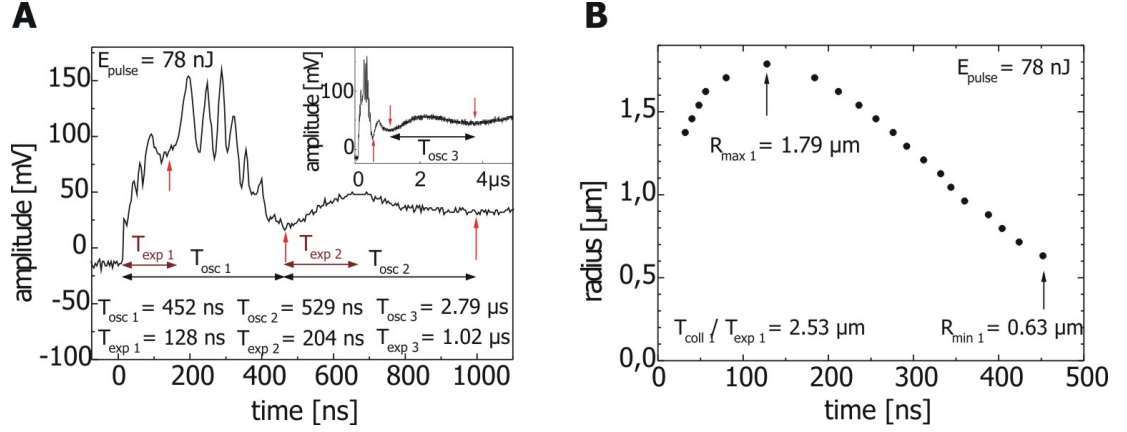


**Figure 6.3:** Scattering signal (A) and radius-time curve (B) of a cavitation bubble produced with  $E_{\text{pulse}} = 78 \text{ nJ}$ . This energy corresponds to the small-bubble regime (I) in Fig. 7. The inset in (A) shows the same signal at a longer time scale.  $T_{\text{exp 1}}$  and the endpoints of the first, second and third oscillation are marked with red arrows.

the Gilmore model, because we neglect the elastic forces during expansion. However, the error will be smaller than the above mentioned 13 % determined for lens tissue, because mucosa is much softer and behaves more similar to water.

By evaluating all interference fringes starting from  $R_{\text{max}}$  obtained from  $T'_{\text{osc}} = 2T_{\text{exp}}$ , we can determine the radius-time curve of the bubble oscillation [Linz et al. 2013] (Figs. 6.3 and 6.4). We evaluate the  $R(t)$  curve considering that each complete fringe represents a radius change of  $1/4$  of the probe laser wavelength  $\lambda$  (660 nm). The bubble walls act as confocal mirrors of an interferometer with pathlength difference  $\Delta x$  of twice the bubble diameter  $d$ . Constructive interference occurs if  $\Delta x = 2d = 4R = n\lambda$ , with  $n$  being a natural number. Therefore, one fringe corresponds to a diameter change of  $\lambda/2$  and a radius change of  $\lambda/4$ . If interference maxima and minima both are evaluated, the  $R(t)$  curve is obtained in steps of  $\lambda/8 = 82.5 \text{ nm}$ . In the early expansion phase of large bubbles, not all interference fringes can be resolved due to the high velocity of the bubble wall that results in oscillation frequencies at the photodetector which exceed the detector bandwidth. In some cases, this is also true for the late phase of the first bubble collapse. However, fairly often collapse and rebound of bubbles in tissue are so slow that all fringes can be resolved and a continuous  $r(t)$  curve is obtained through first and second bubble oscillation (Fig. 6.4).

Figure 6.3 shows the scattering signal (A) and radius-time curve (B) for a cavitation

## 6. UV-LASER MICROSURGERY AND TISSUE RESPONSE

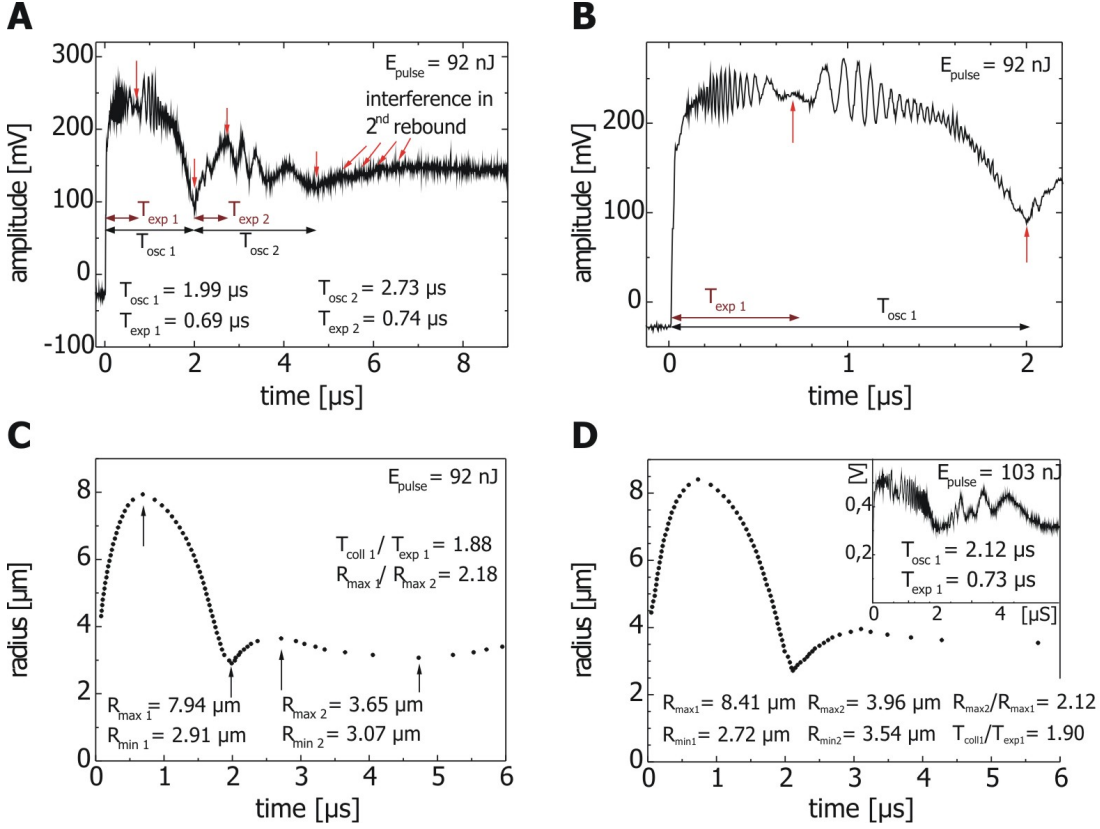


**Figure 6.4:** Scattering signal in two different time scales (**A**, **B**) and radius-time curve (**C**) of a cavitation bubble produced with  $E_{pulse} = 92 \text{ nJ}$ .  $T_{exp}$ ,  $T_{osc}$  are indicated with arrows. (**D**) Radius-time curve for a cavitation bubble produced with  $E_{pulse} = 103 \text{ nJ}$ . The inset shows the corresponding scattering signal. (In (**C**) and (**D**) only interference maxima were evaluated for the first bubble oscillation, while in the second and third oscillation maxima and minima were used.)

bubble produced with  $E = 78 \text{ nJ}$ . During the first bubble oscillation, the amplitude modulation due to interference is clearly visible. The inset shows the same signal on a longer timescale. Two rebounds were observed as slow increase and decrease of the signal amplitude without interference fringes. We measured  $T_{osc,1} = 452 \text{ ns}$ ,  $T_{exp,1} = 128 \text{ ns}$ . Because of the viscous damping, the collapse phase of the first oscillation takes 2.53 times longer than the bubble expansion. The duration of the second and third oscillation were  $T_{osc,2} = 529 \text{ ns}$ ,  $T_{osc,3} = 2.79 \mu\text{s}$  and thus significantly longer than the primary oscillation. The radius-time curve in 5B shows clearly the strongly damped collapse phase in comparison to the bubble expansion. The collapse phase takes 2.53

times longer than bubble expansion. Further, while in water the bubble wall velocity increases during the whole collapse phase, here the bubble wall velocity increases only during the first half of the collapse phase and then is slowed down before the minimum radius is reached. The maximum bubble radius was determined to  $R_{max,1}(2T_{exp}) = 1.79 \mu\text{m}$  and the residual bubble radius before the first rebound is  $R_{min,1} = 0.63 \mu\text{m}$ .

Figure 6.4 shows the scattering signals and radius-time curves for cavitation bubbles ( $R_{max} \geq 8\mu\text{m}$ ) produced with higher pulse energies of  $E = 92 \text{ nJ}$  (A-C) and  $E = 103 \text{ nJ}$  (D). The signal in 6.4 A exhibits interference fringes up to the third oscillation. Figure 6.4 C shows the resulting complete radius-time curve up to 6 microseconds after the optical breakdown, and Fig.6.4 D shows a similar curves for another bubble. The  $R(t)$  curves in Fig. 6.4 exhibit a weaker asymmetry during the first oscillation than for the smaller bubbles in Fig. 6.3. In this respect, the oscillation dynamics start to resemble the bubble dynamics in water. However, the minimum bubble radius during the first collapse is much larger than it would be in water, and the damped oscillation of the  $R(t)$  curve converges towards a final radius value. This convergence reflects the permanent tissue rupture caused by the rapid initial bubble expansion.

For an online dosimetry of laser effects, we do not need to know the entire  $R(t)$  curve of the cavitation bubble but can use the maximum bubble radius derived from  $2T_{exp}$ . Fig. 6.5 shows  $R_{max}$  as a function of pulse energy for single UV laser pulses focussed with  $\text{NA} = 1.2$  into murine gut mucosa. We excluded those scattering signals, for which  $T_{exp}$  could not be clearly determined. Therefore, data from very small bubbles produced close to threshold, such as in Fig. 6.1, are missing. We can identify two distinct regimes with different bubble sizes. Regime I contains small bubbles with  $R_{max} = 0.6 \mu\text{m} - 2.4 \mu\text{m}$ , while regime II contains larger bubbles with  $R_{max} = 7.3 \mu\text{m} - 25.6 \mu\text{m}$ . The two regimes reflect the two steps of optical breakdown with UV ns laser pulses in transparent dielectrics that have been first observed by Linz [Linz 2010]. Regime I corresponds to a low density plasma (LDP) while regime II is associated with high-density plasma (HDP) emitting a bright luminescence. For optical breakdown in water, both regimes are separated by a sharp energy threshold [Linz 2010]. By contrast, in intestinal epithelium the regimes show a certain overlap in terms of energy although a distinct gap is observed between the bubble sizes. This overlap in the energy range of 84-94 nJ is probably due to local inhomogeneities of linear and nonlinear tissue absorption properties. The change of optical breakdown dynamics due to variations of

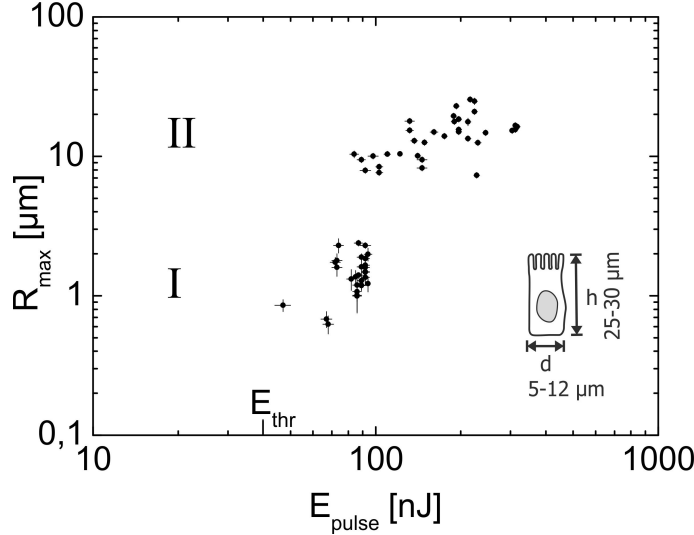


**Figure 6.5:** Maximum bubble radius  $R_{max}$  as a function of pulse energy after application of single UV laser pulses (355 nm, 0.5 ns) focussed with NA 1.2 into intestinal epithelium. Error bars reflect the uncertainty in the determination of  $T_{osc}$  and  $T_{exp}$ . Two distinct regimes with different bubble sizes are observed: **I**) bubbles with  $R_{max} = 0.6 - 2.4 \mu\text{m}$ , and **II**) bubbles with  $R_{max} = 7.3 - 25.6 \mu\text{m}$ . The cartoon in the lower right corner illustrates the dimensions of an epithelial cell in the small intestine.

the molecular content in the laser focus highlights the need for an online monitoring of the lesion size. In addition, once a  $R_{max}(E)$  data set such as in Fig. 6.5 is available, it can serve as calibration curve that enables to produce lesions of predictable size. For example, bubbles in the LDP regime can be reproducibly generated in the energy range between 33 nJ ( $E_{th}$ ) and 80 nJ.

The bubbles in the two regimes differ not only in size but also in their oscillation dynamics. Figure 6.6 shows the ratio of collapse time and expansion time,  $T_{coll}/T_{exp}$ , as a function of the expansion time. This ratio measures the asymmetry of the bubble oscillation dynamics owing to the visco-elastic-plastic tissue properties. The asymmetry decreases with increasing bubble size. It is most pronounced in the LDP regime where viscosity has a strong damping effect on bubble collapse, because the influence of viscosity is proportional to  $1/R$  [Lauterborn 1974, Paltauf and Schmidt-Kloiber 1996].  $T_{coll}/T_{exp}$  reaches a value of 4.8 for  $R_{max} = 0.6 \mu\text{m}$  and drops to 1.8 for  $R_{max} = 2.4 \mu\text{m}$ . With increasing bubble size inertial forces become ever more important, and the oscillation behavior becomes more similar to that of bubbles in water for which expansion

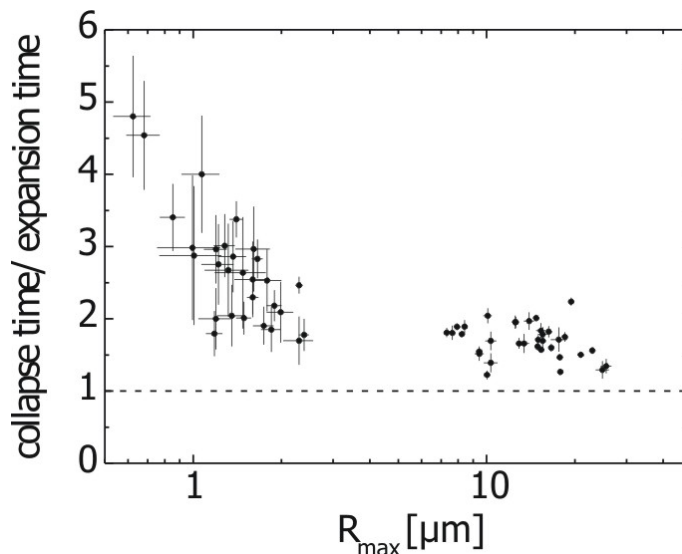


**Figure 6.6:** Bubble oscillation asymmetry (collapse time/expansion time) in murine small intestinal mucosa as a function of maximum bubble radius. Error bars reflect the uncertainty in the determination of  $T_{osc}$  and  $T_{exp}$ .

and collapse phase are largely symmetric [Linz et al. 2013]

Creation of bubbles of different size was used to investigate the tissue response to lesions of different size as will be described in sections 6.2.1 and 6.2.2. During each experiment, the bubble size was determined online.

## 6.2 Tissue response to laser-induced lesions

### 6.2.1 Tissue response to small cavitation bubbles

In this section, the effects of small type I bubbles with a maximum radius  $R_{max} = 0.6 - 2.2 \mu\text{m}$  are discussed. These bubbles are much smaller than the dimensions of a typical epithelial cell with  $25-30 \mu\text{m}$  height and  $5-12 \mu\text{m}$  diameter. Already at the bubble formation threshold ( $33 \text{ nJ}$ ) targeted cells appear dark due to a loss of autofluorescence, which is most likely attributed to destruction of mitochondrial NAD(P)H. Figure 6.7 shows this type of damage for  $E_{pulse} = 68 \text{ nJ}$  and a bubble radius of  $1.9 \mu\text{m}$ . The corresponding Movie 6.7 covers the first 20 minutes after the UV laser pulse. When only single cells are affected by laser surgery, the darkening of the target-cell is the only response observed within the observation period of 30 minutes. The oscillation of

## 6. UV-LASER MICROSURGERY AND TISSUE RESPONSE

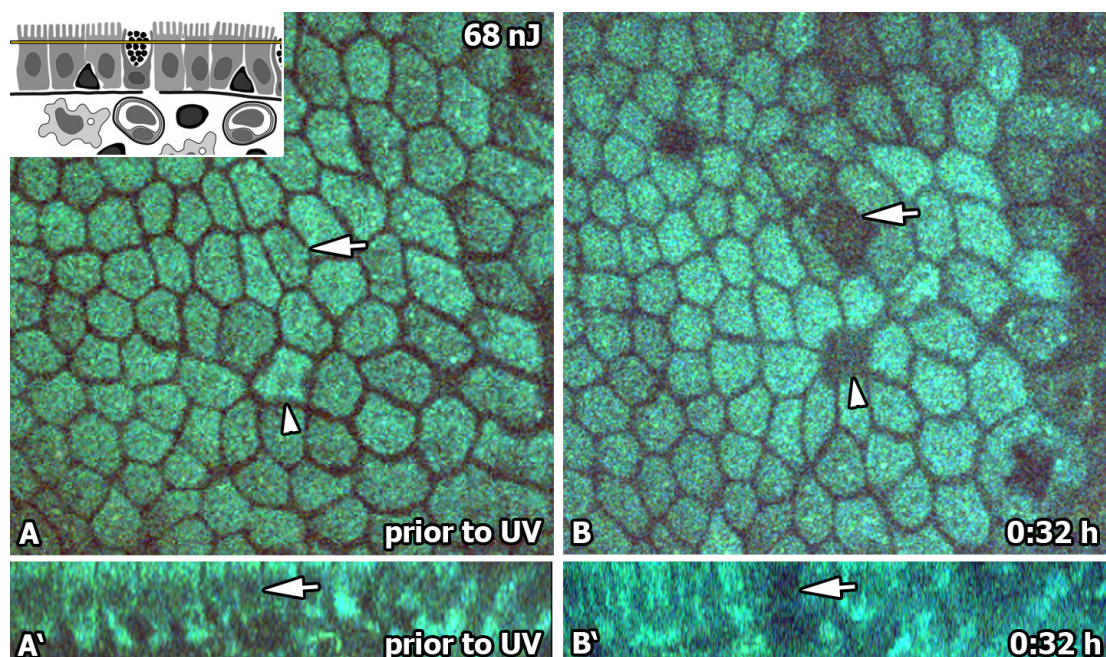


**Figure 6.7:** Movie 6.7. Small intestinal mucosa before (**A**, **A'**) and 32 min. after (**B**, **B'**) application of a single UV ns laser pulse with  $E_{pulse} = 68$  nJ corresponding to a maximum bubble radius of  $1.9 \mu\text{m}$ . The drawing in **A** shows the imaging plane of **A** and **B**. **A'** and **B'** are sectional side views from the target cell showing the epithelial layer, basement membrane and underlying lamina propria. (**B**, **B'**) Within 32 Minutes after UV laser surgery, the target cell (arrow) loses autofluorescence and turns dark but remains within the epithelium. (**A**, **B**) The arrowhead shows an enterocyte undergoing normal cell shedding. A time-lapse movie covering the first 20 minutes after application of the laser pulse is shown in Movie 6.7. Scale bar  $15 \mu\text{m}$ .

the bubble destroys neither the cell membrane nor junctional complexes to neighboring cells, and basal cell-matrix interactions remain intact. This could be verified by the lack of uptake of propidium iodide (PI), when a PI solution was applied to the mucosal surface. In the field of view in Fig. 6.7 a second cell that was not hit by the UV laser pulse is shed into the lumen. This becomes apparent in Movie 6.7: the cell being shed becomes a 'blurry' look, because it moves towards the microscope objective and thus out of focus. The fact that the physiological cell shedding continues to take place even though the villus has been locally damaged by UV laser irradiation indicates that the normal function of the organ is sustained.

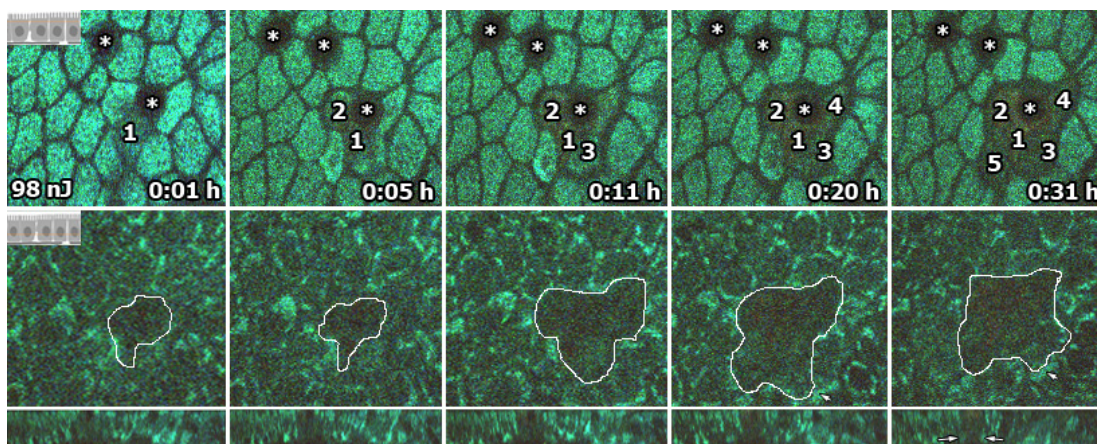


**Figure 6.8:** Small intestinal mucosa after application of a single UV ns laser pulse with  $E_{pulse} = 98$  nJ. Schematic drawings show the focus plane of (A-E and A'-E'). (A-E) View of the apical cytoplasm of small intestinal epithelium showing the target cell (1) and four neighbouring cells turning dark within 31 minutes. \* goblet cells. (A'-E') View from the basal part of small intestinal epithelium the first 31 minutes after laser irradiation. Spreading of the damage. After 31 minutes, epithelial cells move toward the injured area to cover the denuded area (arrow). (Scale bar,  $10 \mu\text{m}$ ). **Movie 6** shows the time-lapse of the apical imaging plane corresponding to the upper row in this figure.

### 6.2.2 Tissue response to large cavitation bubbles

When large bubbles with radii  $> 7 \mu\text{m}$  (type II in Fig. 6.5) are produced in the targeted cell, autofluorescence is lost within the first minute after the laser pulse (Figs. 6.8 - 6.10). Within 31 minutes after the laser pulse, the damage has spread and encompassed five (Fig. 6.8, Movie 6.8) or even ten and more adjoining cells (Fig. 6.9) which also lose their autofluorescence. Since the bubbles are larger than the targeted enterocyte, cell membrane, lateral junctional complexes and basal cell-matrix interactions including the basement membrane are destroyed, leading to necrosis. This could be verified by uptake of PI by the cell nucleus shown in Figs. 6.8 and 6.10 and the corresponding Movies 6.8 and 6.10.

Already within one minute after creating the laser lesion, we observed an immune response: polymorphonuclear leucocytes (PMNL), which belong to the innate immune system, accumulated within the area of necrosis (Fig. 6.9 and Movie 6.9, Fig. 6.10 and Movie 6.10). PMNL contain a segmented lobular nucleus connected by strands of chromatin and are mostly neutrophil granulocytes. They have an average diameter

## 6. UV-LASER MICROSURGERY AND TISSUE RESPONSE

---

of 12-15  $\mu\text{m}$  and are highly motile (Movie 6.9). Neutrophil granulocytes are the first immune cells to arrive at a site of inflammation due to chemotaxis (see also Sect. 2.1). In this case, they follow chemical signals arising from the lesion site. To confirm that the invading cells observed in Figs. 6.9 and 6.10, are indeed PMNL, Fig. 6.11 compares a PMNL as seen in the two-photon microscopic images (B, C) with a Pappenheim stained blood cell smear (A). The characteristic, segmented lobular nucleus is recognized as dark structure surrounded by brighter autofluorescent cytosol in the two-photon microscopic images.

Necrotic cells are a source of damage associated molecular patterns (DAMPs) which recruit and activate innate immune cells, aimed at restoration of homeostasis and tissue repair [Bianchi 2007, Lotze et al. 2007]. The observation of PMNL after creation of 10-20  $\mu\text{m}$  large bubbles suggests that the induced necrosis triggered the production of DAMPs followed by directed migration of neutrophil granulocytes into the damaged area. Adenosine triphosphate released by the dying cells further helps neutrophils attach to the blood vessels walls [McDonald et al. 2010], so that neutrophils can be recruited easily from the venules in the lamina propria and move toward the injured area. Their phagocytic functions probably contribute to the clearance of debris [Kono and Rock 2008] and neutrophils are known to be key cells regulating the switch from proinflammatory to anti-inflammatory conditions [Serhan and Savill 2005].

The immediate tissue response of PMNL migration was followed by extrusion of necrotic cells into the lumen and epithelial restitution that becomes visible in the basal part of the epithelium after a few minutes (Fig. 6.10, Movie 6.10). Healthy epithelial cells adjacent to the injured area migrate into the wound with an measured speed of 0.4  $\mu\text{m}/\text{min}$  to cover the denuded area. These migrating cells form pseudopodia-like structures, reorganize their cytoskeleton, and redifferentiate after closure of the tissue defect [Nusrat et al. 1992]. Villus contraction as indicated by the arrows in Fig. 6.9 C aids epithelial restitution by effectively reducing the size of the injured surface area to be reepithelialized. Contraction is likely achieved by condensation of microfilaments in cytoplasmic processes of subepithelial myofibroblasts [Moore et al. 1989a]. Epithelial restitution provides a rapid mechanism for covering a defect in the barrier but does not involve proliferation of epithelial cells.

After 2 hours at the latest, the large tissue defects were completely healed and the epithelial continuity was established again, resulting in a normal epithelial lining

## 6.2 Tissue response to laser-induced lesions

---

(Fig. 6.10 D, D'). However, epithelial cells were flattened and not as columnar as in undamaged epithelium. Epithelial cell proliferation, maturation and differentiation are necessary to replenish the decreased cell pool. The proliferative compartment of epithelial cells is localized in the crypt region, and in normal physiological turnover a gradient of increasingly differentiated epithelial cells is moving along the vertical axis to the villus tip. This process of cell proliferation and differentiation takes about 24 to 96 hours. Therefore, cells damaged by external factors such as laser lesions cannot be replaced by new cells in a few hours after injury, but the process of proliferation and differentiation may be enhanced by regulatory peptides, such as growth factors and cytokines [Podolsky 1997, Wilson and Gibson 1997]. These peptides may also be produced by innate immune cells, such as PMNL invading in the damaged region.

When epithelial integrity was established again, PMNL were no longer visible within the tissue. Apoptosis of PMNL causes specific recognition and clearance by macrophages that starts the process of egress from the injured tissue to the draining lymphatics [Savill 2001]. Since the necrotic cells were extruded into the lumen, there was no further source of chemoattractants for PMNL anymore.

The fast clearance mechanism of injured cells into the lumen is probably unique to organs such as intestine and lung. In other organs, such as heart, brain, kidney or liver, damaged cells remain in situ, since they cannot be removed from the organs and cleared from the body. In such organs, a further inflammatory response is elicited amongst others to clear away the injured cells [Daemen et al. 2002, Jaeschke 2003, Lee et al. 2000].

## 6. UV-LASER MICROSURGERY AND TISSUE RESPONSE

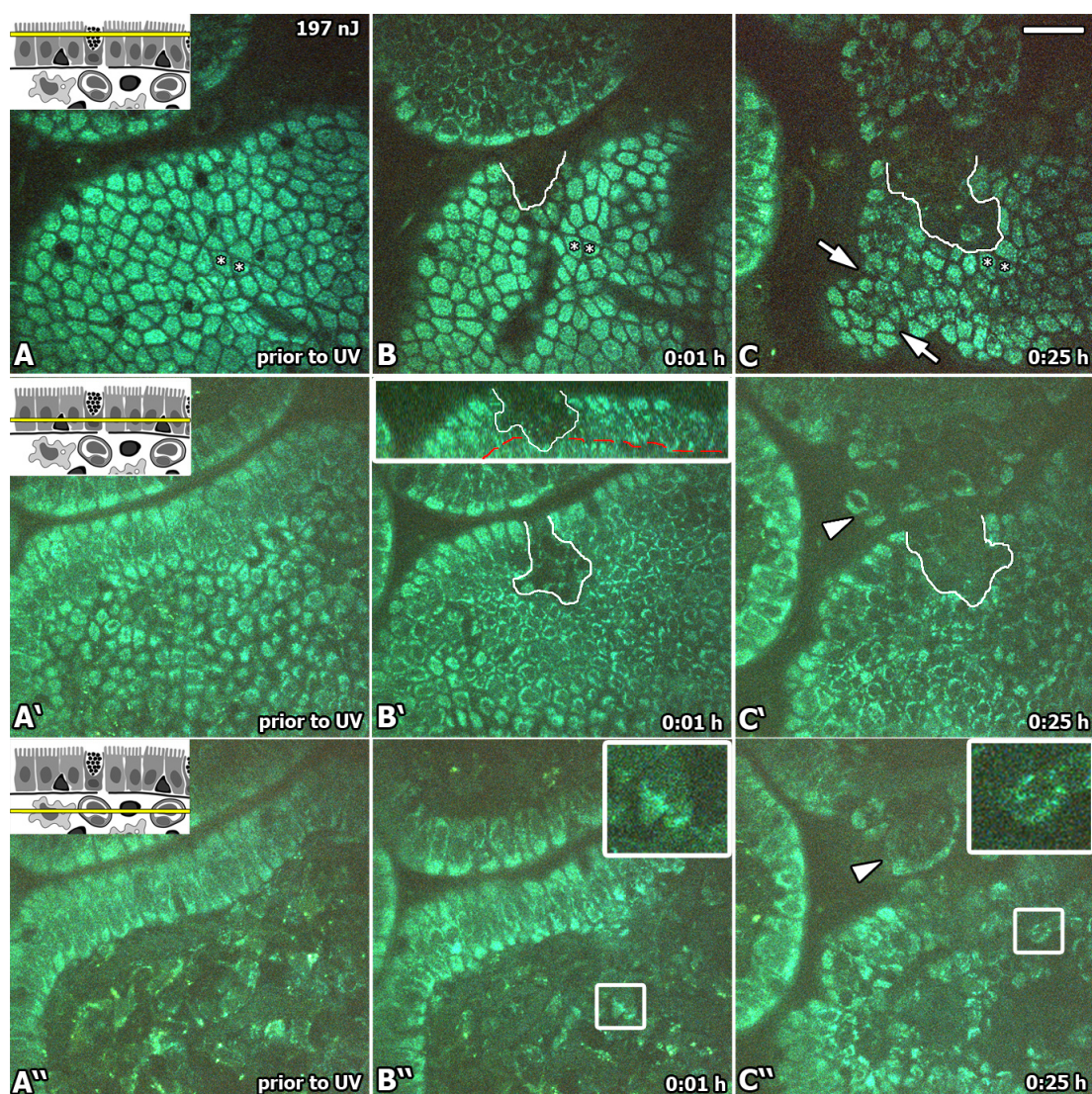


**Figure 6.9:** Small intestinal mucosa after application of a single UV ns laser pulse with  $E_{pulse} = 197$  nJ. Schematic drawings show the focus plane of (A-C, A'-C' and A''-C''). (B, B', B''). One minute after UV ns laser pulse already more cells than the target cell lost autofluorescence. The insert (yellow frame), in B' shows a sectional side view of the affected area, marked with a yellow line, showing that the basement membrane (red) is disrupted. The insert (white frame) in B'' shows a polymorphnuclear leucocyte in the lamina propria. (C, C', C'') 25 minutes after UV ns laser pulse showing villus contraction (arrows) and further spread of the damage. Necrotic cell material appears in the lumen (arrowheads). Insert (white frame) in C'' shows another polymorphnuclear leucocyte. \* Two cells are marked for orientation. (Scale bar,  $10 \mu\text{m}$ ) **Movie 7** shows the image stack through the villus 25 minutes after application of the UV laser pulse, corresponding to column C in the figure. Polymorphnuclear leucocytes are indicated with white arrows.

## 6.2 Tissue response to laser-induced lesions

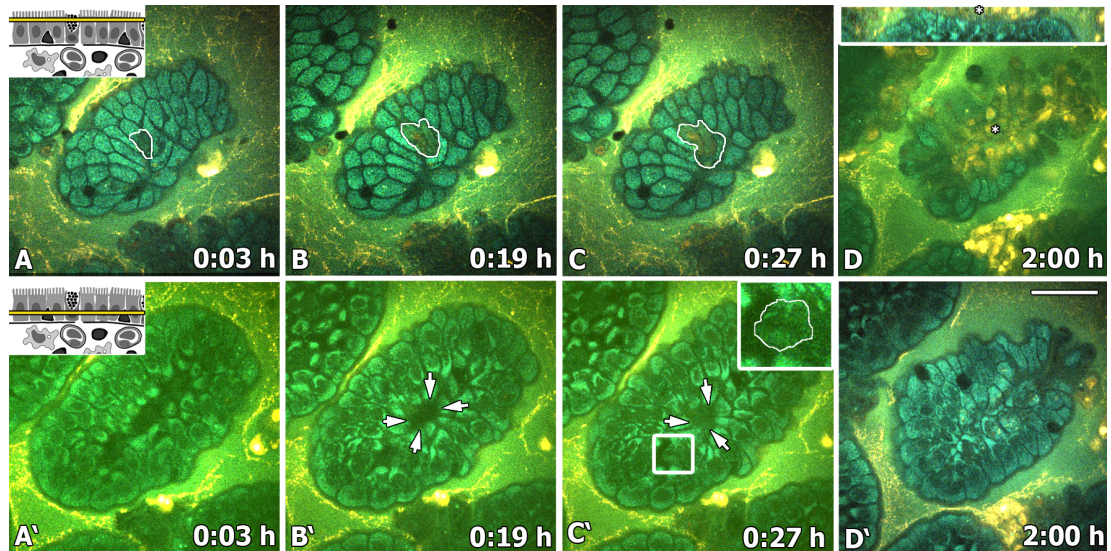


**Figure 6.10:** Time series of small intestinal mucosa after application of a single UV ns laser pulse and luminal application of propidium iodide (PI). Schematic drawings show the focus plane of (A-D and A'-D'). (A-C) The target cell and two adjacent cells lost autofluorescence and take up PI. (A'-C') Epithelial restitution (arrows) is seen in the basal part of the epithelium. The insert (white frame) in C' shows a polymorphnuclear leucocyte. (D, D') Two hours after UV ns laser pulse necrotic cells (\*) that took up PI are seen above the villus (insert: cross sectional view). In the basal part of the epithelium (D') the defect is sealed. (Scale bar, 20  $\mu\text{m}$ ). **Movie 8** shows a time lapse of the focus plane in A'-C' covering minutes 3-27 after application of the UV laser pulse. The sequence is repeated 9 times. Epithelial restitution and a polymorphnuclear lymphocyte are highlighted in the movie.

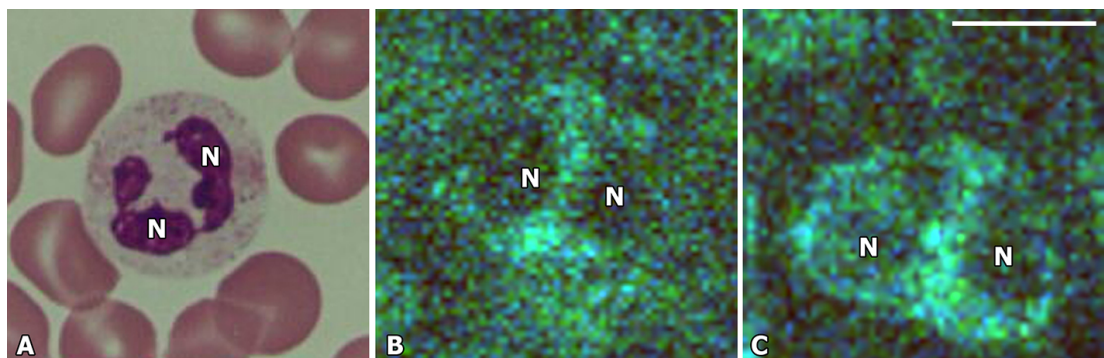


**Figure 6.11:** (A) Polymorphnuclear leucocyte in Pappenheim stained blood cell smear. (B; C) Two-photon excited autofluorescence images of polymorphnuclear leucocytes in small intestinal mucosa after application of type II bubbles. Nucleus N. (Scale bar, 10  $\mu\text{m}$ )

### 6.3 Conclusions

It was demonstrated that autofluorescence-based two-photon microscopy combined with UV-ns laser-surgery can be used as tool for the intravital investigation of immune and healing response to minute injuries of gut mucosa, which is an important and large interface between body and environment. Microlesions were produced using the disruptive action of cavitation bubbles that are generated by optical breakdown with focussed UV ns laser pulses. The cavitation bubbles' size and dynamics were monitored online, using a probe-beam backscattering technique with  $\approx 5$  ns temporal and  $\approx 80$  nm spatial resolution.

Bubbles were produced in two size regimes. In regime I, the maximum radius stayed below  $2.5 \mu\text{m}$ , much smaller than the typical size of an enterocyte. Here, the target cell exhibited a loss of autofluorescence but no membrane damage occurred, neighbouring cells were not affected, and no immune response was observed. In regime II, where bubble radii ranged between  $7$  and  $25 \mu\text{m}$ , the target cell underwent immediate necrosis, and 5-10 neighbouring cells were affected and lost the integrity of their membranes. Within a few minutes after UV laser exposure, polymorphonuclear leucocytes, a type of innate immune cells, migrated into the damaged region and damaged cells were expelled into the intestinal lumen. The lesions healed within 2 hours by stretching and migration of adjacent healthy epithelial cells, reestablishing the integrity of the epithelial surface.

Coverage of the lesion by adjacent cells is possible in healthy tissue but may fail under pathologic conditions where the state and number density of epithelial cells is already compromised and the homeostasis of the epithelium is highly dysregulated. Epithelial homeostasis, that is, the physiological balance of epithelial cell proliferation, differentiation, and apoptosis, is essential for the maintenance of the barrier function. Affections of the barrier functions like inflammatory bowel disease, are still not adequately understood and lead to severe tissue damage and massive impairment of concerned patients. This research will serve as a base for future studies that will investigate how the intestine reacts to microlesions in the case of an existing inflammation and dysregulated homeostasis of the tissue.

The approach presented in this work may also be useful for the investigation of tissue response to microlesions in other exposed surfaces such as corneal and bronchial

### **6.3 Conclusions**

---

epithelia. Comparison between normal and pathological conditions may elucidate tissue response mechanisms relevant for diseases of the cornea (e.g. dry eye) or the respiratory tract (e.g. asthma).

## **6. UV-LASER MICROSURGERY AND TISSUE RESPONSE**

---

# 7

## Outlook

In this work, unique insights could be gained into the immunologically important environment of living small intestinal mucosa. In the first part of this work, it was shown that solely based on cellular autofluorescence, time-lapse two-photon excited fluorescence microscopy revealed the dynamics of physiologic processes in healthy murine intestinal villi, such as peristalsis, cell shedding, and lymphocyte movements. Quantitative excitation-emission spectra of autofluorescence were acquired for villus enterocytes, lysosomes in enterocytes, and antigen-presenting cells in the lamina propria of villi and dome areas. It was shown that these two-dimensional ‘spectral fingerprints’ exhibit characteristic features, which allow a discrimination of different cell types and cell organelles. For example, highest contrast between antigen-presenting cells (APCs) and the surrounding tissue is achieved, when the two excitation wavelengths, 730 nm and 820 nm, are used to create one overlay-image. However, sequential image recording at different excitation wavelengths hampers this imaging mode in dynamic systems. Simultaneous imaging by interlaced excitation with two or more different wavelengths could in future help to follow individual APCs with high contrast in the superimposed images. Further, implementing an algorithm that evaluates images automatically based on the spectral fingerprints acquired in this study, could pave the road for automated and real-time identification of specific cell types and cell organelles that is required to quantitatively follow immunological cell-cell interactions.

Tissue damage in form of hyperfluorescent regions was induced by scanning laser irradiation above a certain power. These lesions formed suddenly and grew fast during further irradiation. Such damage is an unwanted side-effect during imaging and must

## 7. OUTLOOK

---

be avoided. The excitation-emission spectrum of the hyperfluorescence was analyzed in this thesis and showed that it arises from new fluorescent chemical substances that are not present in normal intestinal epithelium. Other authors made similar observations in cultured cells [Tiede and Nichols 2006] and collagenous tissue [Hovhannisyan et al. 2008], and proposed the generation of lipofuscin or tyrosine-photoproducts respectively. Lipofuscin itself is a photoinducible free radical generator Boulton et al. [1993] and can explain the fast growth of the lesions when further irradiated. However, the fluorescence emission spectra of lipofuscin and tyrosine-photoproducts do not match the hyperfluorescence spectra measured in this work. In order to determine the exact composition of the hyperfluorescent substance, further investigations with higher spectral resolution and additional analysis of the fluorescent lifetimes are needed. It further remains an open question whether these substances are formed directly by photochemistry [Vogel et al. 2005] or by cellular metabolism that is altered due to photoinduced stress. It is known that scanning laser irradiation generates reactive oxygen species (ROS) by photochemical processes eventually leading to apoptosis-like cell death [Tirlapur et al. 2001]. First studies have measured irradiance thresholds [Denton et al. 2006] or dependence on the pulse repetition rate [Baumgart et al. 2009] for ROS generation in excised tissue *in vitro*. In this study, roughly two times the average excitation power that was used for imaging led to hyperfluorescence, indicating that it is an irradiance-dependent process. Hovhannisyan et al. [2010] proposed a rate-equation model that describes the rate of collagen-photomodification in cornea and found that it depends on the irradiance to the power of six, while Tiede and Nichols [2006] found a dependence of the rate of lesion formation on the laser power to the power of four. Since nonlinear *in vivo* imaging is becoming more widely used and clinical applications are at hand [König 2008, König et al. 2007], it will be important to further investigate the dependence of tissue damage on laser parameters such as pulse duration, excitation wavelength, irradiance etc. in order to understand the underlying processes and characterize a safe parameter range for imaging. Hyperfluorescence can serve as a well-defined experimental criterion for the onset of damage.

In the second part of this work, the healthy situation at the mucosal interface was deliberately disturbed, and microscopic lesions were created in the small intestinal mucosa using UV laser-induced cavitation bubbles. The healing and immune response of the tissue was then observed by two-photon fluorescence microscopy. It was shown

---

that in a healthy individual only the largest of these small lesions provoke a reaction of the innate immune system characterized by the immigration of polymorphonuclear leucocytes. In all cases, the epithelium completely healed within two hours by expulsion of the damaged cells and closure of the lesion through migration of neighboring cells without further consequences for tissue homeostasis. This is a comforting certainty since small lesions of the intestinal mucosa occur frequently during normal digestion, and it certainly would have severe detrimental effects on the quality of life, if such small lesions would regularly provoke a massive immune reaction. In future, it will be interesting to study the reaction to small mucosal lesions in the case of an existing inflammation, for example in the case of chronic intestinal bowel diseases. In many cases, the disease has a relapsing course and becomes worse after incidents, which put the immune system in a state of alarm. However, it is poorly understood what are these incidents that provoke an acute flare-up of the disease. The method applied in this work enables to create microlesions at a predetermined location and time. In combination with an appropriate model for inflammatory disease this may help to answer these questions.

In this thesis, the focus was laid on the villi that are predominantly resorptive regions. In a next step, it will be interesting to study cellular interactions in the lymphatic tissue of the Peyer's patches, because these are specialized areas of the adaptive immune system. The experimental environment is already established, but to explore and understand immunological processes in detail, the investigative method should be able to recognize and track individual lymphocytes and recognize their specific cell type. With the setup used in this study, it is possible to track individual lamina propria lymphocytes in villi over 40 minutes by intraperitoneally injecting the nuclear dye Hoechst 33258 24 hours before the experiment [Klinger et al. 2012]. However, so far the lymphocyte class and specific function determined by the surface proteins of these cells cannot yet be attributed, because these molecules are not autofluorescent and the applied nuclear staining is unspecific. Use of genetically altered animals that express fluorescent proteins in specific cells, adoptive transfer of specifically labeled cells etc. in combination with two-photon excited time-lapse fluorescence microscopy could possibly resolve these limitations and open up new windows for the study and quantitative analysis of immunological processes on a cellular level.

## 7. OUTLOOK

---

The methods used in this thesis are not limited to the study of murine small intestine but can in principle be universally deployed to the surface of other exposed organs that are accessible for experimental investigation, for example cornea [Steven and Gebert 2009], skin or the respiratory tract.

---

## List of Movies

This work contains several time-lapse series or image stacks of two-photon excited fluorescence microscopic images. These are included on a CD-ROM in Apple Quicktime (\*.mov) or Microsoft audio video interleave (\*.avi) format and are part of this thesis. The movies are referenced in the text and numbered according to the figure number to which they belong. For example, Movie 5.1 belongs to Figure 5.1. The files on the DVD are named according to the figure number of the respective movie as listed in the table below. Additionally, the DVD contains a PDF-file of this thesis.

<b>Movie number</b>	<b>File name</b>	<b>Page number</b>
Movie 5.1	Movie5_1-villus_stack.mov	38
Movie 5.3	Movie5_3-villus_time_series.mov	41
Movie 5.4	Movie5_4-IEL-movement.mov	42
Movie 5.5	Movie5_5-cell_expulsion.mov	43
Movie 5.6	Movie5_6-transport_peristalsis.mov	43
Movie 5.12	Movie5_12-hyperfluorescence.avi	54
Movie 6.7	Movie6_7-small_damage.mov	68
Movie 6.8	Movie6_8-large_damage.mov	69
Movie 6.9	Movie6_9-large_damage_PMNLs.mov	71
Movie 6.10	Movie6_10-epithelial_restitution.mov	72

## 7. OUTLOOK

---

# References

- H. Bao, A. Boussioutas, J. Reynolds, S. Russell, and M. Gu. Imaging of goblet cells as a marker for intestinal metaplasia of the stomach by one-photon and two-photon fluorescence endomicroscopy. *J. Biomed. Opt.*, 14(6):64031, 2010. ISSN 1560-2281.
- J. Baumgart, K. Kuetemeyer, W. Bintig, A. Ngezahayo, W. Ertmer, H. Lubatschowski, and A. Heisterkamp. Repetition rate dependency of reactive oxygen species formation during femtosecond laser-based cell surgery. *J. Biomed. Opt.*, 14(5):054040, 2009.
- M. E. Bianchi. DAMPs, PAMPs and alarmins: all we need to know about danger. *J. Leukoc. Biol.*, 81:1–5, 2007.
- B. Boudaiffa, P. Cloutier, D. Hunting, M. A. Huels, and L. Sanche. Resonant Formation of DNA Strand Breaks by Low-Energy (3 to 20 eV) Electrons. *Science*, 287:1658, 2000. doi: 10.1126/science.287.5458.1658.
- M. Boulton, A. Dontsov, J. Jarvis-Evans, M. Ostrovsky, and D. Svistunenko. Lipofuscin is a photoinducible free radical generator. *J. Photochem. Photobiol. B: Biology*, 19(3):201–4, Aug. 1993. ISSN 1011-1344.
- M. Boulton, M. Rozanowska, B. Roanowski, and T. Wess. The photoreactivity of ocular lipofuscin. *Photochem. Photobiol. Sci.*, 3:759–764, 2004.
- P. Brandtzaeg, E. S. Baekkevold, I. N. Farstad, F. L. Jahnsen, F.-e. Johansen, E. M. Nilsen, and T. Yamanaka. Regional specialization in the mucosal immune system: what happens in the microcompartments? *Immunol. Today*, 20(3):141–151, 1999.
- R. T. Bronson. Ultrastructure of Macrophages and Karyolytic Bodies in Small Intestinal Villi of Macaque Monkeys and Baboons. *Vet. Pathol.*, 18(6):727–737, Nov. 1981. ISSN 0300-9858.
- E.-A. Brujan and A. Vogel. Stress wave emission and cavitation bubble dynamics by nanosecond optical breakdown in a tissue phantom. *J. Fluid Mech.*, 558:281–308, July 2006. ISSN 0022-1120.
- J. M. Brunk and V. P. Collins. Lysosomes and age pigments in cultures cells. In R. S. Sohal, editor, *Age Pigments*, pages 243–265. Elsevier/ North-Holland Biomedical Press, 1981.

## REFERENCES

---

- J. Büning, G. Hundorfean, M. Schmitz, K.-P. Zimmer, S. Strobel, A. Gebert, and D. Ludwig. Antigen targeting to MHC class II-enriched late endosomes in colonic epithelial cells: trafficking of luminal antigens studied in vivo in Crohn's colitis patients. *FASEB J.*, 20(2): 359–361, Feb. 2006. ISSN 1530-6860.
- P. J. Campagnola, A. C. Millard, M. Terasaki, P. E. Hoppe, C. J. Malone, and W. A. Mohler. Three-Dimensional High-Resolution Second-Harmonic Generation Imaging of Endogenous Structural Proteins in Biological Tissues. *Biophys. J.*, 81(May 2001):493–508, 2002.
- J. Chen, A. Lee, J. Zhao, H. Wang, H. Lui, D. I. McLean, and H. Zeng. Spectroscopic characterization and microscopic imaging of extracted and in situ cutaneous collagen and elastic tissue components under two-photon excitation. *Skin Res. Technol.*, 15(4):418–426, Nov. 2009. ISSN 1600-0846.
- Y. Chen, K. Chou, E. Fuchs, W. L. Havran, and R. Boismenu. Protection of the intestinal mucosa by intraepithelial gamma delta T cells. *Proc. Natl. Acad. Sci.*, 99:14338–14343, 2002.
- M. Chieppa, M. Rescigno, A. Y. C. Huang, and R. N. Germain. Dynamic imaging of dendritic cell extension into the small bowel lumen in response to epithelial cell TLR engagement. *J. Exp. Med.*, 203(13):2841–2852, Dec. 2006. ISSN 0022-1007.
- J. Colombelli, S. W. Grill, and E. H. K. Stelzer. Ultraviolet diffraction limited nanosurgery of live biological tissues. *Rev. Sci. Instrum.*, 75(2):472–478, 2004. ISSN 00346748. doi: 10.1063/1.1641163.
- J. Colombelli, E. G. Reynaud, and E. H. K. Stelzer. Investigating relaxation processes in cells and developing organisms: From cell ablation to cytoskeleton nanosurgery. In *Laser Manipulation of Cells and Tissues*, volume 82, pages 267–291. Academic Press Inc, 2007.
- J. M. Crawford and N. S. Braunwald. Toxicity in Vital Fluorescence Microscopy: Effect of Dimethylsulfoxide, Rhodamine-123, and Dil-Low Density Lipoprotein on Fibroblast Growth in vitro. *In Vitro Cell. Dev. Biol.*, 27A(8):633–638, 1991.
- B. Czochralska and L. Lindqvist. Biphotonic one-electron oxidation of NADH on laser excitation at 353 nm. *Chem. Phys. Lett.*, 101:297–299, 1983.
- M. A. Daemen, B. de Vries, and W. A. Buurman. Apoptosis and inflammation in renal reperfusion injury. *Transplantation*, 73:1693–1700, 2002.
- W. Denk, J. H. Strickler, and W. W. Webb. Two-photon laser scanning fluorescence microscopy. *Science*, 248(April):73–76, 1990.
- T. L. Denning, Y.-c. Wang, S. R. Patel, I. R. Williams, and B. Pulendran. Lamina propria macrophages and dendritic cells differentially induce regulatory and interleukin 17-producing T cell responses. *Nat. Immunol.*, 8(10):1086–1094, Oct. 2007. ISSN 1529-2908.

## REFERENCES

---

- M. L. Denton, K. J. Schuster, and B. a. Rockwell. Accurate measure of laser irradiance threshold for near-infrared photo-oxidation with a modified confocal microscope. *J. Microsc.*, 221(Pt 3):164–171, Mar. 2006. ISSN 0022-2720. doi: 10.1111/j.1365-2818.2006.01557.x.
- A. Didierlaurent, J.-C. Sirard, J.-P. Kraehenbuhl, and M. R. Neutra. How the gut senses its content. *Cellular Microbiol.*, 4(2):61–72, 2002.
- A. U. Dignass. Mechanisms and Modulation of Intestinal Epithelial Repair. *Inflammatory Bowel Diseases*, 7(1):68–77, 2001.
- K. W. Dunn, R. M. Sandoval, K. J. Kelly, P. C. Dagher, G. A. Tanner, S. J. Atkinson, R. L. Bacallao, and B. a. Molitoris. Functional studies of the kidney of living animals using multicolor two-photon microscopy. *Am. J. Physiol. - Cell Ph.*, 283(3):C905—C916, Sept. 2002. ISSN 0363-6143.
- N. J. Durr, C. T. Weisspennig, B. A. Holfeld, and A. Ben-Yakar. Maximum imaging depth of two-photon autofluorescence microscopy in epithelial tissues. *J. Biomed. Opt.*, 16(2):26008, Feb. 2011. ISSN 1560-2281.
- E. Essner and A. Novikoff. Human hepatocellular pigments and lysosomes. *J. Ultrastruct. Res.*, 3:374–391, 1960.
- A. Fasano. Zonulin and Its Regulation of Intestinal Barrier Function : The Biological Door to Inflammation , Autoimmunity , and Cancer. *Physiol. Rev.*, 91:151–175, 2011.
- M. P. Fink. Leaky gut hypothesis: a historical perspective. *Critical care medicine*, 18:579–580, 1990.
- A. Gebert. The role of M cells in the protection of mucosal membranes. *Histochem. Cell Biol.*, 108(6):455–470, Dec. 1997. ISSN 0948-6143.
- F. R. Gilmore. The collapse and growth of a spherical bubble in a viscous compressible liquid. *Calif. Inst. Tech. Hydrodynamics Lab. Report*, 26-4, 1952.
- M. Göppert-Mayer. Über Elementarakte mit zwei Quantensprüngen. *Ann. Phys.*, 9(3):273–294, 1931.
- D. Grand, A. Bernas, and E. Amouyal. Photoionization of aqueous indole; conduction band edge and energy gap in liquid water. *Chem. Phys.*, 44:73, 1979.
- J. Grossmann, S. Mohr, E. G. Lapentina, C. Fiocchi, and A. D. Levine. Sequential and rapid activation of select caspases during apoptosis of normal intestinal epithelial cells. *Am. J. Physiol.*, 274(6 Pt 1):G1117–G1124, 1998.
- C. Günther, H. Neumann, M. F. Neurath, and C. Becker. Apoptosis, necrosis and necroptosis: cell death regulation in the intestinal epithelium. *Gut*, n.a.(June), June 2012. ISSN 1468-3288.

## REFERENCES

---

- D. Guy-Grand and P. Vassalli. Gut intraepithelial T lymphocytes. *Curr. Opin. Immunol.*, 5(2):247–252, 1993.
- N. M. Haralampus-Grynaviski, L. E. Lamb, C. M. R. Clancy, C. Skumatz, J. M. Burke, T. Srana, and J. D. Simon. Spectroscopic and morphological studies of human retinal lipofuscin granules. *Proc. Natl. Acad. Sci.*, 100:3179–3184, 2003.
- A. N. Hellman, K. R. Rau, H. H. Yoon, and V. Venugopalan. Biophysical Response to Pulsed Laser Microbeam-Induced Cell Lysis and Molecular Delivery. *J. Biophoton.*, 12(1):1–12, 2007. ISSN 1864-0648.
- F. Helmchen and W. Denk. Deep tissue two-photon microscopy. *Nat. Meth.*, 2(12):932–940, 2005.
- C. Hofmann, F. Obermeier, M. Artinger, M. Hausmann, and W. Falk. Cell-cell contacts prevent anoikis in primary human colonic epithelial cells. *Gastroenterology*, 132:587–600, 2007.
- A. Hopt and E. Neher. Highly nonlinear photodamage in two-photon fluorescence microscopy. *Biophys. J.*, 80(4):2029–2036, Apr. 2001. ISSN 0006-3495.
- V. Hovhannisyan, W. Lo, C. Hu, S.-J. Chen, and C. Y. Dong. Dynamics of femtosecond laser photo-modification of collagen fibers. *Opt. Express*, 16(11):7958–7968, May 2008. ISSN 1094-4087.
- V. Hovhannisyan, A. Ghazaryan, Y.-F. Chen, S.-J. Chen, and C.-Y. Dong. Photophysical mechanisms of collagen modification by 80 MHz femtosecond laser. *Opt. Express*, 18(23):24037–47, Nov. 2010. ISSN 1094-4087.
- S. Huang, A. A. Heikal, and W. W. Webb. Two-Photon Fluorescence Spectroscopy and Microscopy of NAD(P)H and Flavoprotein. *Biophys. J.*, 78(5):2811–2825, May 2002. ISSN 0006-3495.
- D. A. Hume, V. H. Perry, and S. Gordon. The mononuclear phagocyte system of the mouse defined by immunohistochemical localisation of antigen F4/80: macrophages associated with epithelia. *Anat. Rec.*, 210(3):503–512, 1984.
- M. S. Hutson and X. Ma. Plasma and cavitation dynamics during pulsed laser microsurgery in vivo. *Phys. Rev. Lett.*, 99(15):158104, 2007.
- K. Inagaki-Ohara, T. Chinen, G. Matsuzaki, A. Sasaki, Y. Sakamoto, K. Hiromatsu, F. Nakamura-Uchiyama, Y. Nawa, and A. Yoshimura. Mucosal T cells bearing TCR gamma delta play a protective role in intestinal inflammation. *J. Immunol.*, 173:1390–1398, 2004.
- H. Jaeschke. Molecular mechanisms of hepatic ischemia-reperfusion injury and preconditioning. *Am. J. Physiol. Gastrointest. Liver Physiol.*, 284:G15–G26, 2003.

## REFERENCES

---

- S. M. Karam. Lineage commitment and maturation of epithelial cells in the gut. *Front. Biosci.*, 4:D286–98, 1999.
- B. L. Kelsall and W. Strober. Distinct populations of dendritic cells are present in the subepithelial dome and T cell regions of the murine Peyer’s patch. *J. Exp. Med.*, 183(1):237–247, 1996.
- A. Klinger, R. Orzekowsky-Schroeder, D. von Smolinski, M. Blessenohl, A. Schueth, N. Koop, G. Huettmann, and A. Gebert. Complex morphology and functional dynamics of vital murine intestinal mucosa revealed by autofluorescence 2-photon microscopy. *Histochem. Cell Biol.*, 137(3):269–278, Mar. 2012. ISSN 1432-119X.
- H. J. Koester, D. Baur, R. Uhl, and S. W. Hell. Ca<sup>2+</sup> fluorescence imaging with pico- and femtosecond two-photon excitation : Signal and Photodamage. *Biophys. J*, 77(October): 2226–2236, 1999.
- K. König. Clinical multiphoton tomography. *J. Biophot.*, 1(1):13–23, 2008.
- K. König, H. Liang, M. W. Berns, and B. J. Tromberg. Cell damage by near-IR microbeams. *Nature*, 377(6544):20–21, 1995.
- K. König, T. W. Becker, P. Fischer, I. Riemann, and K.-J. K.-J. J. Halbhüser. Pulse-length dependence of cellular response to intense near-infrared laser pulses in multiphoton microscopes. *Opt. Lett.*, 24(2):113–115, Jan. 1999a. ISSN 0146-9592.
- K. König, I. Riemann, P. Fischer, and K. Halbhüser. Intracellular nanosurgery with near infrared femtosecond laser pulses. *Cell. Mol. Biol.*, 45:195–201, 1999b.
- K. König, A. Ehlers, I. Riemann, S. Schenkl, R. Bückle, and M. Kaatz. Clinical Two-Photon Microendoscopy. *Microsc. Res. Techniq.*, 70:398–402, 2007.
- V. Konjufca and M. J. Miller. Two-photon microscopy of host-pathogen interactions: acquiring a dynamic picture of infection in vivo. *Cellular Microbiol.*, 11(4):551–559, 2009.
- H. Kono and K. L. Rock. How dying cells alert the immune system to danger. *Nat. Rev. Immunol.*, 8:279–289, 2008.
- W. Lauterborn. Kavitation durch Laserlicht. *Acustica*, 31(2):52–78, 1974.
- W. Lauterborn and A. Vogel. Shock wave emission by laser generated bubbles. In C. F. Delale, editor, *Bubble Dynamics & Shock Waves, SHOCKWAVES 8*, chapter 3, pages 67–103. Springer, Berlin, 2013.
- V. S. Le Bleu, B. MacDonald, and R. Kalluri. Structure and function of basement membranes. *Exp Biol Med*, 232(9):1121–9, Oct. 2007. ISSN 1535-3702.

## REFERENCES

---

- J. M. Lee, M. C. Grabb, G. J. Zipfel, and D. W. Choi. Brain response to ischemia. *J. Clin. Invest.*, 106:723–731, 2000.
- B. Lemaitre, E. Nicolas, L. Michaut, J. M. Reichhart, and J. A. Hoffmann. The dorsoventral regulatory gene cassette *spätzle/Toll/cactus* controls the potent antifungal response in *Drosophila* adults. *Cell*, 86:973–983, 1996.
- J. E. Lin, A. E. Snook, P. Li, B. A. Stoecker, G. W. Kim, M. S. Magee, A. V. M. Garcia, M. A. Valentino, T. Hyslop, S. Schulz, and S. A. Waldman. GUCY2C opposes systemic genotoxic tumorigenesis by regulating AKT-dependent intestinal barrier integrity. *PLoS one*, 7(2):e31686, Jan. 2012. ISSN 1932-6203.
- N. Linz. *Controlled Nonlinear Energy Deposition in Transparent Dielectrics by Femtosecond and Nanosecond Optical Breakdown*. Phd, University of Luebeck, Luebeck, Germany, 2010.
- N. Linz, S. Freidank, R. Orzekowsky-Schroeder, and A. Vogel. Interferometric single-shot determination of cavitation bubble dynamics in water and transparent biological tissues with nanometer resolution. *in preparation*, 2013.
- M. T. Lotze, H. J. Zeh, A. Rubartelli, L. J. Sparvero, and A. A. Amoscato. The grateful dead: damage-associated molecular pattern molecules and reduction/oxidation regulate immunity. *Immunol. Rev.*, 220:60–81, 2007.
- R. Lüllmann-Rauch. *Histologie*. Thieme, Stuttgart, 2 edition, 2006. ISBN 3-13-129242-3.
- J. L. Madara. Maintenance of the macromolecular barrier at cell extrusion sites in intestinal epithelium: physiological rearrangement of tight junctions. *J Membr. Biol.*, 116(2):177–184, 1990.
- A. M. Marchiando, W. V. Graham, and J. R. Turner. Epithelial barriers in homeostasis and disease. *Annu. Rev. Pathol.*, 5:119–144, 2010.
- N. Mata, J. Wen, and G. H. Travis. Biosynthesis of a major lipofuscin fluorophore in mice and humans with ABCR-mediated retinal and macular degeneration. *Proc. Natl. Acad. Sci.*, 97:71547159, 2000.
- L. Mayer, A. Panja, Y. Li, E. Siden, A. Pizzimenti, F. Gerardi, and N. Chandswang. Unique features of antigen presentation in the intestine. *Ann. NY Acad. Sci.*, 664:39–46, Jan. 1992. ISSN 0077-8923.
- S. A. McCormack, M. J. Viar, and L. R. Johnson. Migration of IEC-6 cells: a model for mucosal healing. *Am. J. Physiol.*, 263G:426–435, 1992.
- B. McDonald, K. Pittman, G. B. Menezes, S. a. Hiroto, I. Slaba, C. C. M. Waterhouse, P. L. Beck, D. A. Muruve, and P. Kubes. Intravascular danger signals guide neutrophils to sites of sterile inflammation. *Science*, 330:362–366, 2010.

## REFERENCES

---

- T. R. Mempel, S. E. Henrickson, and U. H. Von Andrian. T-cell priming by dendritic cells in lymph nodes occurs in three distinct phases. *Nature*, 427(6970):154–159, Jan. 2004. ISSN 1476-4687.
- Y. Mochizuki, M. K. Park, T. Mori, and S. Kawashima. The difference in autofluorescence features of lipofuscin between brain and adrenal. *Zool. Science*, 12(3):283–288, 1995. ISSN 0289-0003.
- R. Moore, S. Carlson, and J. L. Madara. Villus contraction aids repair of intestinal epithelium after injury. *Am. J. Physiol. Gastrointest. Liver Physiol.*, 257:274–283, 1989a.
- R. Moore, S. Carlson, and J. L. Madara. Rapid barrier restitution in an in vitro model of intestinal epithelial injury. *Lab. Invest.*, 60:237–244, 1989b.
- A. M. Mowat and J. L. Viney. The anatomical basis of intestinal immunity. *Immunol. Rev.*, 156(Apr.):145–166, 1997.
- M. R. Neutra and M. P. Murtaugh. Current Concepts in Mucosal Immunity. *Am J Physiol Gastrointest Liver Physiol*, 274:785–791, 1998.
- D. N. Nikogosyan. Two-quantum UV photochemistry of nucleic acids: comparison with conventional low-intensity UV photochemistry and radiation chemistry. *Int. J. Radiat. Biol.*, 57(2):233–299, Feb. 1990. ISSN 0955-3002.
- D. N. Nikogosyan, A. A. Oraevsky, and V. Rupasov. Two-photon ionization and dissociation of liquid water by powerful laser UV irradiation. *Chem. Phys.*, 77:131–143, 1983.
- N. Nishimura, C. H. B. Schaffer, B. Friedman, P. S. Tsai, P. D. Lyden, and D. Kleinfeld. Targeted insult to subsurface cortical blood vessels using ultrashort laser pulses : three models of stroke. *Nature Methods*, 3(2):5–7, 2006.
- A. Nusrat, C. Delp, and J. L. Madara. Intestinal epithelial restitution. *J. Clin. Invest.*, 89:1501–1511, 1992.
- R. Orzekowsky-Schroeder, A. Klinger, B. Martensen, M. Blessenohl, A. Gebert, A. Vogel, and G. Hüttmann. In vivo spectral imaging of different cell types in the small intestine by two-photon excited autofluorescence. *J. Biomed. Opt.*, 16(11):116025, 2011.
- J. A. Palero. *Nonlinear Spectral Imaging of Biological Tissues*. Phd, Utrecht, 2007.
- J. A. Palero, H. S. de Bruijn, A. van der Ploeg van den Heuvel, H. J. C. M. Sterenberg, and H. C. Gerritsen. Spectrally Resolved Multiphoton Imaging of In Vivo and Excised Mouse Skin Tissues. *Biophys. J.*, 93(August):992–1007, 2007.
- G. Paltauf and H. Schmidt-Kloiber. Microcavity dynamics during laser-induced spallation of liquids and gels. *Appl. Phys. A - Mater.*, 62(4):303–311, Mar. 1996. ISSN 0947-8396.

## REFERENCES

---

- M. Pentecost, J. Kumaran, P. Ghosh, and M. R. Amieva. *Listeria monocytogenes* internalin B activates junctional endocytosis to accelerate intestinal invasion. *PLoS Pathogens*, 6(5): e1000900, 2010.
- D.-W. Piston and S. M. Knobel. Quantitative imaging of metabolism by two-photon excitation microscopy. *Methods Enzymol.*, 307:351–368, 1999.
- D. K. Podolsky. Healing the epithelium: solving the problem from two sides. *J. Gastroenterol.*, 32:122–126, 1997.
- A. Poltorak, X. He, I. Smirnova, M. Y. Liu, C. van Huffel, X. Du, D. Birdwell, E. Alejos, M. Silva, C. Galanos, M. Freudenberg, P. Riccardi-Castagnoli, B. Layton, and B. Beutler. Defective LPS signaling in C3H/HeJ and C57BL/10ScCr mice: Mutations in the Tlr4 gene. *Science*, 208:2085–2088, 1998.
- C. S. Potten and M. Loeffler. Stem cells: attributes, cycles, spirals, pitfalls and uncertainties. Lessons for and from the crypt. *Development*, 110(4):1001–1020, Dec. 1990. ISSN 0950-1991.
- A. J. Radosevich, M. B. Bouchard, S. A. Burgess, B. R. Chen, and E. M. C. Hillman. Hyper-spectral in vivo two-photon microscopy of intrinsic contrast. *Opt. Lett.*, 33(18):2164–2166, Sept. 2008. ISSN 0146-9592.
- L. O. M. Rayleigh. On the pressure developed in a liquid during the collapse of a spherical cavity. *Phil. Mag*, 34(200):94–98, 1917.
- A. A. Resendiz-Albor, R. Esquivel, R. Lopez-Revilla, L. Verdin, and L. Moreno-Fierros. Striking phenotypic and functional differences in lamina propria lymphocytes from the large and small intestine of mice. *Life Sci.*, 76:2783–2803, 2004.
- R. Richards-Kortum and E. Sevick-Muraca. Quantitative optical spectroscopy for tissue diagnosis. *Annu. Rev. Phys. Chem.*, 47:555–606, Jan. 1996. ISSN 0066-426X.
- J. V. Rocheleau, W. S. Head, and D. W. Piston. Quantitative NAD(P)H/fluoroprotein autofluorescence imaging reveals metabolic mechanisms of pancreatic islet pyruvate response. *J. Biol. Chem.*, 279(30):31780–31787, 2004. ISSN 0021-9258.
- J. Rosenblatt, M. C. Raff, and L. P. Cramer. An epithelial cell destined for apoptosis signals its neighbors to extrude it by an actin- and myosin-dependent mechanism. *Curr. Biol.*, 11(23):1847–1857, 2001.
- C. A. Sacchi. Laser-induced electric breakdown in water. *J. Opt. Soc. Am. B*, 8:337, 1991.
- L. Sacconi, R. P. O. Connor, A. Jasaitis, A. Masi, M. Buffelli, R. P. O’Connor, and F. S. Pavone. In vivo multiphoton nanosurgery on cortical neurons. *J. Biomed. Opt.*, 12(October):050502, 2007.

## REFERENCES

---

- J. Savill. Apoptosis in post-streptococcal glomerulonephritis. *Kidney Int.*, 60:1203–1214, 2001.
- G. Schuler and R. M. Steinman. Murine epidermal Langerhans cells mature into potent immunostimulatory dendritic cells in vitro. *J. Exp. Med.*, 161(526):546, 1985.
- C. N. Serhan and J. Savill. Resolution of inflammation: the beginning programs the end. *Nat. Immunol.*, 6:1191–1197, 2005.
- H.-J. Shin and J.-L. Mego. A rat liver lysosomal membrane flavin-adenine dinucleotide phosphohydrolase: purification and characterization. *Arch. Biochem. Biophys.*, 267:95–103, 1988.
- L. E. Smythies, M. Sellers, R. H. Clements, M. Mosteller-barnum, G. Meng, W. H. Benjamin, J. M. Orenstein, and P. D. Smith. Human intestinal macrophages display profound inflammatory anergy despite avid phagocytic and bacteriocidal activity. *J. Clin. Invest.*, 115(1):66–75, 2005.
- R. M. Steinman and Z. A. Cohn. Identification of a novel cell type in the peripheral lymphoid organs of mice. I. Morphology, quantitation, tissue distribution. *J. Exp. Med.*, 137:1142–1162, 1973.
- R. M. Steinman and M. D. Witmer. Lymphoid dendritic cells are potent simulators of the primary mixed leukocyte reaction in mice. *Proc. Natl. Acad. Sci. USA*, 5132-5136, 1978.
- P. Steven and A. Gebert. Conjunctiva-associated lymphoid tissue - current knowledge, animal models and experimental prospects. *Opht. Res.*, 42(1):2–8, 2009. ISSN 1423-0259.
- P. Steven, J. Rupp, G. Hüttmann, N. Koop, C. Lensing, H. Laqua, and A. Gebert. Experimental induction and three-dimensional two-photon imaging of conjunctiva-associated lymphoid tissue. *Invest. Ophthalmol. Vis. Sci.*, 49:1512–1517, 2008.
- M. Strupler, A.-M. Pena, M. Hernest, P.-L. Tharaux, J.-L. Martin, E. Beaurepaire, and M.-C. Schanne-Klein. Second harmonic imaging and scoring of collagen in fibrotic tissues. *Opt. Express*, 15(7):4054–65, Apr. 2007. ISSN 1094-4087.
- W. Supatto, D. Débarre, B. Moulia, E. Brouzés, J.-L. Martin, E. Farge, and E. Beaurepaire. In vivo modulation of morphogenetic movements in *Drosophila* embryos with femtosecond laser pulses. *Proc. Natl. Acad. Sci.*, 102(4):1047–52, Jan. 2005. ISSN 0027-8424.
- L. M. Tiede and M. G. Nichols. Photobleaching of reduced nicotinamide adenine dinucleotide and the development of highly fluorescent lesions in rat basophilic leukemia cells during multiphoton microscopy. *Photochem. Photobiol.*, 82:656–664, 2006.
- U. K. Tirlapur, K. König, C. Peuckert, R. Krieg, K.-j. K.-J. Halbhuber, and K. Ko. Femtosecond Near-Infrared Laser Pulses Elicit Generation of Reactive Oxygen Species in Mammalian Cells Leading to Apoptosis-like Death. *Exp. Cell Res.*, 263:88–97, 2001.

## REFERENCES

---

- T. Tsuchiya, S. Fukuda, H. Hamada, A. Nakamura, Y. Kohama, H. Isikawa, K. Tsujikawa, and H. Yamamoto. Role of gamma delta T cells in the inflammatory response of experimental colitis in mice. *J. Immunol.*, 171:5507–5513, 2003.
- J. R. Turner. Intestinal mucosal barrier function in health and disease. *Nature Reviews Immunology*, 9:799–809, 2009.
- S. Uematsu, K. Fujimoto, M. H. Jang, B. G. Yang, Y. J. Jung, M. Nishiyama, S. Sato, T. Tsujimura, M. Yamamoto, Y. Yokota, M. Kiyona H, Miyasaka, K. J. Ishii, and S. Akira. Regulation of humoral and cellular gut immunity by lamina propria dendritic cells expressing Toll-like receptor 5. *Nat. Immunol.*, 9:769–776, 2008.
- C. Varol, A. Vallon-Eberhard, E. Elinav, T. Aychek, Y. Shapira, H. Luche, H. J. Fehling, W. Hardt, G. Shakar, and S. Jung. Intestinal lamina propria dendritic cell: subsets having different origin and functions. *Immunity*, 31:502–512, 2009.
- V. Venugopalan, A. G. Iii, K. Nahen, A. Vogel, A. Guerra III, and A. Guerra. Role of Laser-Induced Plasma Formation in Pulsed Cellular Microsurgery and Micromanipulation. *Phys. Rev. Lett.*, 88:78103, 2002.
- A. Vogel and V. Venugopalan. Mechanisms of Pulsed Laser Ablation of Biological Tissues. *Chem. Rev.*, 103(2):577–644, Feb. 2003. ISSN 0009-2665.
- A. Vogel, S. Busch, and U. Parlitz. Shock wave emission and cavitation bubble generation by picosecond and nanosecond optical breakdown in water. *J. Acoust. Soc. Am.*, 100(1):148–165, 1996.
- A. Vogel, J. Noack, G. Huttman, G. Paltauf, and G. Hüttman. Mechanisms of femtosecond laser nanosurgery of cells and tissues. *Appl. Phys. B - Lasers O.*, 81(8):1015–1047, 2005.
- A. Vogel, N. Linz, S. Freidank, and G. Paltauf. Femtosecond-Laser-Induced Nanocavitation in Water: Implications for Optical Breakdown Threshold and Cell Surgery. *Phys. Rev. Lett.*, 100(3):1–4, 2008. ISSN 0031-9007.
- A. Vogel, N. Linz, and S. Freidank. Method for laser machining transparent materials, 2010.
- H.-J. von Brandis and W. Schönberger. *Anatomie und Physiologie für Krankenpflegeberufe sowie andere medizinische und pharmazeutische Fachberufe*. Gustav Fischer Verlag, Stuttgart, 9. auflage edition, 1995. ISBN 3-437-00653-3.
- G. A. Wagnières, W. M. Star, B. C. Wilson, and G. A. Wagnieres. In Vivo Fluorescence Spectroscopy and Imaging for Oncological Applications. *Photochem. Photobiol.*, 88(5):603–632, 1998.
- A. J. M. Watson, S. Chu, L. Sieck, O. Gerasimenko, T. Bullen, F. Campbell, M. McKenna, T. Rose, and M. H. Montrose. Epithelial barrier function in vivo is sustained despite gaps in epithelial layers. *Gastroenterology*, 129(3):902–912, Sept. 2005. ISSN 0016-5085.

## REFERENCES

---

- F. Williams, S. P. Varama, and S. Hillenius. Liquid water as a lone-pair amorphous semiconductor. *J. Chem. Phys.*, 64:1549–1554, 1976.
- A. J. Wilson and P. R. Gibson. Epithelial migration in the colon: filling the gaps. *Clin. Sci.*, 93:97–108, 1997.
- M. Wisniewski, A. Sionkowska, H. Kaczmarek, S. Lazare, V. Tokarev, and C. Belin. Spectroscopic study of a KrF excimer laser treated surface of thin collagen films. *J. Photochem. Photobiol. A: Chemistry*, 188(2-3):192–199, 2007.
- J. L. Wolf and W. A. Bye. The membranous epithelial (M) cell and the mucosal immune system. *Ann. Rev. Med.*, 35(1):95–112, 1984.
- C. Xu and W. W. Webb. Measurement of two-photon excitation cross sections of molecular fluorophores with data from 690 to 1050 nm. *J. Opt. Soc. Am. B*, 13(3):481–491, Mar. 1996. ISSN 0740-3224.
- M. F. Yanik, H. H. N. Cinar, A. D. Chisholm, Y. Jin, and A. Ben-Yakar. Functional regeneration after laser axotomy. *Nature*, 432(December):822, 2004.
- J. Yuan and G. Kroemer. Alternative cell death mechanisms in development and beyond. *Genes Dev.*, 24(23):2592–2602, 2010.
- Q. Q. Zhang, D. W. Piston, and R. H. Goodman. Regulation of corepressor function by nuclear NADH. *Science*, 295(2002):1895–1897, 2002.
- B. H. Zinselmeyer, J. N. Lynch, X. Zhang, T. Aoshi, and M. J. Miller. Video-rate two-photon imaging of mouse footpad - a promising model for studying leukocyte recruitment dynamics during inflammation. *Inflamm. Res.*, 57(3):93–96, 2008. ISSN 1023-3830.
- W. R. Zipfel, R. M. Williams, R. Christie, A. Y. Nikitin, B. T. Hyman, and W. W. Webb. Live tissue intrinsic emission microscopy using multiphoton-excited native fluorescence and second harmonic generation. *Proc. Natl. Acad. Sci. USA*, 100(12):7075–7080, June 2003. ISSN 0027-8424.
- A. Zoumi, A. Yeh, and B. J. Tromberg. Imaging cells and extracellular matrix in vivo by using second-harmonic generation and two-photon excited fluorescence. *Proc. Natl. Acad. Sci. USA*, 99(17):11014–11019, Aug. 2002. ISSN 0027-8424.

## REFERENCES

---

# Publications

## Publications related to the work described in this thesis

1. **R. Orzekowsky-Schroeder**, A. Klinger, A. Schueth, S. Eckert, S. Freidank, G. Hüttmann, A. Gebert, and A. Vogel, *Intravital laser nanosurgery of murine gut mucosa with online monitoring of cavitation bubble dynamics and two-photon microscopy of healing response*. To be submitted to Biomed. Opt. Expr. (2013)
2. Y. Miura, G. Hüttmann, **R. Orzekowsky-Schroeder**, P. Steven, M. Szaszák, N. Koop, and R. Brinkmann, *Two-Photon Microscopy and Fluorescence Lifetime Imaging of Retinal Pigment Epithelial Cells under Oxidative Stress*. Accepted for publication in Invest. Opth. Vis. Sci. (2013)
3. A. Klinger, **R. Orzekowsky-Schroeder**, D. von Smolinski, M. Blessenohl, A. Schueth, N. Koop, G. Huettmann, and A. Gebert. *Complex morphology and functional dynamics of vital murine intestinal mucosa revealed by autofluorescence 2-photon microscopy*. Histochem. Cell Biol. (2011) DOI 10.1007/s00418-011-0905-0
4. **R. Orzekowsky-Schroeder**, A. Klinger, B. Martensen, M. Blessenohl, A. Gebert, A. Vogel, and G. Huttmann, *In vivo spectral imaging of different cell types in the small intestine by two-photon excited autofluorescence*. J. Biomed. Opt. **16**, 116025 (2011)
5. M. Szaszák, P. Steven, K. Shima, **R. Orzekowsky-Schröder**, G. Hüttmann, I. König, W. Solbach, and J. Rupp, *Fluorescence lifetime imaging unravels c. trachomatis metabolism and its crosstalk with the host cell*. PLoS Pathogens. **7**(7), e1002108 (2011)
6. **R. Orzekowsky-Schroeder**, A. Klinger, A. Schüth, S. Freidank, G. Hüttmann, A. Gebert, and A. Vogel. *Intravital real-time study of tissue response to controlled laser-induced cavitation using 500-ps UV laser pulses focused in murine gut mucosa under online dosimetry and spectrally resolved 2-photon microscopy*. Proc. SPIE **7568**, 756815 (2010)
7. S. Kretschmer, **R. Orzekowsky-Schroeder**, G. Hüttman, and P. König. *Bildgebung zellulärer Dynamik in den Atemwegen mittels der 2-Photonen Laserscanning Mikroskopie mit endogenen und exogenen Fluoreszenzfarbstoffen*. Pneumologie **64**, A33 (2010)

## REFERENCES

---

### Conference contributions related to the work described in this thesis

#### Oral presentations

1. G. Hüttmann, **R. Orzekowsky-Schroeder**, A. Vogel, A. Klinger, A. Gebert, U. Gehlsen, F. Bock, and P. Steven. *Imaging of immune cell dynamics in small intestine and teh eye by 2-photon microscopy*.  
7th Workshop on Advanced Multiphoton and Fluorescence Lifetime Imaging Techniques (FLIM 2012), Saarbrücken, Germany, 2012
2. A. Gebert, D. von Smolinski, **R. Orzekowsky-Schroeder**, G. Hüttmann, and A. Klinger. *Dynamik intraepithelialer Lymphozyten in der Darmschleimhaut: Ergebnisse der Autofluoreszenz-2-Photonenmikroskopie in der lebenden Maus*.  
3. Symposium Zentrum für Medizinische Optik und Photonik (ZeMOP) Jena, Deutschland, 2012
3. **R. Orzekowsky-Schroeder**, A. Klinger, A. Schüth, S. Freidank, G. Hüttmann, A. Gebert, and A. Vogel. *Intravital real-time study of tissue response to controlled laser-induced cavitation using 500-ps UV laser pulses focused in murine gut mucosa under online dosimetry and spectrally resolved 2-photon microscopy*.  
SPIE BiOS, San Francisco, USA, 2011
4. L. Krapf, **R. Orzekowsky-Schroeder**, N. Koop, A. Rodewald, H. Diddens-Tschoeke, and G. Hüttmann, *Multiphoton imaging with 10 fs pulses*  
FLIM Workshop, Saarbrücken, Germany, 2011
5. **R. Orzekowsky-Schroeder**, G. Hüttmann, N. Koop, A. Vogel, A. Klinger, M. Bleszenohl, and A. Gebert. *In vivo spectral imaging of different cell types by two-photon excited autofluorescence in the small intestine*  
European Conference on Biomedical Optics (ECBO) 2009, Munich, Germany
6. **R. Orzekowsky-Schroeder**, G. Hüttmann, N. Koop, A. Vogel, A. Klinger, M. Bleszenohl, and A. Gebert. *Multi-spectral imaging of tissue autofluorescence: discriminating cell types during dynamic processes in the intestine*  
4th Workshop on Advanced Multiphoton and Fluorescence Lifetime Imaging Techniques (FLIM 2009) Workshop, Saarbrücken, Germany, 2009

#### Poster presentations

1. Y. Miura, G. Hüttmann, M. Szaszák, **R. Orzekowsky-Schroeder**, N. Koop, P. Steven, and R. Brinkmann. *Two-photon microscopy and fluorescence lifetime analysis of lipid peroxidation product in photoreceptor outer segment and in retinal pigment epithelial cell*.  
ARVO, Fort Lauderdale, USA, 2012

2. U. Gehlsen, R. Orzekowsky-Schroeder, M. Szaszák, N. Koop, S.E. Siebelmann, G. Hüttmann, and P. Steven. *Non-invasive multi-dimensional two-photon microscopy distinguishes activation states of antigen presenting cells.*  
ARVO, Fort Lauderdale, USA, 2011
3. Y. Miura, G. Hüttmann, **R. Orzekowsky-Schroeder**, P. Steven, M. Szaszák, N. Koop, R. Birngruber, and R. Brinkmann. *Investigations of two-photon excited bright autofluorescent granules in the RPE cells around photocoagulation spots.*  
ARVO, Fort Lauderdale, USA, 2011
4. U. Gehlsen, G. Hüttmann, **R. Orzekowsky-Schroeder**, N. Koop, S. Siebelmann, P. Steven. *Optical fingerprinting of key players in ocular surface inflammation by non-invasive multi-dimensional two-photon-microscopy.*  
ARVO, Fort Lauderdale, USA, 2010
5. A. Schüth, L. Krapf, J. Dimitrijevic, A. Klinger, **R. Orzekowsky-Schroeder**, T. Vossmeier, G. Hüttmann, H. Weller, and A. Gebert. *Uptake of 200 nm latex particles and 20 nm quantum dots by the small intestinal mucosa - an intravital two-photon microscopy study in mice.*  
European Cells and Materials, 3rd International NanoBio Conference, Zurich, Switzerland, 2010
6. A. Gebert, D. von Smolinski, M. Blessenohl, A. Schüth, **R. Orzekowsky-Schroeder**, J. Textor, A. Klinger, and G. Hüttmann. *Intravital lymphocyte trafficking in the intestinal epithelium: a novel experimental model based on high-resolution autofluorescence 2-photon microscopy.*  
2nd European Congress of Immunology, Berlin, Germany, 2009.
7. A. Gebert, M. Blessenohl, D. von Smolinski, A. Schüth, **R. Orzekowsky-Schroeder**, J. Textor, G. Hüttmann, and A. Klinger. *In vivo dynamics of intraepithelial lymphocytes in the gut: a novel experimental approach based on high-resolution autofluorescence 2-photon microscopy.*  
16th Germinal Center Conference, Frankfurt, Germany, 2009.
8. S. Kretschmer, A. Gebert, **R. Orzekowsky-Schroeder**, G. Hüttmann, and P. König. *An airway ex-vivo model to study tissue structures and cellular dynamics using two-photon microscopy.* Joint meeting Anatomische Gesellschaft - Nederlandse Anatomen Vereniging, Antwerpen, Netherlands, 2009
9. **R. Orzekowsky**, G. Hüttmann, N. Koop, A. Vogel, A. Klinger, M. Blessenohl, and A. Gebert. *In vivo spectral fingerprinting of different cell types in murine intestinal tissue by multiphoton excited autofluorescence*  
Gordon Research Conference for Lasers in Medicine and Biology, Holderness, USA, 2008
10. P. Steven, J. Rupp, G. Hüttmann, **R. Orzekowsky**, N. Koop, and A. Gebert. *Intravitreal two-photon-imaging of conjunctiva-associated lymphoid tissue - A new window to visualize*

## REFERENCES

---

*immune mechanisms of the ocular surface.*

ARVO 2008, Fort Lauderdale, USA

## Other publications

1. D. Nau, A. Seidel, **R. Orzekowsky**, S.-H. Lee, S. Deb, and H. Giessen. *Hydrogen sensor based on metallic photonic crystal slabs*. Opt. Lett. **35**(18), 3150-2 (2010)
2. D. Nau, **R. Orzekowsky**, A. Seidel, T. Meyrath, H. Giessen; *A Hydrogen Sensor Based on Metallic Photonic Crystal Slabs*. CLEO/QELS 2008, San Jose, USA (talk)
3. **R. Orzekowsky**, A. Seidel, and H. Giessen. *Wasserstoffsensoren auf Basis metallischer photonischer Kristalle*. DPG spring meeting 2007, Regensburg, Germany (talk)

# Acknowledgements

*per aspera ad astra*

There are a number of persons without whose support this thesis would never have been completed.

It is my pleasure to thank my supervisor and promotor Alfred Vogel, who helped me throughout my time as a PhD student in his group. Thank you for pushing me to my limits with challenging tasks, and for your confidence in my success. Your thoughtful comments and discussions and your eye for the overall picture always helped me not to lose the red thread while struggling with details of my work. I want to especially thank you for giving me the opportunity for scientific exchange on international conferences. These experiences surely were some of the highlights during my years of research.

My special gratitude goes also to my second supervisor, Gereon Hüttmann. Your broad knowledge in the field of biomedical optics and your infectious enthusiasm for research in general were an inexhaustible source of inspiration and encouragement.

The work described in this thesis would not have been possible without the close collaboration with Antje Klinger. Thank you Antje, for providing your medical and anatomical expertise without that none of the mouse experiments would have been possible. I very much enjoyed our long-time lab-sessions and thank you also for many fruitful discussions regarding the biologic significance of our results, or for translating complex biological and immunological concepts into a language that is understood by a physicist.

I also want to thank Andreas Gebert whose interest in intestinal mucosa was a key factor for the initiation of this whole research project, and who initially revealed to me the beauty of moving cells.

I especially thank my colleagues Norbert Linz and Sebastian Freidank for contributing to my experiments their invaluable experience with setups for cavitation bubble generation and detection and for countless funny hours in the lab and elsewhere. I also thank my colleagues and office mates Sebastian Eckert, Tobias Jachowski and Xiaoxuan Liang for most interesting discussions on science and beyond and for their support in many aspects.

## REFERENCES

---

I gratefully acknowledge the support of Norbert Koop and Reinhard Schulz, who always helped in finding timely and custom-made solutions to problems related with mechanical hardware or lab infrastructure, be it on a large scale such as for optical tables or on a tiny scale such as for the mouse holder.

I thank Barbara Flucke, Astrid Rodewald and Christiane Heise, who not only supported me in several work-related issues but also particularly made me feel at home in the institute.

I thank the ‘Two-Photon Girls Task Force’, Lisa Krapf, Sarah Kretschmer, Anna Schüth, Márta Szaszák, Uta Gehlsen, and Yoko Miura, for valuable interdisciplinary exchange of support and knowledge.

Finally I would like to thank my family and friends for their support throughout my way. It is without saying that you deserve more than a simple ‘Thank You’. Your love, support and encouragement kept me going.

And most importantly, thank you Martin for being there for me.